Commissie Opberging
Radioactief Afval (CORA)

Cora 12

RuG

Radiation Damage in NaCl
Retrievability
Smart Backfill Materials
Monitoring

Final Report
CORA research project
December 1999

State University of Groningen
4 Nijenborgh
9747 AG Groningen
the Netherlands

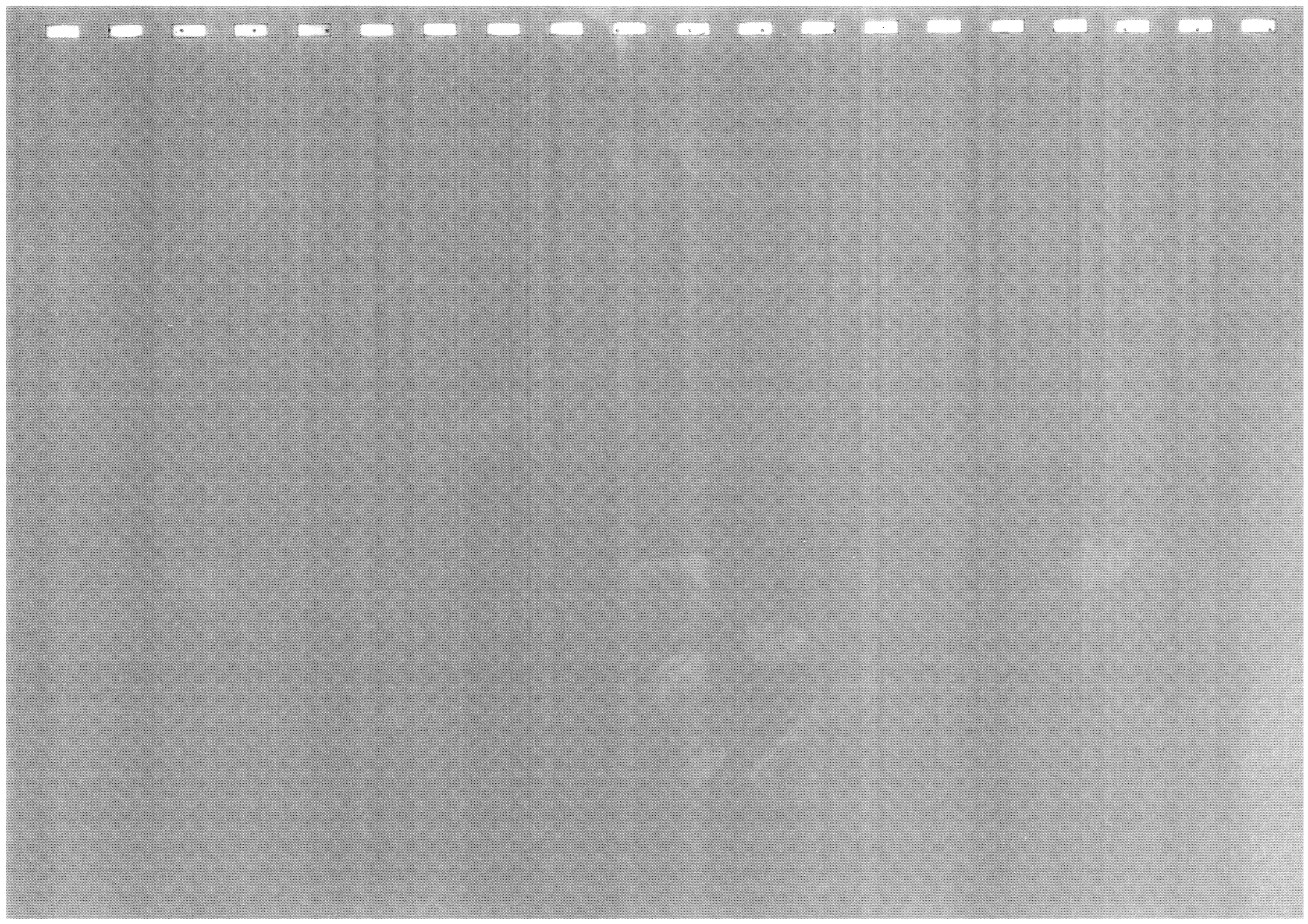

State University of Groningen
Solid State Physics Laboratory

Radiation Damage in NaCl

Retrievability
Smart Backfill Materials
Monitoring

Final Report
CORA research project

Henry W. den Hartog
David Vainshtein
Vladimir Dubinko
Anatole Turkin
Vladimir Gann
Jan Jacobs

Contents

1 INTRODUCTION

In this report we describe the achievements and results obtained from our research project entitled "Radiation Damage in NaCl". As planned in the proposal, a lot of the work was done on the preparation/modification of the irradiation facility, which has been used during this project (i.e. from Jan. 1st 1998 until the end, which was scheduled at Dec. 1st of 1999).

After the formal procedures were finalized by the letter from the Ministry of Economic Affairs E/EE/KK/97063517, which was received by us in the beginning of December 1997, "Het College van Bestuur van de Rijksuniversiteit Groningen" gave us the permission to carry out this project mid December 1997. The official letter FED 98/00431 was dated 15 Jan. 1998. Fortunately, we could hire the necessary personnel and start our work by Jan 1st of 1998.

1.1 General

In this research project, the contribution to the development of a dependable and, above all retrievable, method to store high level waste (HLW) of nuclear power plants is the central issue. At the end of the OPLA research program it has been concluded that the phenomena associated with radiation damage, generated in artificial and natural NaCl samples, is one of the unsolved problems of storage of nuclear waste in natural rock salt formations. This problem still exists, because it is impossible to simulate storage conditions directly with laboratory or in-situ experiments. Irradiation times of several hundred years would be required. In addition, rock salt in a storage site varies in composition, which gives rise to differences in the efficiency of the damage formation processes. In-situ experiments have been carried out in a limited range of doses and at high dose rates. Laboratory experiments have been performed in a wide range of doses (up to 300 Grad[1]), but the dose rates were extremely high (between 8 and 500 Mrad/hr).

The gap between laboratory situations or in-situ conditions on the one hand and storage conditions on the other hand can be closed by applying suitable theoretical models describing the radiolysis processes. In order to achieve this, we need improved theoretical models, because we have found during earlier investigations that we are not able to explain several important features of damage formation in NaCl with the existing models [1- 5]. The improvements require significant additional research efforts. It is worthwhile to make these efforts, because together with systematic experiments, theoretical models play a decisive role in the safety assessment of the radiation effects in NaCl. The above mentioned improvements should also provide us with an adequate description of void formation as will become clear from the information presented below.

We have observed experimentally [6-8], that heavily irradiated NaCl may explode during or after irradiation. In addition, we have concluded that it cannot be excluded that these explosions take place during storage in a rock salt formation in the vicinity of a canister with HLW. Explosions, especially those in the vicinity of the HLW, are highly undesirable, because they endanger the retrievability of the stored high level waste and therefore the

[1] In this report we give the dose in units Mrad or Grad instead of the SI units MGy or GGy. In order to obtain the SI based values the numbers mentioned in this report should be divided by a factor of 100, i.e. 150 Grad is equivalent to 1.5 GGy, or 1500 MGy.

investigation of radiolytic effects, as carried out in this project, is closely connected with the condition of retrievable storage.

In the above-mentioned explosions the radiolytic sodium and chlorine precipitates and voids play an essential role. Prior to the start of this project only little information about voids in irradiated NaCl was available, and we have attempted to investigate as many heavily irradiated samples as possible in order to obtain information about the production of voids. In addition, the annealing behavior of these unstable systems, and the mechanism of the collapse of voids have been investigated, because these phenomena are closely related with explosive decomposition.

From earlier investigations we have obtained evidence that the collapse of unstable voids initiates the explosion of irradiated NaCl. We have also found that the size of the voids depends upon the presence of impurities; in several doped samples large voids are produced, indicating that it is necessary to investigate the effects of doping. Natural rock salt from the Netherlands and Germany (Asse) does not behave as pure NaCl. In these materials large and unstable voids are produced at relatively low doses, and in accordance with this observation relatively powerful explosions have been observed in many irradiated natural rock salt samples, which supported the idea that voids are essential ingredients in the explosive processes.

In this project we have investigated the properties of radiation-induced voids as a function of the impurity content, the dose and the irradiation temperature. These investigations have been carried out mainly with SEM, in most cases combined with DSC and annealing experiments. These results provide us with information about the stability of irradiated samples depending upon the numbers, size and shape of the voids. We note that as compared to the research of the radiolytic products Na and Cl_2 we have to improve the information for voids. At this point we emphasize again that the investigation of radiation-induced voids is highly necessary in order to ensure retrievability of the storage of HLW. We note that until the start of this research project there was little or no information about the void production as a function of the dose rate, the irradiation temperature and the impurity content.

1.2 Goals of the project

The work in this research project was focused at several goals, which are connected with the central issues of the CORA research program and several unsolved problems of the OPLA research program. These goals will be sketched briefly in the next few sub-sections.

1.2.1 Goal 0: Preparation of the irradiation facility

In order to carry out the investigations, outlined below, it was necessary to prepare/modify our irradiation facility for long-term and high dose rate operation. According to the time schedule in our proposal the major part of this work has been carried out during the first stage of this research project. The time needed to complete this job was estimated to be about 9 months. As expected, the first part of the project has been used almost completely in order to reach this goal.

1.2.2 Goal 1: Investigation of voids

In the explosive processes, which have been observed for heavily irradiated NaCl, radiolytic precipitates of sodium and chlorine and voids play an essential role. The information, deduced from earlier experiments, leads us to the assumption that the voids are important players in the initiation of explosive processes, and they need further investigations. In order to achieve this goal, we have investigated systematically many irradiated samples. We have obtained new and highly relevant information about the size, shape, and concentration of voids. We have investigated several samples from previous irradiation runs and new irradiation experiments by means of DSC, ESR and SEM. The SEM experiments yield important details about the formation of voids. The ESR results provide us with information about the Na colloids. DSC experiments have been carried out between –140 and 250 °C, which implies that in many cases we have obtained information about the presence of Na, chlorine and voids.

In particular, we planned to increase our knowledge of voids, because radiation induced voids may affect the retrievability. At the start of this project little information was available about the void production as a function of the dose, the dose rate, the irradiation temperature and the impurity content.

1.2.3 Goal 2:"Smart" backfill materials

An important aim of this project is to contribute to the development of smart backfill materials by finding doped NaCl samples with reduced formation of voids. Samples with small numbers of (small) voids are expected to be relatively stable and we expect that these materials will not explode even after heavy irradiation.

From the point of view of mechanical and chemical stability doped NaCl could be used as a backfill material, because the density of doped NaCl is approximately the same as the host rock. There are candidate materials, but there is insufficient information about the formation of radiation induced voids. In this project we have collected significantly more information about the production of voids as a function of the impurity content, which allows us to give recommendations for further investigations of particular doped NaCl backfill materials. This type of research will also help us to define strategies to be used in future storage sites and it will eventually help us to find details such as the thickness and composition of the backfill layer.

1.2.4 Goal 3: Relation with future monitoring of storage sites

An important aim of this project is to find out which radiation damage parameters should be monitored and, if possible, to estimate what the critical values of these parameters are. At this moment we can say that it is crucial to monitor the percentages of radiolytic sodium and chlorine, because samples with large amounts of Na and Cl_2 often showed explosive effects. At the same time we conclude that monitoring the numbers, sizes and shapes of the radiation-induced voids is also necessary, because voids may initiate the explosions. We have carried out some systematic experiments, in which the samples were heated to initiate explosive decomposition. These experiments will help us to recognize dangerous conditions during irradiation in a storage site with HLW. Our experimental results have revealed that with increasing temperature the stability of the radiation-induced voids is reduced, i.e. at higher temperatures the probability for explosive decomposition increases.

The first measures to avoid dangerous conditions are (as mentioned above) the application of smart backfill layers, but also an active approach may be possible. With *local* heaters close to the HLW one can probably anneal the radiation damage in a small region of the salt to some extent (we hope that this applies to both colloids and voids). If these local heating actions are carried out in a suitable way, it probably contributes only slightly to the overall temperature of the repository, and the negative effects due to the slightly higher overall storage temperature are limited. It is clear that this approach is possible, only if the temperature and the defect-state of the rock salt surrounding the HLW are monitored.

1.3 Relation with the central objectives of the CORA research program

This research project addresses the problems associated with the effects of the combined radiation and temperature field, due to the presence of high level waste in NaCl formations. In case of retrievable storage, as has been demanded by the Dutch Government and Parliament, we need detailed information about the development of radiation damage in the rock salt surrounding the waste canisters. To develop a situation where retrievable storage is possible is the objective in the CORA research program. We have found in our laboratory that after exposure to high doses of irradiation Rock Salt, which is under normal conditions an extremely stable compound, becomes unstable and might explode. Explosions in the vicinity of high level waste should be excluded in particular when retrievable storage is required.

An essential step in view of retrievable storage is to develop a future *regime of monitoring* in the storage site. This is crucial, because it allows us to work on: i. the further development of the physical models describing the long-term processes in the storage site (including radiolytic processes in Rock Salt), and ii. confidence building and proving on the basis of a real one-to-one in-situ experiment that safe storage of HLW in Rock Salt is possible.

1.4 The accelerator setup

Before we were able to use the irradiation facility a lot of work had to be done. This work had the highest priority, because the success of this research project was depending fully on the operation of this equipment.

The irradiation source consists of a 500 kV LINear electron ACcelerator (LINAC), driven by the high voltage produced by a cascade generator, which is enclosed by a steel tank and placed (for reasons of radiation safety) in a bunker. The advantage of the LINAC setup is that there are only a few moving parts within the accelerator, which means that the long-term dependability of the machine is very good. Before the start of the project several parts of the setup had been tested. The high voltage source, which provides 30 kV (20 kHz, AC) necessary to feed the cascade generator, needed several modifications, because it appeared that it produced high frequency plasmas in the open air.

After several successful irradiation runs had been carried out, the accelerator broke down during an irradiation run. From the tests performed on the instrument it appeared that the failure was due to defect parts inside the accelerator tank. After opening the tank we found that there was extensive damage. After a few weeks we were able to establish the cause of the failure. Several parts of the accelerator were damaged and should be replaced. In addition, it was decided to modify the machine with respect to a few parts in order to avoid similar situations in the future. After these modifications the mechanical ruggedness of the accelerator system has been improved and an electronic modification prevents that large

instantaneous forces are exerted on parts within the accelerator tank when the machine is started.

1.5 The irradiation runs

The irradiation runs in this project were aimed at producing many different highly damaged materials with sufficient void formation, because the first priority of the present project is to obtain additional information about radiation-induced voids. In line with this we have chosen to start with relatively long term irradiation experiments, which have provided us with a reasonable number of heavily irradiated samples.

When the irradiation runs were in progress we decided that slight changes from the initially proposed irradiation schemes would provide us with interesting additional information. The objective to produce large numbers of heavily irradiated samples remained unchanged. We decided that it would be more effective to apply different dose rates in order to obtain additional information about dose rate effects. In order to reach this goal, we have split the irradiation runs into different stages. In stage 1 we have irradiated a set of samples at a fixed temperature (100 °C) with a fixed dose rate until we passed the nucleation stage. In stage 2 we have irradiated the same samples to a certain extra dose, but we have split the set of samples into two different groups. These groups were irradiated at two different dose rates at different fixed temperatures between 50 and 150 °C. The difference between the results of the two groups is a measure for the dose rate effect.

1.6 The target plate

The target plate, used until now to accommodate the samples, has some disadvantages. In the first place due to the limited possibilities to apply sufficient cooling, the range of dose rates is too limited. At high dose rates the amount of heat, which should be removed from the target area is large. In this project we want to study samples, which had been irradiated at fixed temperatures between 50 and 150 °C and therefore a suitable temperature control is necessary. From an extensive investigation of the sample holder, which was used until now, we concluded that the flow of cooling liquid should be increased significantly. At the same time the old target plate showed from time to time leakage of cooling liquid, as a result of weak seals. In the new design of the target plate we have reduced the number of seals to an absolute minimum.

1.7 Dosimetry

In the past, a point of concern has been the question regarding the dose rate produced by the electron beam. Until now we have employed the method published by Berger and Seltzer, which is used extensively in the present literature. The method of Berger and Seltzer takes into account the loss of energy of the high-energy electrons in the sample. We have concluded that this method does not account for eventual effects associated with the presence of the Al-target plate in which the samples are accommodated. These effects lead to deviations in the dose rate from the Berger and Seltzer values. In this research project we have designed a new model for the calculation of the dose rate in which the secondary effects due to the target plate are included.

1.8 The theoretical model of radiolysis of NaCl

As mentioned above, it is necessary to develop a consistent picture of the processes that go on in rock salt during irradiation. Without a dependable model it is impossible to draw any conclusion about the development of radiation damage under storage conditions in the rock salt in the vicinity of a canister with HLW, because realistic laboratory experiments would take several hundred years. By means of new models we should account for the role of all relevant defect types, which are involved in the damage formation process. This implies that we have to consider the creation and growth of the Na and chlorine precipitates and the voids.

Until now the role of voids was not taken into account, because this is impossible within the framework of the various Jain-Lidiard type radiolysis models. The difficulty appeared to be the creation of electroneutral vacancy pairs. During this research project we have definitely made significant progress in this respect. We were able to design the model in such a way that in the process Na and chlorine precipitates are created along with voids. In addition to this, we now understand that at moderate irradiation temperatures V_K and V_F-centers (just as observed in the literature) are formed in stead of only H-centers. V_K and V_F-centers are formed as a result of a reaction of highly mobile H-centers with dislocation lines or loops.

At the end of this CORA research project we have a rather general (and possibly too crude) model for the description of the radiolysis processes in NaCl. This model needs further refinement. Several steps in the process need further verification, but the most significant step ahead is that we have (in contrast with the Jain-Lidiard type models) the possibility to include voids into our considerations.

1.9 Production of colloids, chlorine precipitates and voids

During the advanced stages of the radiolysis process three different types of extended defects are formed: Na-colloids, chlorine precipitates and voids. All three types have been investigated in this research project. Some extra work has been done on voids and chlorine precipitates, because in earlier projects we have focused our attention mainly at the properties of Na-colloids. In addition, we have reached the conclusion, that most certainly the chlorine precipitates play a central role in the production of radiation damage in NaCl. First, chlorine precipitates are difficult to accommodate in the NaCl lattice, because they need extra space. Secondly, the most essential steps in the radiolysis processes involve chloride ions or holes in the chloride sub-lattice. As compared to the information on radiolytic Na we have only little information on chlorine precipitates. This is due to the fact that there are not many techniques available that provide detailed information about these precipitates.

In the past we have obtained evidence that two Raman scattering peaks in heavily irradiated NaCl can be ascribed to extremely fine chlorine precipitates (H.J. van Es and H.W. den Hartog). In earlier reports we have reported to OPLA about the melting peaks of extremely small chlorine bubbles in heavily irradiated samples. In this research project we have increased our knowledge on the formation of chlorine precipitates in NaCl during irradiation. We have observed interesting effects, associated with these precipitates, which yield information necessary for the description of the radiolysis processes in these materials.

In particular voids are important defects, because we have evidence that they play an essential role in the processes leading to the explosions observed in heavily damaged NaCl. Samples with large voids turned out to be unstable as compared to samples, which contain only small

voids. The volume percentage of the voids reaches values of about 10%, which implies that the formation of voids is one of the central steps in the radiolysis process in NaCl. We have for the first time determined the production of voids as a function of the dose. This means that we are now able to compare the results for the voids with those obtained for Na-colloids.

1.10 Effects of impurities

In the past we have investigated the effect of impurities on the amount of stored energy. Also we have carried out research to find the relationship between the presence of impurities and the production of Na-colloids. As an example we mention the observation that in KBF_4-doped NaCl samples the production of Na-colloids is rather high, whereas in pure NaCl and Br doped samples there are much less colloids. Now we have obtained experimental data on the correlation between the presence of impurities and the production of voids and cracks, which appears to have the most crucial effect on the mechanical stability of the material. We are able to present an explanation for this observation, based on a new concept of the radiolysis process, which has been developed in the present project.

1.11 Effects of the dose: saturation?

In the past we have carried out many experiments to find the relation between the dose and the amount of stored energy (evt. the latent heat of melting of the Na-colloids). There were several samples, especially those showing large quantities of stored energy that did not reveal saturation of the amount of stored energy as a function of the dose. This behavior was shown to persist up to large percentages of Na-colloids. On the other hand there were some samples which showed clearly sub-linear behavior, although it was uncertain that this behavior was the precursor of real saturation. The experimental information, which was available at the beginning of this research project shows clearly that there is definitely no general trend of the radiation damage to saturate with increasing doses as suggested by Gies [2], and Soppe et al [3]. In some exceptional cases we have indeed observed some evidence for possible saturation, but this behavior is limited to some isolated cases.

In terms of the storage strategy it is practical to know if there are particular samples that may show saturation of the amount of stored energy/colloid fraction as a function of the dose. This would mean that the radiolysis process is inhibited significantly, especially when we are dealing with large doses (and stored energy values). Our new results fully support the existing data, and it appears, that even in some cases where an eventual onset of saturation of the colloid concentration has been observed the overall damage keeps increasing with increasing doses! It will be shown in this report that in the crystals showing saturation of the concentration of colloids, sometimes extra (large) voids were produced, resulting in highly unstable samples. An example of this type of behavior is NaCl:Ba, which contains relatively small concentrations of colloids. On the other hand the shape of the voids indicates that they are quite unstable. This implies that one has to be extremely careful drawing conclusions about eventual saturation effects. On the other hand the effect of saturation may offer possibilities for the development of smart backfill materials, which can be used as an intermediate between the HLW canisters and rock salt. These are reasons why these materials have received extra attention in this project. The observations for NaCl:Br look particularly promising from this point of view because both the colloid fraction and the numbers of voids and their average sizes are small.

1.12 Effects of the irradiation temperature

In earlier research projects we have shown that the production of radiation damage, e.g. colloids depends sensitively upon the irradiation temperature. We have also shown that the temperature behavior of the damage formation depends on the presence of impurities [6-8]. In general there is a maximum of the damage production at about 100 °C, at low temperatures, i.e. below 50 °C the production of damage is small, and at high temperatures the formation of colloids depends strongly upon the presence of impurities. When pure NaCl is irradiated, there is a high temperature cut-off, which means that the colloid production at high temperatures is small. The same applies to several kinds of doped samples. On the other hand we have found that several other NaCl samples doped with particular impurities do not show this high temperature cut-off. For these materials the formation of radiation damage takes place up to the highest irradiation temperatures that have been investigated (i.e. 150 °C). Prior to the start of this project we have obtained interesting information about the production of colloids, but the corresponding information about chlorine precipitates and voids was not available. For the evaluation of the safety problems associated with the formation of radiation damage we need information about the production of voids as a function of the irradiation temperature. Similarly, information about the details of the production of chlorine precipitates is needed because it will help us to further develop the radiolysis model for pure and doped NaCl crystals. Suitable, verified physical models will ultimately allow us to estimate the radiation effects of storage of HLW in different types of rock salt samples.

1.13 Effects of the dose rate

The radiolytic reactions taking place during irradiation are usually strongly temperature dependent. This applies to the processes in which the mobility of defects is involved but it applies also to many other processes. The damage formation process can be regarded as a delicate sum of many different temperature dependent reactions. When the dose rate is increased, the most obvious result will be an increase of the concentration of the primary radiation induced defects. As a result the concentrations of all defects involved in the radiolysis process will change and the ultimate result will be that the colloid concentration and the total void volume change. These effects are usually called dose rate effects. According to the Jain-Lidiard model the dose rate effects are appreciable. When the dose rate is decreased by a factor of 10 and when at the same time the irradiation time is increased by a factor of 10, i.e. when the same total dose is applied, the concentration of colloids may increase by a factor of 3. In this project we will try to establish eventual dose rate effects. In practice this is difficult and most of the earlier experiments were not suitable to find eventual dose rate effects, because the irradiation experiment was in the stage where nucleation of colloids takes place. In order to establish dose rate effects we need long-term irradiation experiments combined with well-chosen experiments at high dose rates. During this stage of the irradiation experiment the fluctuations in the efficiency of the damage formation process are quite large. The information, which will become available as a result of the present project will definitely not sufficient to draw conclusions about these dose rate effects.

2 GOALS OF THE PROJECT

We have defined several goals for this research project, which are all connected with the central issues of the CORA research program. In addition, it should be noted that at the end of the OPLA research program there were several questions with regard to the subject of radiation damage, which were unanswered. It is an important task to find during this project as many answers as possible for these questions.

2.1 Goal 0: Preparation of the irradiation facility

Before we were able to use the irradiation facility a lot of work had to be done. This work had the highest priority, because the success of this research project was depending fully on the operation of this central piece of equipment.

The central part of the irradiation facility is the irradiation source, consisting of a 500 kV LINear electron ACcelerator (LINAC), driven by the high voltage produced by a cascade generator, which is enclosed by a steel tank; these part are all placed inside a concrete bunker. The advantage of the LINAC setup is that there are only a few moving parts within the accelerator tank, which means that the long-term dependability of the machine is very good. Before the start of the project several parts of the setup had been tested. The high voltage source, which provides 30 kV (20 kHz, AC) necessary to feed the cascade generator, needed several modifications, because it appeared that it produced high frequency plasmas in the open air.

Although several problems were encountered in the process to get the accelerator working, we could start the first test irradiation in time. The operation of the machine was as expected and several long runs have been carried out without any difficulty, until February 1999 when the accelerator broke down and we faced a delay of several months. This occurred at a crucial moment, because after the irradiation runs we needed sufficient time to analyze the large numbers of samples with a variety of experimental techniques. After a reconstruction of some of the parts of the LINAC we have irradiated samples without any further difficulties.

2.2 Goal 1: Investigation of voids

Radiation-induced voids have been investigated only in a limited group of materials. These materials are found predominantly in the class of crystalline metals [9, 10]. In these materials one sometimes found ordered structures of voids, which have received a great deal of attention in the recent literature [11-12]. Insulators have been investigated to a much smaller extent [9]. Here too, in several cases one has observed (e.g. CaF_2 [13] and Al_2O_3 [14]) ordered structures of voids. Radiation-induced voids in NaCl have been investigated in Groningen, and not anywhere else. Although there was some kind of order in the voids, we did not observe the ordered structures of voids like in CaF_2. At low damage concentrations the voids are usually small and more or less round. Sometimes they appear to be slightly faceted. The only indication of ordering was the fact that in heavily damaged samples large voids (which are combined with large void volume fractions) were not spherical objects, but elongated along the principal axes (i.e. the <100> axes) of the NaCl lattice.

2.3 Goal 2: Smart backfill materials

An valuable option in the management of high-level radioactive waste is the development of, or the search for, suitable materials, which are more resistant to radiation fields than natural rock salt. Of course these resistant properties should be in terms of both colloid and void formation. From previous investigations we know that in NaCl samples doped with small amounts of NaBr relatively small concentrations of colloids are formed. In addition, the radiation-induced stored energy in these samples is relatively small. The production of colloids and voids can be monitored by means of experimental techniques (ESR, DSC and SEM). We note that in this project the experiments have been carried out on samples, which have been irradiated under laboratory conditions, i.e. high dose rates. Laboratory experiments at low dose rates and high total doses are practically impossible, because these irradiation experiments would take several hundred years. This implies that also for these smart backfill materials a suitable model should be developed in order to extrapolate the lab results to storage conditions.

We have found samples, which show low colloid fractions as well as low void volume fractions. Therefore, we are at the present moment optimistic that there will be suitable backfill materials, which are needed to fight undesired radiation effects in the vicinity of HLW. We note that this remark is a preliminary one, because it is based on a rather limited number of (high dose rate) laboratory observations. Obviously, a lot of work should be done to establish whether our optimism can be extended to the situations existing in storage facilities.

2.4 Goal 3: Relation with future monitoring of storage sites

From the point of view of the production of radiation damage the development of monitoring techniques for retrievable storage of HLW is a quite natural thing to do. In fact there are no possibilities to carry out laboratory experiments on radiation damage under conditions similar to those in a storage site. In these situations the most effective approach is to investigate as closely as possible the general features of the radiation damage formation processes and add at a later stage well-chosen and well-defined monitoring experiments under controlled conditions in storage sites. The experiments during monitoring are aimed at avoiding undesired situations with regard to radiation damage. The experimental observations in this project will help us to choose the most promising conditions and materials.

In the present research project we have investigated the development of Na colloids, chlorine precipitates and voids as a function of the dose, irradiation temperature and the presence of impurities. These investigations have provided us with necessary information, which can be helpful in a monitoring process. For example, we have obtained information about the conditions (such as colloid percentage or void size, shape and volume) giving rise to explosions in the irradiated samples. In addition, further experiments in this direction might allow us to recommend particular measures such as local heating in order to release the stored energy in a controlled way.

3 ACHIEVEMENTS DURING THE PROJECT

In January 1998 we started immediately with the work necessary to improve/modify our irradiation facility. In addition, we were already for some time in close contact with several scientists of the NSC-KIPT in Kharkov (Ukraine), who were willing to help us to bring this project to a successful end. These scientists, Dr.'s Dubinko and Turkin, are highly experienced in the area of voids, void structures and radiation effects. At later stages we have expanded our collaboration with NSC-KIPT, and also Prof. Gann from Kharkov has given valuable contributions to this research project.

3.1 Goal 0: Preparation of the irradiation facility

3.1.1 The accelerator

Before we were able to use the irradiation facility a lot of construction work has been done. This work had the highest priority, because it was clear that the success of this research project depends fully on the dependable operation of the irradiation equipment. A brief description of the work on several parts of the accelerator system and the other parts of the irradiation facility is given below.

The irradiation source consists of a LINear electron ACcelerator (LINAC), driven by the high voltage produced by a cascade generator, which is enclosed by a steel tank and placed (for reasons of radiation safety) in a bunker. The advantage of this setup is that there are only a few moving parts within the accelerator, which means that the long-term dependability of the machine is very good. Before the start of the project several parts of the setup had been tested. The high voltage source, which provides 30 kV (20 kHz, AC) necessary to feed the cascade generator, needed several modifications, because it appeared that it produced high frequency plasmas in the open air.

Another problem, associated with the application of 30 kV (AC), has been solved completely during the first stage of this project. It appeared that the feedthrough, which allows this AC voltage to be applied to the cascade generator inside the accelerator tank, is dielectrically not strong enough. After 100 – 200 hours of operation it breaks down and should be replaced. We have investigated the possibilities to use more suitable feedthroughs and we have found a useful possibility. This type of feedthrough is capable to withstand the high frequency, high voltage conditions occurring in our accelerator system during long-term operation (i.e. several thousand hours) and it has been working without any problems during this project.

In the beginning the cascade generator, which is used to produce the high voltage (up to 500 kV DC), showed sparks. After the occurrence of the sparks often many of the electronic components were damaged and should be replaced. These components are located inside the accelerator tank and in order to replace these parts, we had to open the tank and the expensive gas mixture in the tank was lost. The first task was to prevent these sparks completely. The cascade generator and the damaged electronic components are located in a metallic tank, which is filled with a dry mixture of 80% nitrogen and 20% carbon dioxide. The sparks could be prevented effectively by the addition of 10% sulfur hexafluoride to the gas mixture. In addition, we have reduced the probability of the occurrence of sparks by polishing the metallic parts of the cascade generator and the accelerator tube and by removing the sharp

edges inside the accelerator tank. Finally, the damage of the sparks to the different electronic components could be reduced drastically by the application of electronic suppression, using suppressor diodes. With these modifications we have used the accelerator a long time without any difficulty.

The electron beam produced by the accelerator can in principle be set to values up to 500 kV and 1 mA. The voltage and the current can be adjusted by means of the beam control unit in the accelerator control cabinet, which is located outside the bunker. This beam control unit has been developed in our laboratory. The actual value of the beam current depends strongly upon the settings of the heating coil of the electron-emitting cathode of the electron gun and the electric field lines in the vicinity of the cathode. In order to adjust the settings to the optimal values we have used a trial and error method, which resulted in a maximum beam current of 0.7 mA during the first stage of the project and a maximum voltage of 500 kV. This was quite sufficient for the irradiation runs planned for this part of the project. Further improvements have been obtained later. As soon as we had to open the accelerator tank we have made the necessary modifications and obtained (as specified) the maximum beam current of 1 mA.

With the above-mentioned LINAC system we are able to irradiate a target area of 320 cm^2 at dose rates between 10 Mrad/hr and 1.5 Grad/hr. For thigh dose rates there are limitations due to the heat production in the target plate caused by the energy losses of the stopped electrons. When high dose rates are applied, the temperatures of the sub-targets cannot be controlled in the planned temperature interval 50-150 °C. In order to solve this problem we have introduced a new, strongly cooled sample holder in the final stage of the project.

3.1.2 The vacuum system

In order to irradiate the samples, we need high vacuum (about 10^{-7} Torr) in the accelerator tube and in the target area. Our vacuum system has been designed and constructed (fig1) and it is part of the radiation safety control, mentioned below. It includes valves and measuring devices, which can be controlled fully by the vacuum controller in the control cabinet outside the bunker (fig2). In addition, the vacuum control system is integrated in the PLC system of the accelerator setup.

3.1.3 The beam steering system

A major part of the construction work was to align the electron beam produced by the accelerator system. The first alignment of the system has been obtained with laser beams, which were adjusted to coincide with the main axis of the accelerator setup. Ultimately, we have optimized the alignment by using the electron beam. It was possible to make some necessary final mechanical adjustments in order to align the beam exactly along the main axis of the accelerator. It appeared however that these adjustments were too crude and they were insufficient to assure that the electron beam would pass the magnetic beam sweep unit in the irradiation cell and reach the target plate as planned. In order to achieve this goal we have designed an electrostatic beam steering system, which allows us to direct the beam accurately through the magnetic beam sweep magnets.

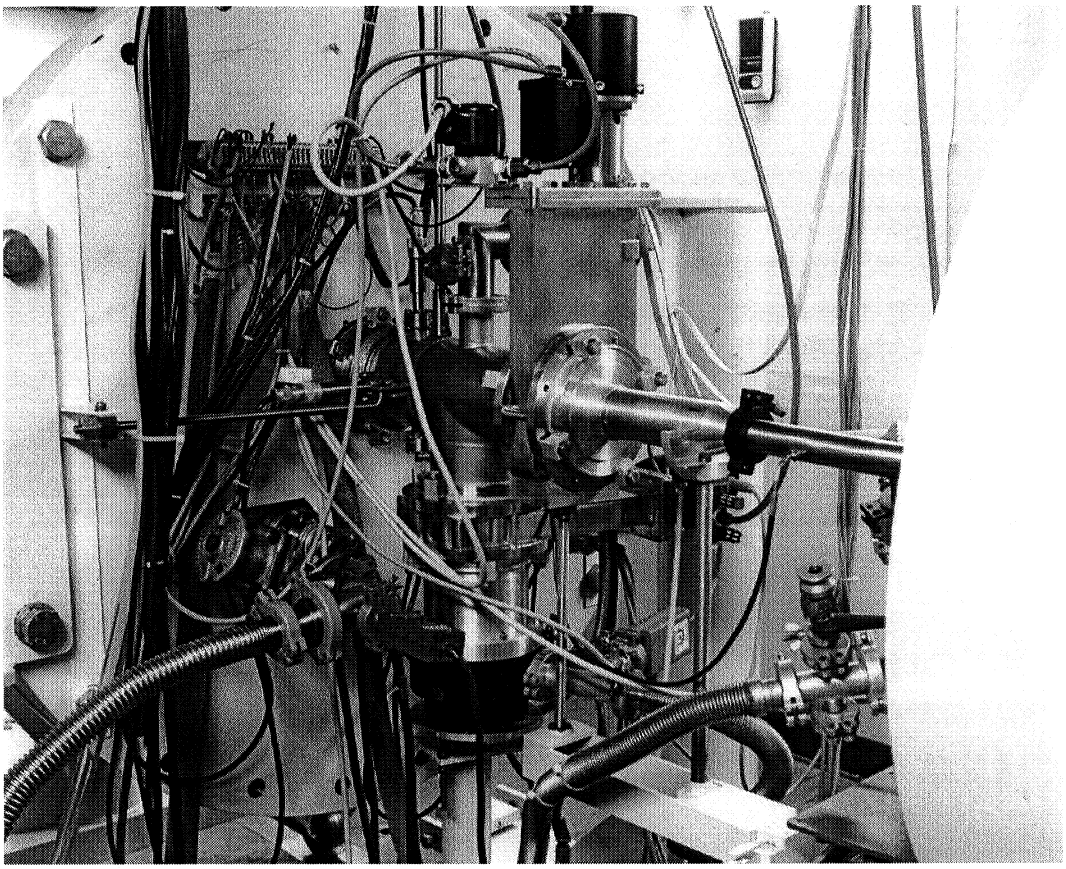

Figure 1. The picture of the part of the high vacuum system of new LINAC.

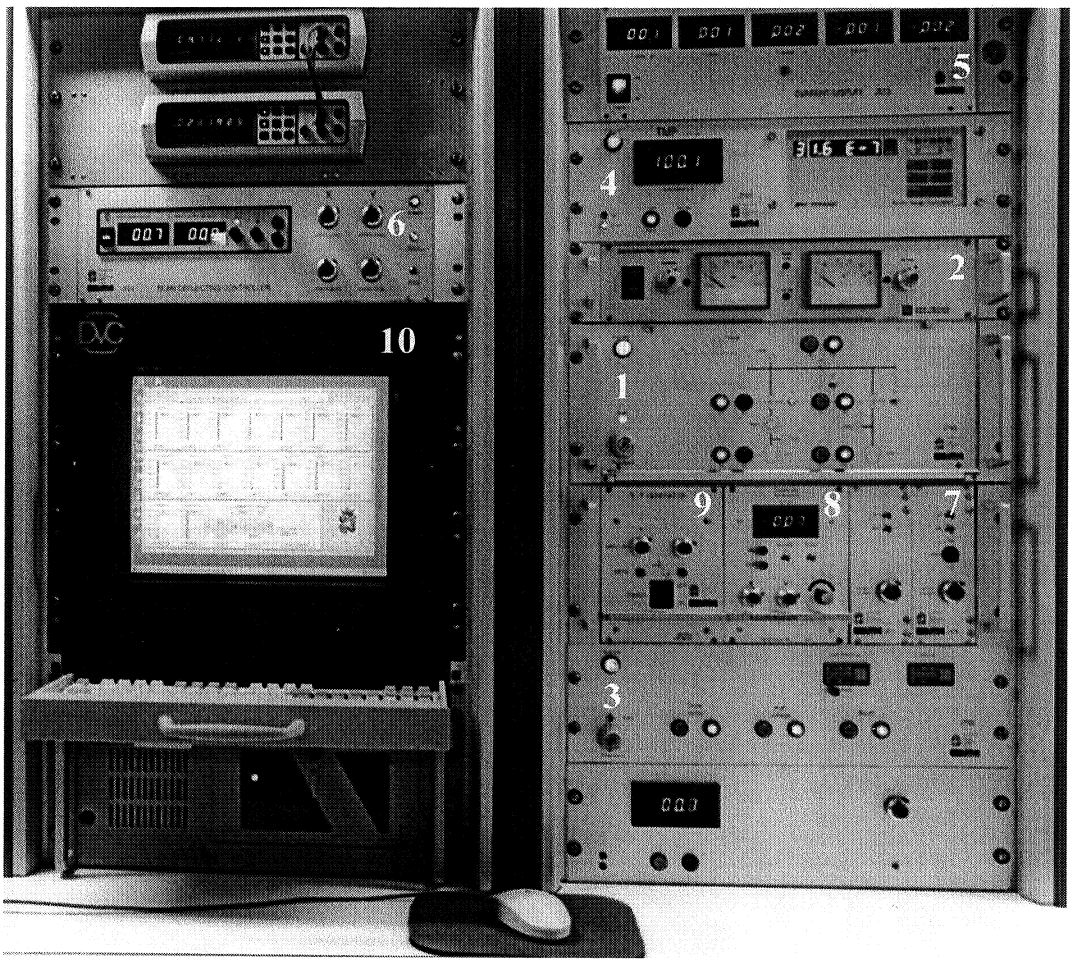

Figure 2. The control cabinet of the new accelerator.

1. PLC and safety control systems. 2. High voltage control unit 3. Main switches 4. Vacuum control system. 5. Full current control and display units. 6. Beam-deflecting controller. 7. Filament and beam currents regulation systems. 8. Beam steering electronic control system. 9. Beam sweeping control unit. 10. Computer control system.

The beam steering control consists of two parts, the horizontal and vertical part. It consists of a symmetrical power supply, which provides symmetrical voltages to both the vertical and the horizontal part of the beam steering system. For example a voltage V_h is applied to one of the horizontal beam steering electrodes, while $-V_h$ is applied to the opposite one. V_h can be adjusted between 0 and 3000 Volt. A similar situation has been created for the vertical beam steering. A voltage V_v is applied to one of the vertical beam steering electrodes, while $-V_v$ is applied to the opposite one. V_v can be adjusted between 0 and 6000 Volt. Here we need a higher value, because a relatively large initial vertical correction was necessary.

3.1.4 Beam focusing, magnetic lens

For small beam currents the diameter of the beam was several mm's, but with increasing current we have observed strong defocusing effects and the diameter of the electron beam increased to unacceptable values (between 10 and 15 mm). With these diameters is impossible for the beam to pass the beam sweeping system, necessary to obtain a homogeneous dose for all samples located in the target area of approximately 18*18 cm^2. A magnetic focusing system has been developed and constructed, which is highly effective in reducing the diameter of the electron beam. By adjusting the current in the coil of the magnetic lens we can easily reduce the diameter of the beam to values less than 0.1 mm. This applies to beam currents up to several hundreds μA, which means that after the application of this device the system works well and the electron beam passes the beam sweeping unit without problems.

3.1.5 Electronic and computer control of the accelerator

Several electronic devices and a PLC system control the operation of the accelerator. The beam current is checked at five different positions in order to provide accurate information about the real flux of electrons at the target with the samples. The current produced by the emitting cathode $I_{emission}$ is measured, but this current does not reach the target. This is due to the fact, that the electrons are stopped partly by several diaphragms in the beam line. In addition, the column current along the accelerator tube I_{column} is measured. And the numbers of electrons caught by each of the diaphragms $I_{diaphragm}$ are monitored separately. The target is a part of a so-called Faraday cup system, which allows us to measure accurately the number of electrons, which really reached the samples and contribute to the irradiation dose, I_{target}. In addition, the number of electrons passing a suppressor ring surrounding the target, $I_{suppressor}$ is measured. Because all currents are small, suitable amplifiers have been constructed to amplify them. The different current readings allow an accurate determination of the real electron flux through the samples and the corresponding dose rate can be calculated.

The irradiation runs, which had been planned for this research project, lasted several months and therefore it was useful to check the equipment during the nights and weekends by means of computers. Also the parameters, such as the dose rate, irradiation temperatures (i.e. the temperatures of the different sub-targets) are recorded by means of computer equipment. The same applies to the various safety conditions during the irradiation runs, in particular the radiation levels.

The monitoring of the irradiation conditions can be displayed at any PC, belonging to the network surrounding the irradiation facility. This means that we can from our PC at home get access to the files, which are developed by the monitoring software and we were able to see how the dose rate, the total dose and the irradiation temperatures of the different sub-targets behaved during the irradiation run (fig.3).

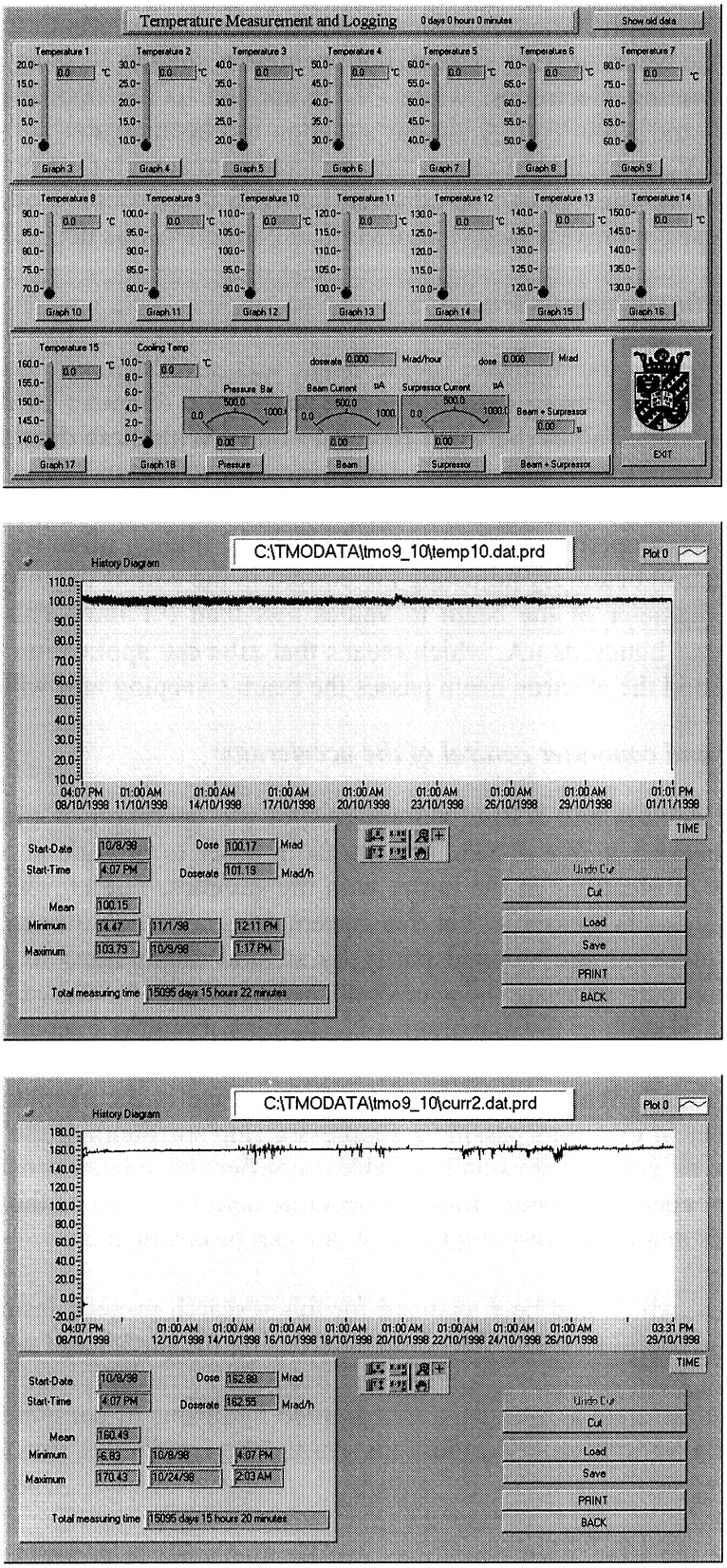

Figure 3. The monitoring of the irradiation conditions from the remote terminal. The monitoring software has been made on the basis of Lab View program.

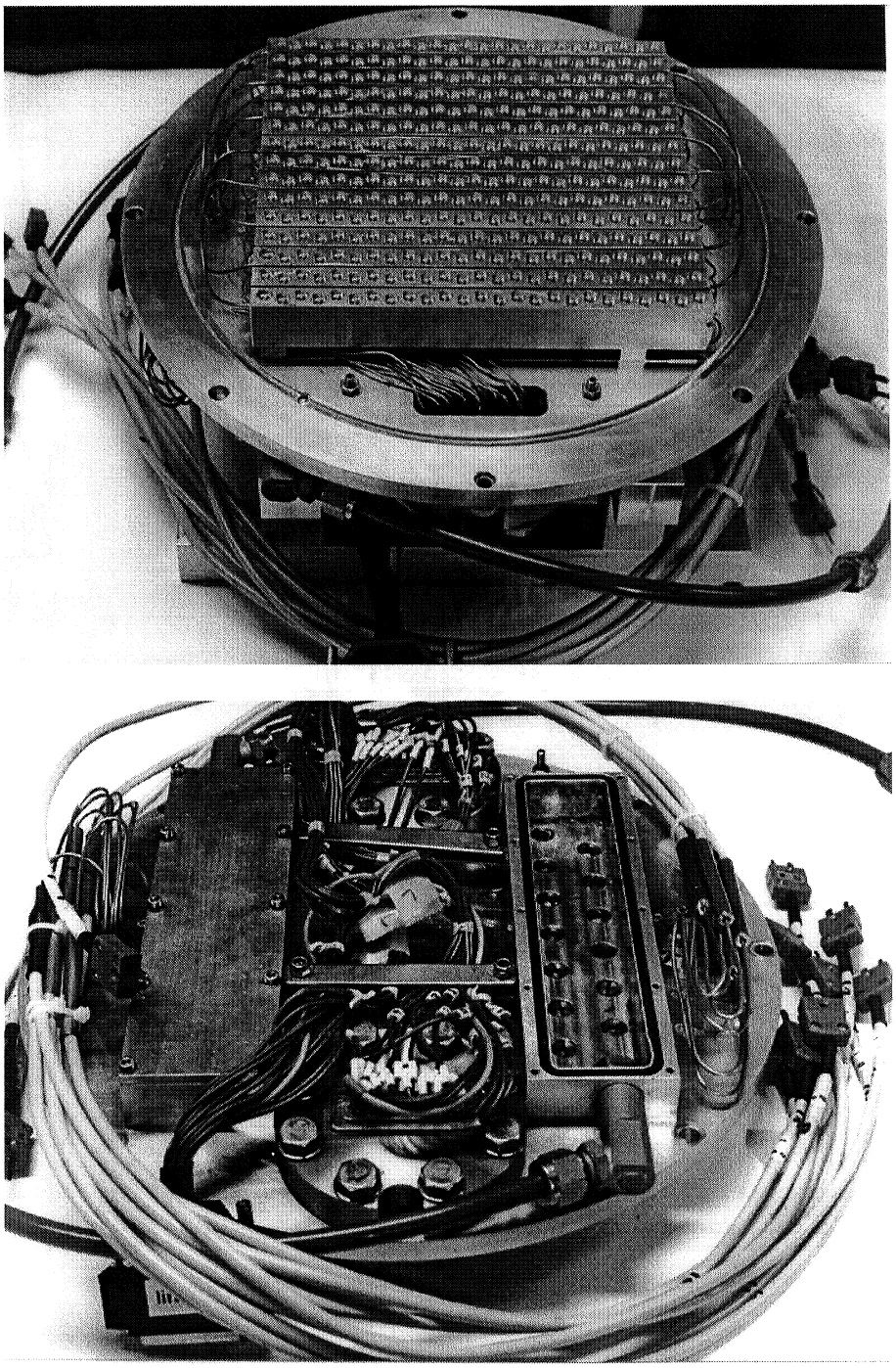

Figure 4. The front and the rear sides of the new multi-sample target.

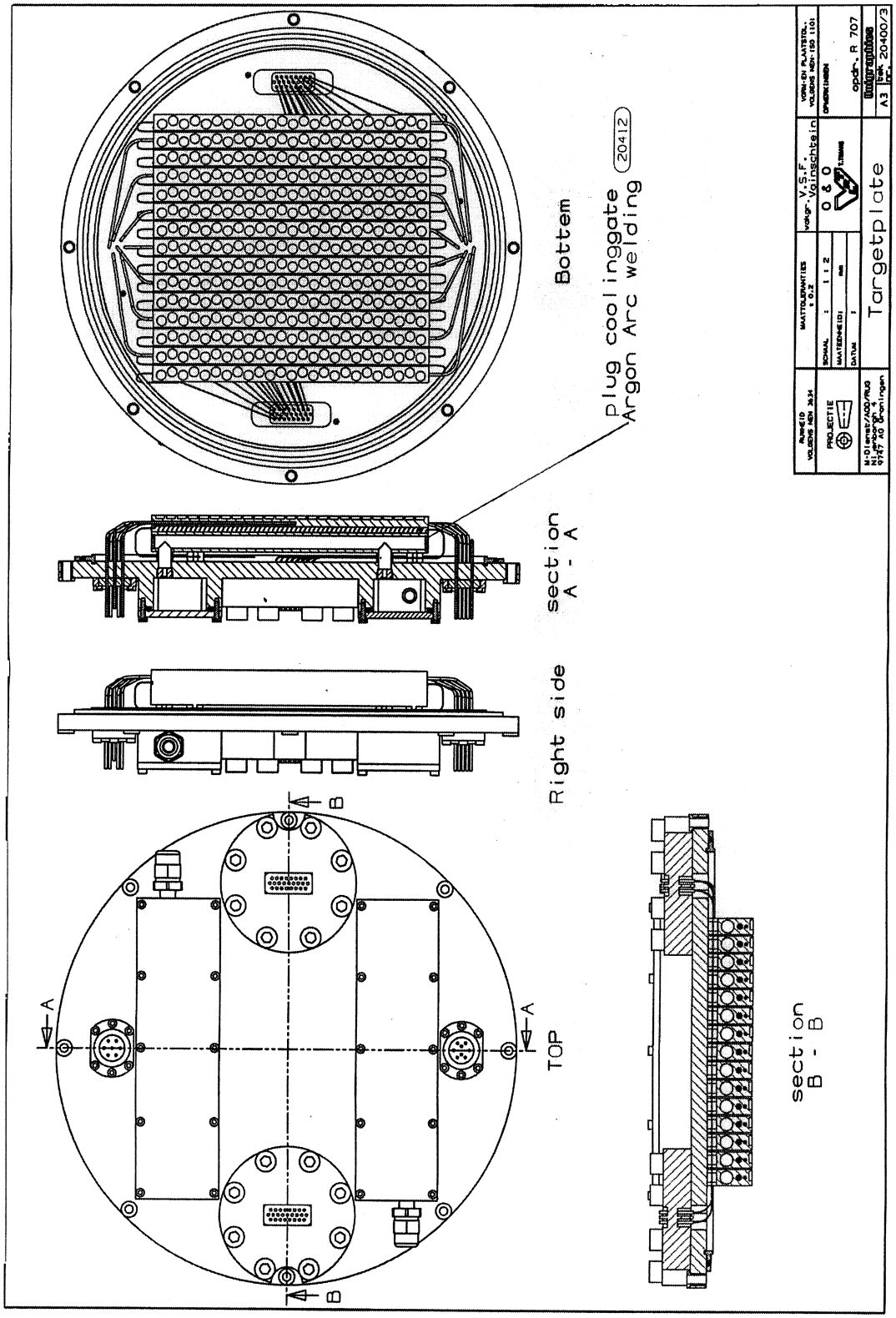

Figure 5. The working drawing of the new multi-sample target.

3.1.6 The irradiation safety

The safety and measuring hard- and software have been tested and it appeared that the programs were working properly. This means, that we were able to read the above-mentioned parameters from our computers at home and elsewhere in the lab, which makes the work with the irradiation facility much more efficient than before. In particular it is useful to be able to check the safety conditions related with the operation of the electron accelerator.

The computer system carries out checks on the radiation levels close to the accelerator. In addition, the vacuum system, the cooling devices, the gas pressure in the tank, the beam sweeping devices, etc. are under continuous control and in case one of the parameters is changed to an unexpected value, the accelerator is switched off immediately. Before the accelerator can be switched on, all parameters should have the correct values (interlock system).

3.1.7 The new multi-sample target

Although the plans for our new multi-sample target were ready in the early stages of this project, we were not able to finish this part of our setup earlier than in the last stage of the project. Welding of the different Al-parts of the multi-sample target was extremely difficult to accomplish, but finally we were successful. The most important feature of this part of the setup is, that it consists basically of one piece of aluminum metal, which implies, that it is much more reliable than the old target plate. In the old one we had to use a cooling system with many vacuum connections, which caused problems during the irradiation runs from time to time. The target consists of 15 sub-targets, which can accommodate more than 20 samples each. The temperature of the sub-targets are measured and controlled by means of electrical heaters in conjunction with PID controllers. In order to compensate the overall heat produced by the electron beam the sub-targets are cooled with water. This system is particularly useful when high dose rates are applied, because the water cooling system is much more reliable than in the old target.

Drawings of the new target, including some of the wiring, have been given in fig.4 and fig.5.

3.1.8 The test runs of the radiation facility

We have carried out several test runs with the upgraded irradiation facility. The first runs were short, with irradiation times ranging from a few minute to several hours. After testing the most critical parts of the accelerator setup, we have started a few test runs, which took a few days. All test runs so far were successful. During the test runs we have irradiated several NaCl samples. The irradiated samples looked quite normal and showed a homogeneous distribution of radiation damage. During the stage of testing we have irradiated several samples for some of our colleagues at the GSI in Darmstadt (Germany). Experiments of these colleagues on these samples turned out to be successful.

Finally, it was decided that the system was ready for the first long-term test. Unfortunately, we could not implement the new target system with its new cooling device. The irradiation has been carried out with the old target. Except for two short interruptions close to the end of the run, this experiment went well, without major problems.

The results of the test runs have shown that for the irradiation experiments, which will be carried out later it should be preferred to install new temperature control units for the 15 sub-targets. The variations produced by the existing temperature controllers are too large. At this moment we are testing several new T-control systems. It appears that these instruments give better results than the old ones. We have implemented several new systems for the old ones and after comparing the results we came to the conclusion, that new temperature controllers have to be installed for all sub-targets.

3.1.9 Dosimetry

Theoretical and experimental investigation of energy deposition profiles in NaCl platelets under 0.5 MeV electron irradiation is performed. We have proposed a new model for the calculation of the dose rate. The build-up phenomenon is shown to double increase the dose rate due to back scattered and multi-scattered electrons.

The depth distribution of absorbed dose was determined by measuring the density of stored energy in NaCl after electron irradiation with differential scanning calorimetric method.

3.1.9.1 Formulation of the problem

It is necessary to distinguish two different quantities: energy losses and energy deposition by electrons in a target. The energy loss is the specific energy, which is lost by incident electrons of the beam at a given depth, whereas the energy deposition is the specific energy dissipated by primary, δ (secondary, and so on) electrons and absorbed by the sample at a given depth. The energy losses of monoenergetic electrons due to ionization and excitation processes in thin targets can be described with the Bethe-Bloch formula [15]:

$$\frac{dE}{dx} = C\left\{\ln\left[\frac{\beta^2 E}{2I^2(1-\beta^2)}\right] - [2(1-\beta^2)^{1/2} - (1-\beta^2)]\ln(2) + (1-\beta^2) + \right.$$
$$\left. + \tfrac{1}{8}[1-(1-\beta^2)^{1/2}]^2 - \delta\right\} \qquad (3.1.1)$$

where E is the kinetic energy of electron, $\beta = \frac{v}{c} = \sqrt{1-\left(\frac{E}{mc^2}+1\right)^{-2}}$, m is the electron mass, v is the electron velocity, c is the light velocity, I is the mean excitation energy, Z the atomic number, A is the atomic weight, $C = 2\,\pi\, m\, c^2\, r_0^2\, Z\, N_A\, \rho / A / \beta^2$, r_0 is the classical radius of electron, N_A is the Avogadro number, ρ the matter density, and δ is the density correction. Tables of δ - correction and experimentally derived I-values were published by Seltzer and Berger [16] (for NaCl, the recommended value is $I = 175.3$ eV).

The calculation of energy losses by electrons in thick target is rather sophisticated problem. The main difficulty arises from the back scattering and multi-scattering of electrons in the matter. Hence, it is necessary to take in consideration the δ-electrons when calculating the energy deposition profile. Spencer [17], Rao [18], and Kobetich and R. Katz [19] performed extended analytical calculations of energy loss profiles for the normally incident electron

beam and for a flat surface. A lot of calculations have been carried out in the literature using the Monte-Carlo method [20] in the computer simulation of the electron transport in matter.

3.1.9.2 Energy loss profile

The most complete calculations of the dissipation of energy of normally incident beams of electrons in matter have been made by Spencer [17]. Rao [18] derived a simple formula for the fraction of incident electrons of energy E transmitted by an absorber of thickness t:

$$\eta = \frac{1+\exp(-gh)}{1+\exp[g(t/R-h)]} \tag{3.1.2}$$

where $g = 9.2Z^{-0.2} + 16Z^{-2.2}$ and $h = 0.63Z/A + 0.27$. The dependence of transmission η on the sample thickness t, calculated on Eq.3.1.2 for 0.5 MeV electron beam in NaCl is displayed in Fig.6.

The point at which the extension of the linear region meets x-axis is defined as a *practical* (or *extrapolated*) *range* R_P, whereas the point were the tail meets x-axis is known as the *maximum range* R_0 (the background is neglected).

The energy loss profile of normally incident beam of electrons one can calculate as [19]:

$$S = \frac{d[\eta E(R-t)]}{dt}. \tag{3.1.3}$$

Here $E(R)$ is the energy-range relation.

3.1.9.3 Range-energy relation for electrons

The maximum range of electrons in matter can easily be calculated in the continuous-slowing-down-approximation (CSDA):

$$R_0(E) = \int_0^E \frac{dE'}{\left(\frac{dE'}{dx}\right)_{tot}}, \tag{3.1.4}$$

here $\left(\frac{dE'}{dx}\right)_{tot}$ is the value of total energy losses for electron of energy E'. R_0 is the total path length traveled to rest. Extended tables of CSDA ranges of electrons in many materials and compounds were published by Seltzer and Berger [16].

3.1.9.4 Energy deposition profile

Experimental energy deposition profiles are shown in Fig.7 for aluminum. The energy deposition profiles as well as the energy loss profiles have the pronounced maximum.

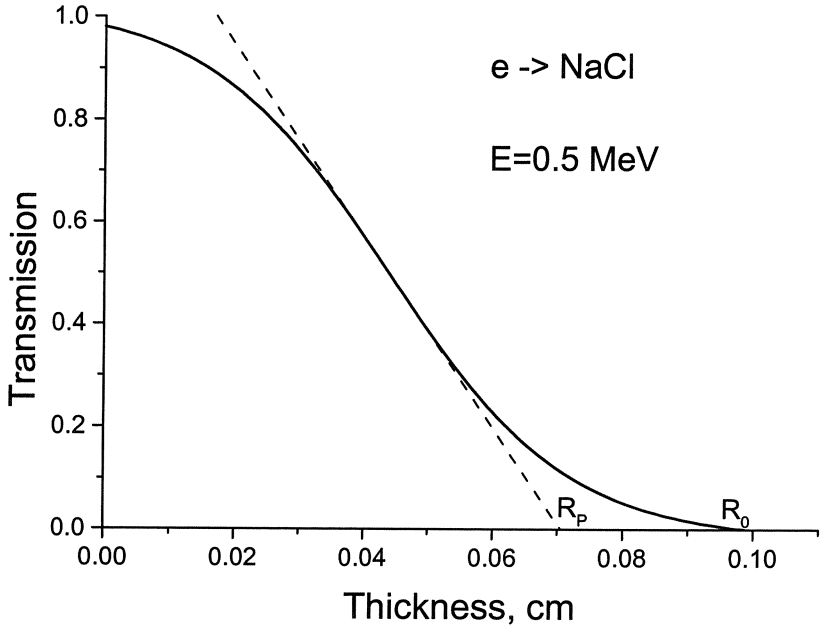

Figure 6. Dependence of beam transmission on thickness of NaCl sample

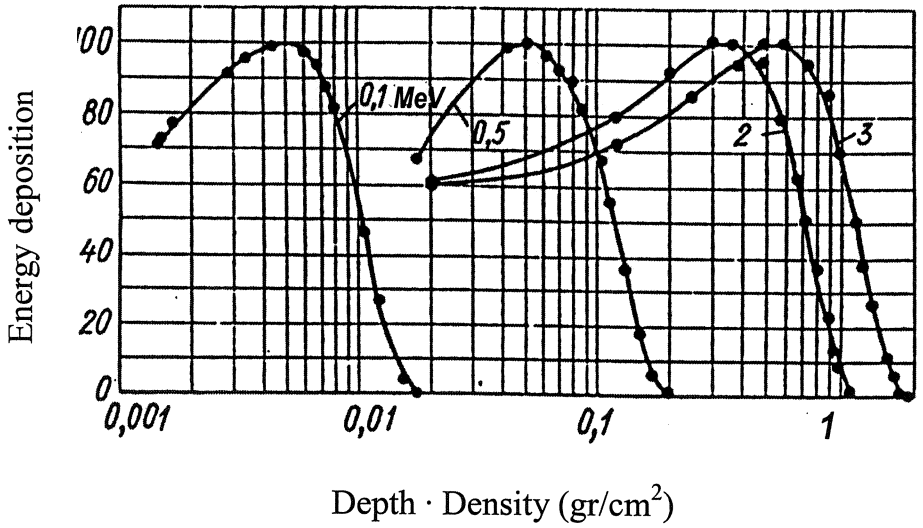

Fig.7. Energy deposition profiles in aluminum.

The calculation of the electron beam energy deposition in a target is a rather complicated problem because of multiple scattering of electrons by atoms and the appearance of δ-electrons. The Monte Carlo simulation method is used for evaluation of the energy deposition profile in 3d geometry. But the Monte Carlo is a time consuming method. So, for a quick evaluation we have developed a simple semi-empirical method for calculation of electron beam energy deposition $Q(x)$, based on a well-measured energy deposition profiles for flat-parallel electron beam in aluminum.

3.1.9.5 Universal profile approximation

It is seen from Fig. 8 that in the 100 KeV - 3MeV energy region, the energy deposition profile $Q(x)$ can be easily scaled in x by the value of practical range $R_P(E)$ and expressed in terms of the universal function $P(\xi)$ (see Fig.8)

$$P(\xi) = \frac{1.065}{\{ch[0.95(2.295\xi - 1)]\}^{1.8}[0.5 + 1/(2.7 - 2.295\xi)]} \tag{3.1.5}$$

Here ξ is depth x, scaled by the extrapolated range, $\xi = x / R_P(E)$. The values of parameters were obtained by fitting to experimental data (Fig. 7) Function $P(\xi)$ is normalized as $\int_0^\infty P(\xi)d\xi = 1$. One can calculate the electron range in aluminum $R_{Al}(E)$ using Eq. (3.1.4). For other materials, having atomic number Z and atomic mass A, the electron range can be found in ref. [2] or can be evaluated using the following scaling law

$$R_P(E) = 0.482\,(A/Z)R_{Al}(E)\,. \tag{3.1.6}$$

So, the energy deposition profile for MeV-energy electrons can be expressed as

$$Q(x) = \frac{E}{R_P(E)} P\left(\frac{x}{R_P(E)}\right). \tag{3.1.7}$$

A computer code PROFILE for a calculation of the dose-depth distribution under electron irradiation has been designed. Two versions of the code PROFILE have been tested. In the first one, called as DOSE_E1, the energy deposition profile $Q(x)$ was calculated, using the aluminum-based range-energy relation (3.1.6) for the practical range $R_P(E)$. In the second one (DOSE_E2) the practical range was assumed as $R_P(E)$=0.85 $R_0(E)$, where $R_0(E)$ was taken from S.Seltzer and M.Berger tables [2]. The both versions gave similar results.

3.1.9.6 Analysis of the approximation validity

The comparison of profiles, calculated by Eqs. (3.16-3.1.7) (labeled as PROFILE), with experimental data is shown in Fig 9. A good agreement between experimental and calculated values in Fig. 9 is not surprising because the energy deposition profile $P(\xi)$ was calibrated, using data on aluminum.

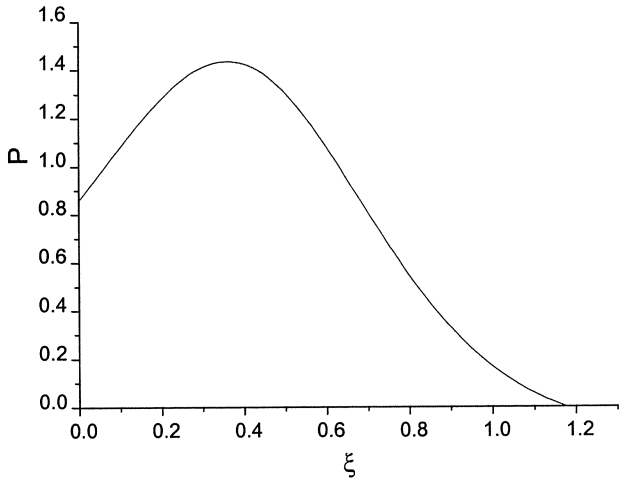

Fig. 8. The universal profile of energy deposition.

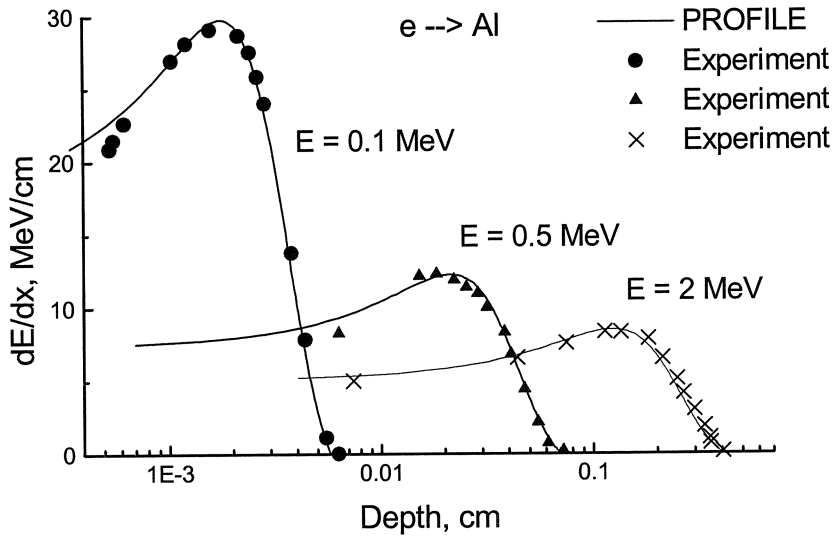

Fig.9. The energy deposition profiles in Al, comparison with experiment

3.1.9.7 Average absorbed dose calculation

Having the $dE/dx = Q(x)$ profile, we can calculate the average energy deposition $(dE/dt)_{av}$ for the sample of given thickness t:

$$\left(\frac{dE}{dt}\right)_{av} = \frac{1}{t}\int_0^t Q(x')dx' \tag{3.1.8}$$

The dependence of average dose $\left(\frac{dE}{dt}\right)_{av}$ on sample thickness t for NaCl irradiated with 1.3 MeV electrons is shown in Fig. 10a. The broken lines show the RMS deviation from average dose: $\left(\frac{dE}{dt}\right)_{av} \pm \Delta\left(\frac{dE}{dt}\right)$ where

$$\Delta\left(\frac{dE}{dt}\right) = \sqrt{\frac{1}{t}\int_0^t \left[\left(\frac{dE}{dx'}\right) - \left(\frac{dE}{dt}\right)_{av}\right]^2 dx'}, \tag{1.3.9}$$

It is interesting to compare the energy deposition profile $Q(x)$ with energy losses, calculated by formula (3.1.1). In Fig.10a the average values of deposited energy are plotted together with energy losses, calculated on formula (3.1.1) with I =13.6 Z (as Bethe-Bloch), with I =175.3 (as Seltzer-Berger) [17] and Levy's value [18]. One can see that taking into account the build-up of energy deposition due to back scattering and multi-scattering of electrons results in an increase of the irradiation doses of approximately 100% (fig. 10b).

3.1.9.8 Comparison of experimental and theoretical results

Experimental investigations of energy deposition profiles in NaCl platelets under 0.5 MeV electron irradiation have been performed. The depth distribution of the absorbed dose was determined by measuring the density of stored energy of radiation damage, which arose in NaCl after electron irradiation. The stored energy was measured using the differential scanning calorimetry method.

Three sets of NaCl + 0.1 mol % K samples were irradiated at Groningen electron accelerator. The parameters of the irradiation run have been shown below.

Electron beam energy	0.5 MeV
Beam current	210 μA
Irradiated area	306 cm^2
Irradiation temperature	100 °C
Irradiation time	10 d 15 h 9 min
Density of current	0.686 $\mu A/cm^2$
Fluence	0.63 C/cm^2
Max. thickness of samples	1.25 mm

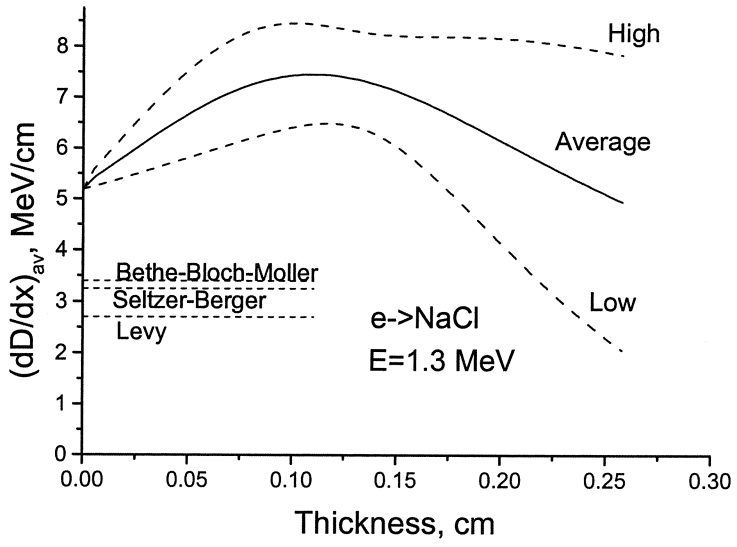

Figure 10a. Comparison of the average energy deposition profile with average energy losses for 1.3 MeV electron irradiation.

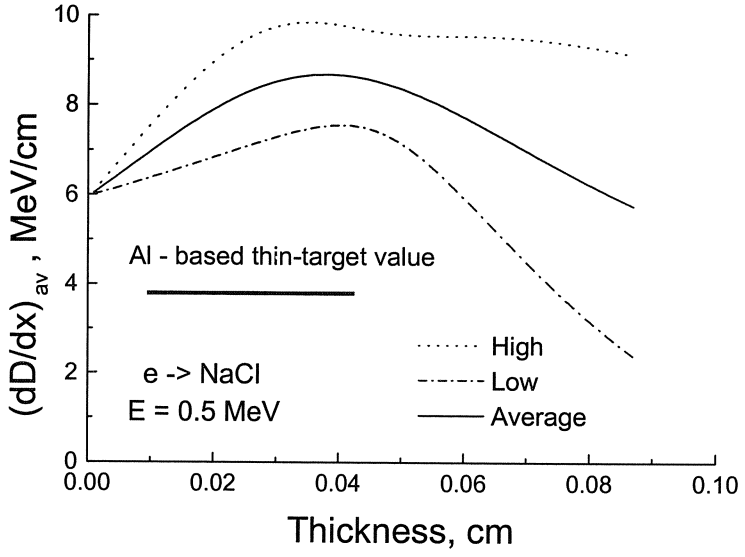

Figure10 b. Calculation of the average deposition profile with and without taking in to account the effect of the back scattering and multi-scattering electrons for 0.5 MeV electron irradiation

In the first set there were the samples of different thickness from 0.3 to 1.1 mm. The second and third sets consisted of the samples with the same thickness of 1.25 mm. After irradiation the samples of the second set were thinned from the front surface, the samples of the third set were thinned from the back surface to different thickness up to 0.6 mm. The stored energy was measured for each sample.

The predicted dose profile after 0.63 C/cm^2 irradiation with 0.5 MeV electrons is shown in Fig. 11a. The average absorbed dose $D_{av}(t)$ in the sample of given thickness t is:

$$D_{av}(t) = \frac{n}{t\rho}\int_0^t Q(x')dx' \cdot \tag{1.3.10}$$

Here n is the electron fluence and ρ is the density of the sample. Dependence $D_{av}(t)$ for the first set of samples is shown in Fig.11b. The absorbed dose for the sample of initial thickness t_0 and thinned from the front surface up to final thickness t from the second set is given by

$$D^b_{av}(t) = \frac{n}{t\rho}\int_{t_0-t}^{t_0} Q(x')dx' \tag{1.3.11}$$

and it is shown in Fig.11b. Then we have ultimately

$$D_{av}(t_0 - t) = [D^b_{av}(t_0)t_0 - D^b_{av}(t)t]/(t_0 - t) \tag{1.3.12}$$

Using (1.3.12) it is simple to recalculate $D^b{}_{av}(t)$ data to obtain the $D_{av}(t)$ dependence. In Fig. 12 the selected measured data are plotted together with data, recalculated using equation (3.1.12). The comparison of the experimental data with the calculated profile has shown that the proposed method can serve as a baseline for an evaluation of the absorbed dose in alkali halides under electron irradiation of MeV-energy.

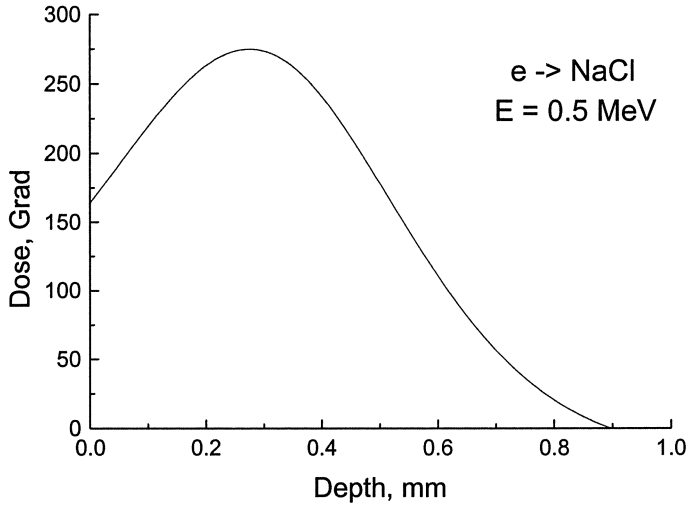

Fig.11a. Calculated energy deposition profile in NaCl after 0.63 C/cm^2 irradiation with 0.5 MeV electrons.

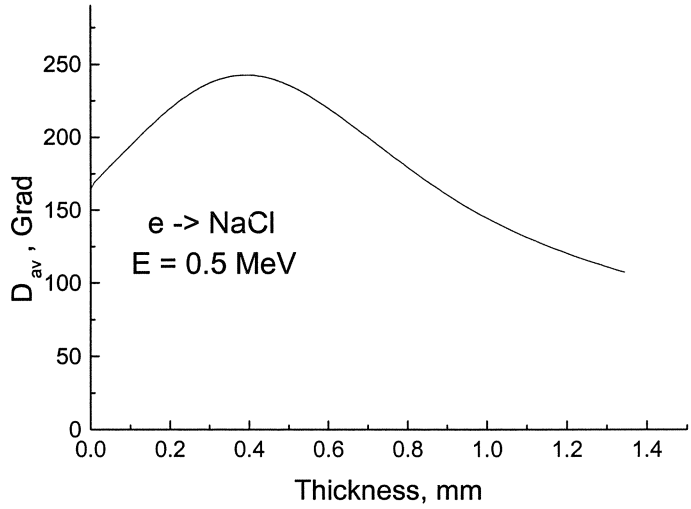

Fig.11b. The average absorbed dose vs. the sample thickness.

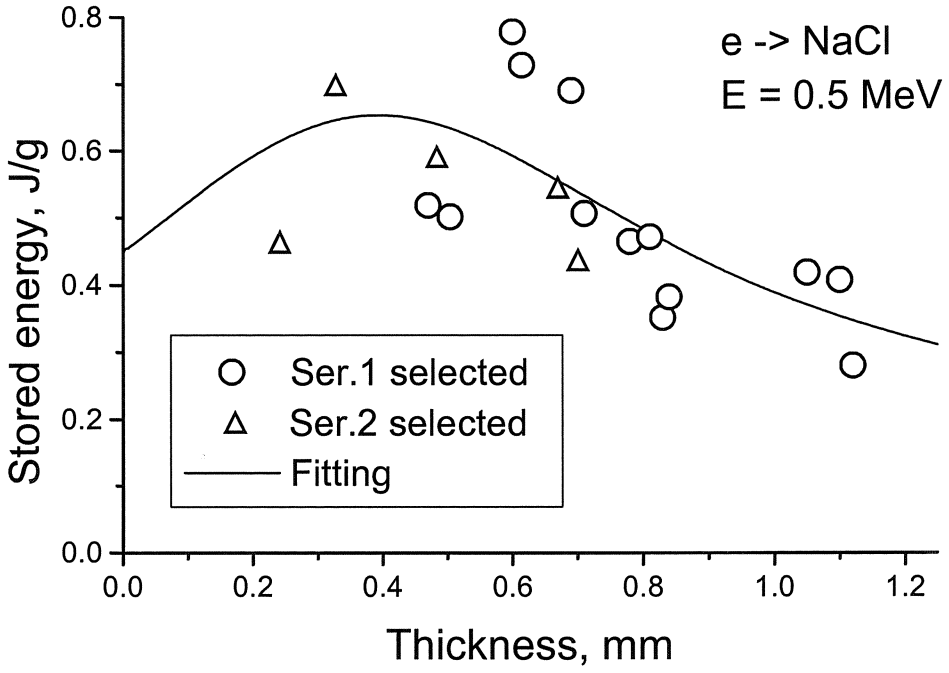

Fig.12. The average absorbed dose vs. the sample thickness.

3.1.10 Irradiation runs

In the present project we have carried out four irradiation runs to different dose levels in the temperature range from 40 to 150 ^{0}C. As a result, a total number of 1335 samples have been irradiated to reach the following goals: testing irradiation facility, dosimetry control and irradiation of NaCl samples to carry out the planned experimental investigations.

Below is the list of irradiation runs that shows the numbers of samples irradiated in each run:

NaCl:Impurities	**Nominal Concentration, mole %**	**Dose, Grad (± 8%)**			
		30	**100**	**200**	**300**
K	0.1	45	25	15	15
K	1	45	-	15	15
Li	0.5	45	-	15	15
F	0.1	45	-	15	15
B	0.1	45	-	15	15
Br	0.1	45	-	15	15
Br	0.015	45	-	15	15
Ba	0.05	45	-	15	15
KBF4	0.03	45	25	15	15
Pure		45	-	15	15
Dutch Rock Salt		45	25	15	15
German Rock Salt (Asse)		45	-	15	15

3.2 Goal 1: Investigations of voids

The methodology of the investigations of voids by means of scanning electron microscopy (SEM) will be explained first. A freshly cleaved surface (this is a (100) plane) of an irradiated sample is placed in a vacuum system in order to apply a very thin layer of metallic palladium by means of evaporation. This treatment is necessary in order to avoid negative charging of the insulating NaCl samples during exposure to the moderately energetic electron beam of the electron microscope. The transfer to the vacuum system should be as fast as possible because the water vapor in the ambient atmosphere reacts with the surface of the cleaved sample, and this may perturb the SEM pictures considerably.

After this treatment the sample is transferred to the electron microscope system and suitable areas at the surface of the sample are found and investigated. As grown crystals and natural crystals, which were not irradiated, did not show any sign of void formation. The surfaces of these samples were completely flat. Only after exposure to high doses of irradiation we have observed voids.

In order to obtain results, which are representative for the sample, we have always investigated several different areas of the sample surface. In some cases this is useful, because the formation of voids often depends on the stress-state in a particular area of the sample. In addition, some samples like Br-doped NaCl contain only a few voids and it is necessary to scan a relatively large area to find them. We note that in the latter situation a SEM picture does not represent the average picture for this sample. SEM experiments including the analysis are time consuming. For each sample several photographs were made. The scanned pictures of these photographs have been investigated by means of a computer program, which enables us to recognize and characterize the voids. After this process of recognition and characterization, the characteristic properties of the voids are analyzed in terms of histograms by our SCAN-PRO software. The accuracy of the method is estimated to be less than 1%. This figure does not include the statistical effects, which can be particularly important in case of very low void number densities (i.e. in case of NaCl:Br). We have obtained values for the void sizes, we were able to establish the shape of the individual voids by comparing the length and width and finally we have calculated on the basis of this information the total void volume in the sample. In figures 13 and 14 we present two examples of SEM pictures, which have been analyzed by means of the program SCAN-PRO. The void-number, the contours of the voids and the long and short axes of the voids are indicated. Statistical software was used to analyze the results, which will be presented in this chapter.

In this project we have obtained SEM pictures of at least 150 different heavily irradiated NaCl samples and for each sample different areas of the surface have been investigated in order to be sure that the results obtained for the samples was representative. As mentioned above, for some of the samples the statistics is poor, but it is difficult to improve the situation, because this applies to samples with only a few (small) voids per picture or even no void at all. We note however that the characteristic properties presented in the void-pictures of this report are representative for the samples under consideration. I.e. small approximately equi-axial voids are observed in most of the samples at low doses. The voids grow with increasing dose and ultimately they are transformed into what we call "elongated voids". This applies to almost all types of investigated samples, the exceptions being pure NaCl and NaCl:Br. Although the results on the voids have been presented rather quantitatively, they should be treated qualitatively. This includes the graphical presentations given in this chapter. We emphasize that this limitation does not interfere with the important, final conclusions of this project presented at the end of this report.

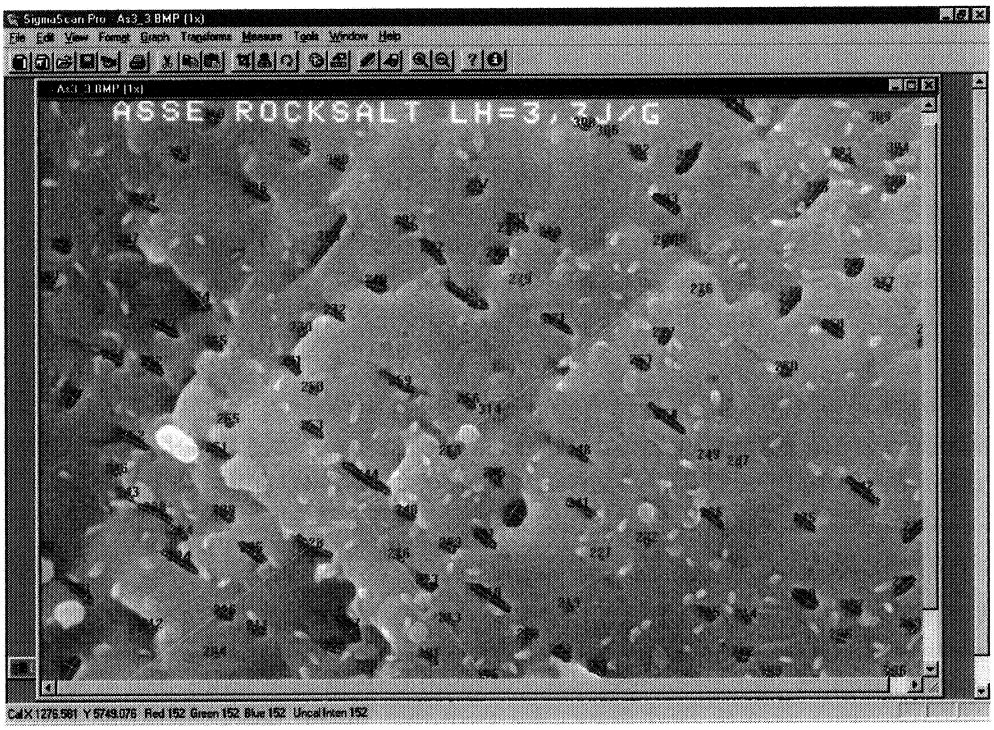

Figure 13. Voids in heavily irradiated natural rock salt from the Asse mine in Germany. The latent heat of melting of metallic Na is 3.3 J/g, which implies that about 7.5% of the Na-ions in the NaCl lattice were transformed into Na-atoms. A significant fraction of the voids is elongated. The contours of the voids have been indicated together with the void numbers.

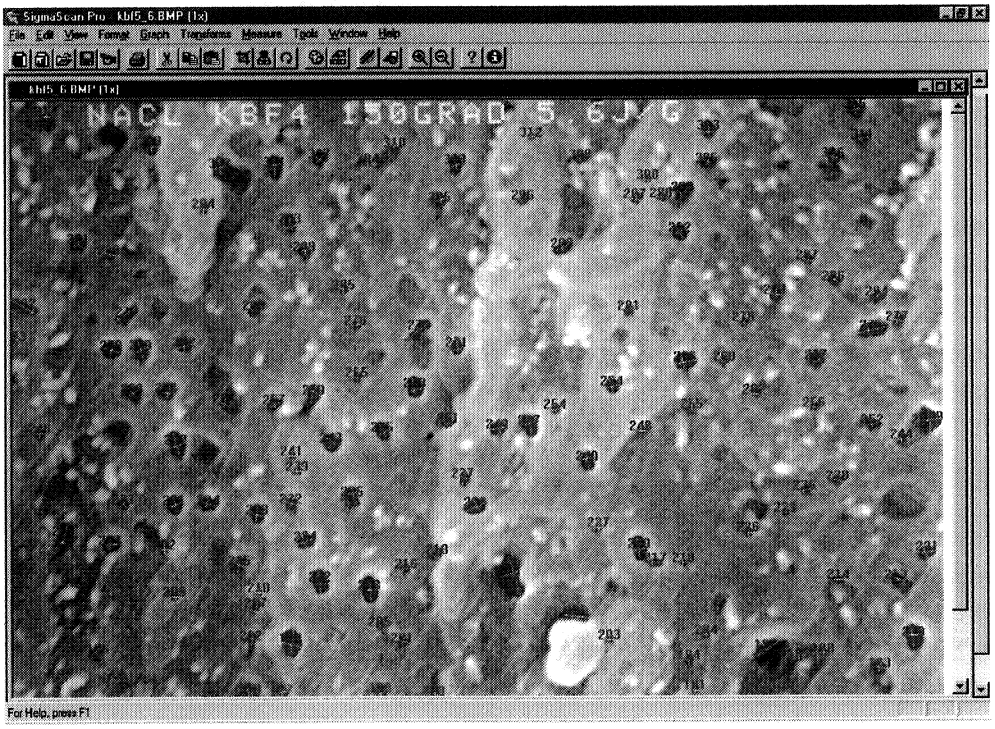

Figure 14. Voids in heavily irradiated NaCl doped with KBF_4. The amount of metallic Na in this sample is about 12%. The voids in this sample are more or less round and not elongated, as natural rock salt from Asse shown in Fig. 13.

From the point of view of statistics we note that usually the number of voids per experiment is several hundred in some cases almost 500, but in some cases we are not able to reach these numbers, because the number of voids is just too small. In these samples void formation was very slow. In samples with extensive void formation this problem does not occur and for these samples we can draw sound conclusions. For instance, in NaCl:K, NaCl:KBF_4 and natural rock salt, samples in which voids develop very easily, we have carried out investigations on groups with sufficiently large numbers of voids. For samples with small numbers of voids the characteristic properties (such as the size and the ratio of the length and width) of the voids shown in the SEM pictures are representative for the samples under consideration. Of course the number densities and the total void volumes depend on the specific area under investigation. This remark applies particularly to NaCl:Br.

3.2.1 Experimental observations

Several samples, which had been irradiated in earlier irradiation runs, have been studied by means of SEM. These results will be used as comparison with results, obtained after irradiation experiments with the modified irradiation facility. As mentioned above, it is important to find the eventual relationships between the numbers, sizes and shapes of the voids and the presence of impurities. Among the impurities investigated are lithium, fluoride, barium, potassium, KBF_4 and bromide. In addition, several, heavily irradiated, natural rock salt samples have been investigated with SEM. The irradiation dose of the samples was between 0 and 300 Grad. We note that in several cases only a limited number of doses were available, because the samples were not present or they had been used already for other purposes, e.g. explosion or annealing experiments.

Figs. 15-24 show SEM micrographs and void size histograms in nominally pure NaCl (impurity content less than 10 ppm) and doped with lithium, barium, fluoride and KBF_4 samples and in the Asse and Dutch rock salt, all of them being irradiated up to a maximum dose 300 Grad[1] at temperatures ranging from 60 ^{0}C to 130 ^{0}C. It can be seen that sizes, shapes and number densities of voids as well as amounts of stored energy are different for different materials. There are also some differences between the samples of the same type due to different irradiation temperatures as shown for fluoride doped and Asse rock salt (figs. 18 and 19) and especially for KBF_4 samples (Figs. 20 and 21) and Dutch rock salt (Figs. 22-24).

Figs. 25- 31 show the microstructural evolution with increasing irradiation dose at 100 ^{0}C in samples doped with bromide and potassium, which represent the opposite effects of impurities on the colloid and void evolution. In the former case voids are few and relatively small, and the shape of the voids is more or less round. In the latter case voids are more numerous and strongly elongated along the <100> crystallographic directions. The volume fraction of colloids in potassium-doped samples is higher than those in bromide-doped samples by a factor of 5, while the volume fraction of voids is higher by 3 orders of magnitude! This huge difference is, first of all, due to the very large differences in void size (fig. 31).

It should be noted that the volume fraction of the colloids is proportional to the latent heat of melting (LHM) of metallic *Na*, which was measured and shown in the figures in J/g. A latent heat value of 1 J/g is equivalent to about 2% of the colloid volume fraction (see Table 3). The

1 Note that a total dose 150 Grad shown in the micrographs does not take into account the beam reflection from the sample holders. In this project we have developed a new code for the dose rate calculation (sec. 3.1.9), which gives a factor of 2 increase of the actual dose rate.

void volume fraction is equal to the surface fraction, which was actually measured and shown in the figures, as well as the void surface density. The void volume density, $N_V(vol)$, was deduced from the measured density per unit surface, $N_V(surf)$, and the mean size, according to the following simple relation: $N_V(vol) \approx N_V(surf)/2R_V$, where $2R_V$ is the mean void size.

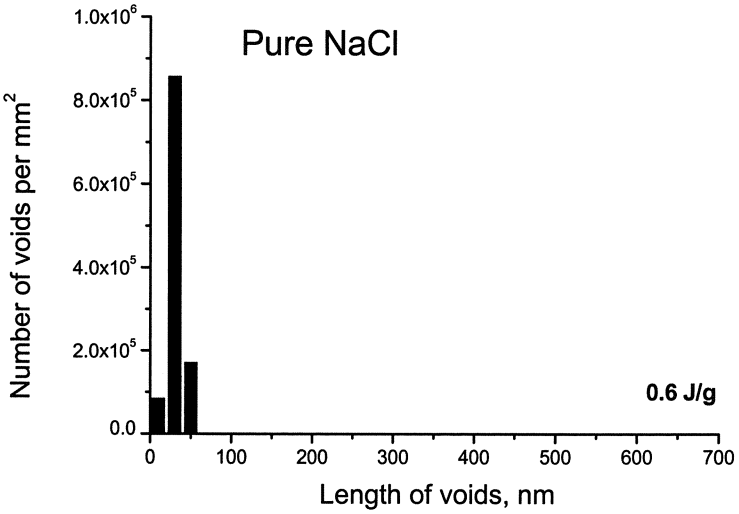

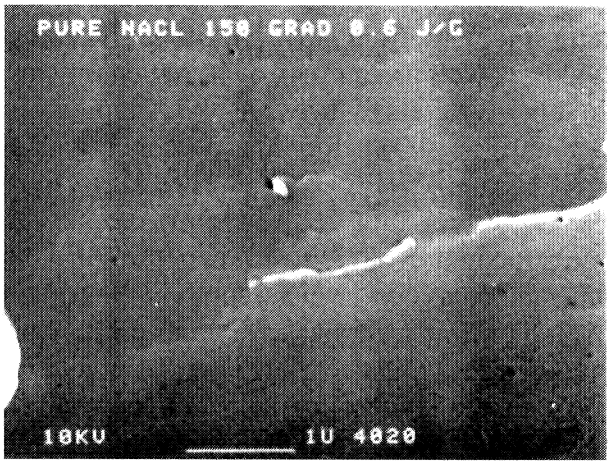

Figure 15. SEM micrograph and the void size histogram in electron irradiated pure NaCl.

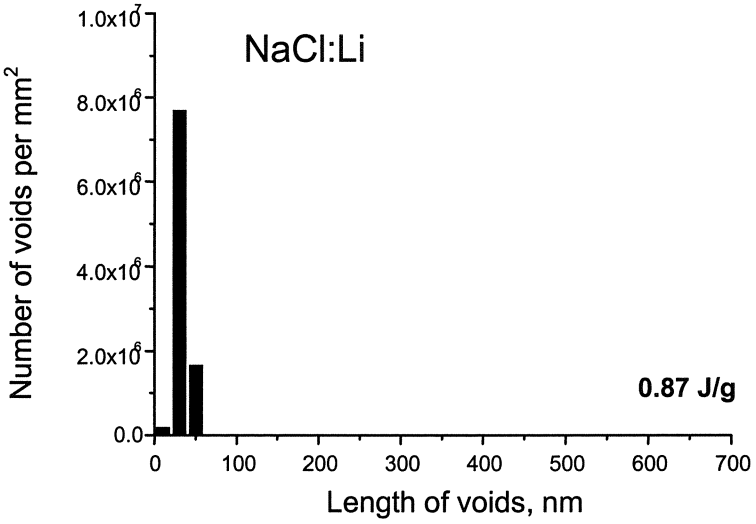

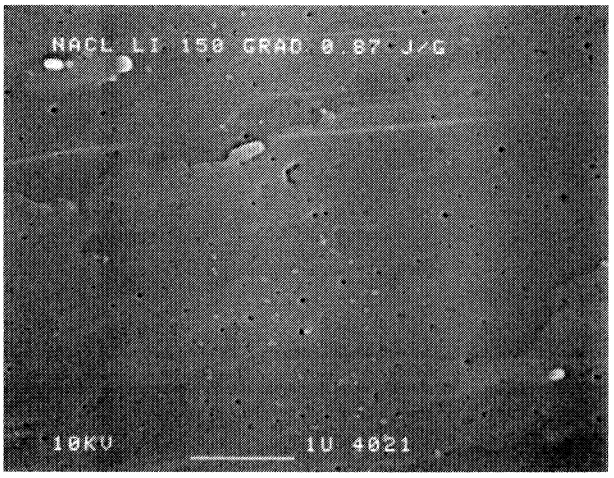

Figure 16. SEM micrograph and the void size histogram in electron irradiated NaCl doped with 0.5% Li.

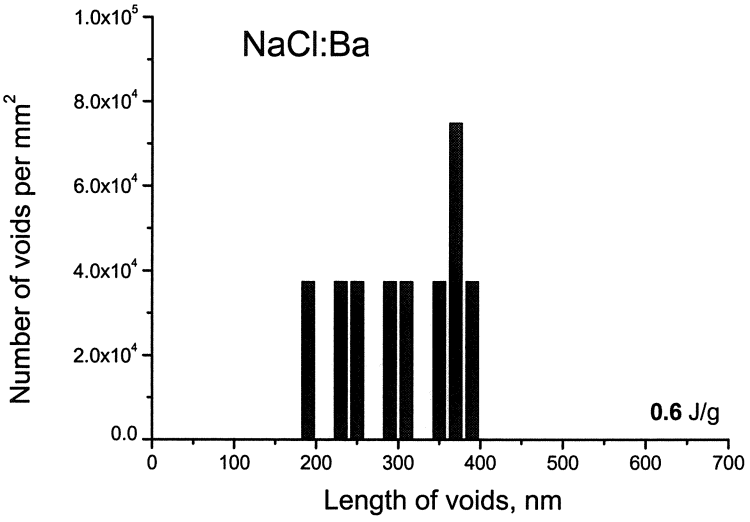

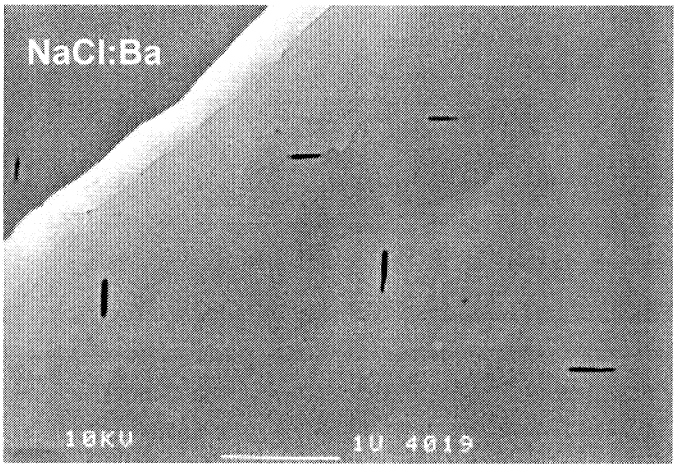

Figure 17. SEM micrograph and the void size histogram in electron irradiated NaCl doped with 0.05% Ba.

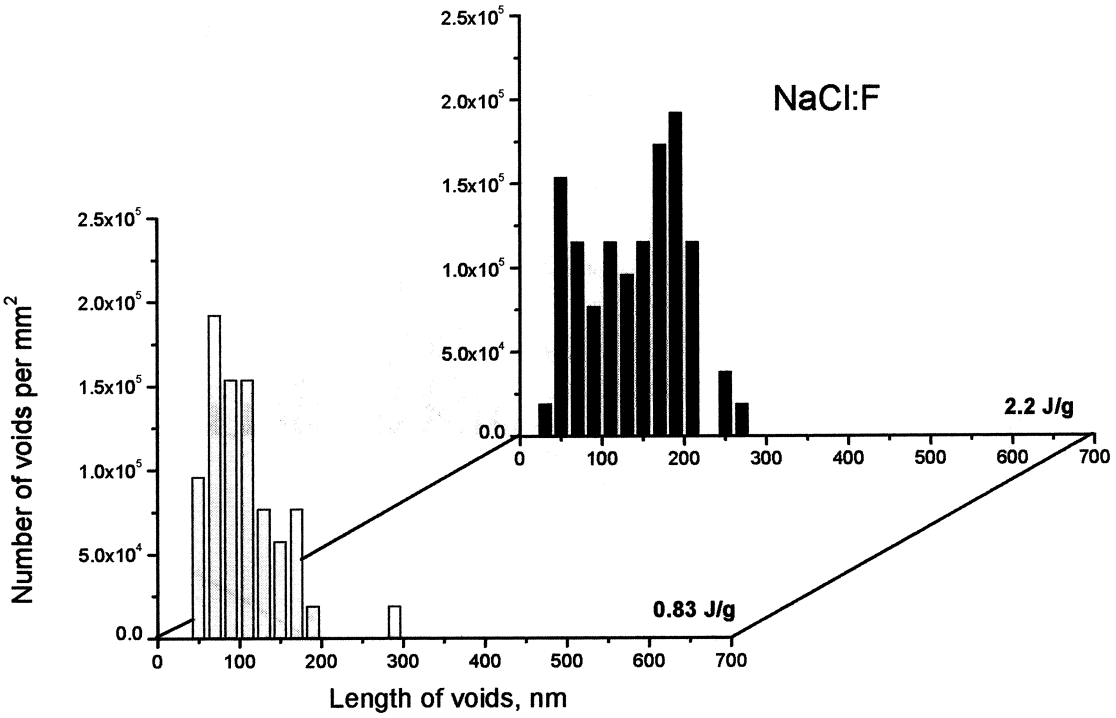

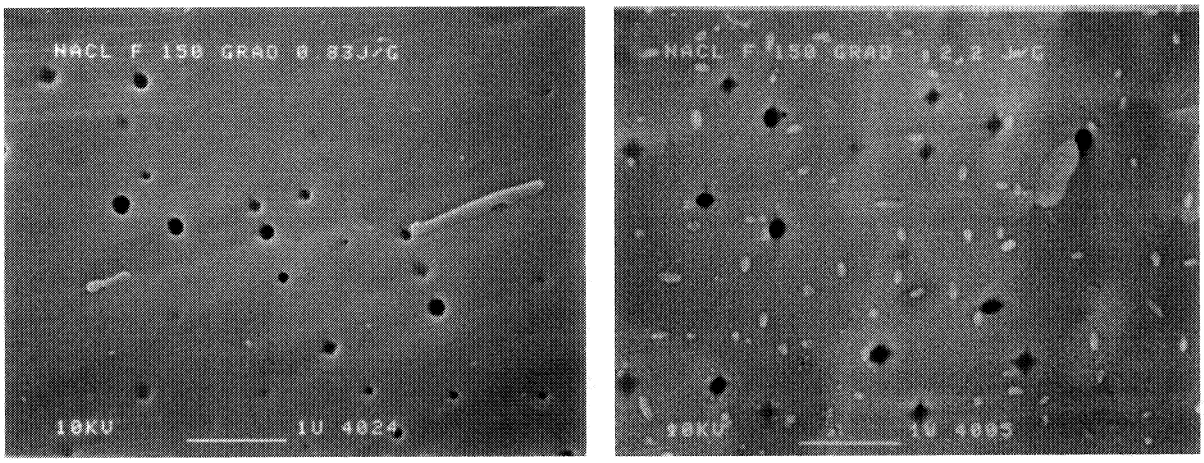

Figure 18. SEM micrograph and the void size histogram in electron irradiated NaCl doped with 0.1% F

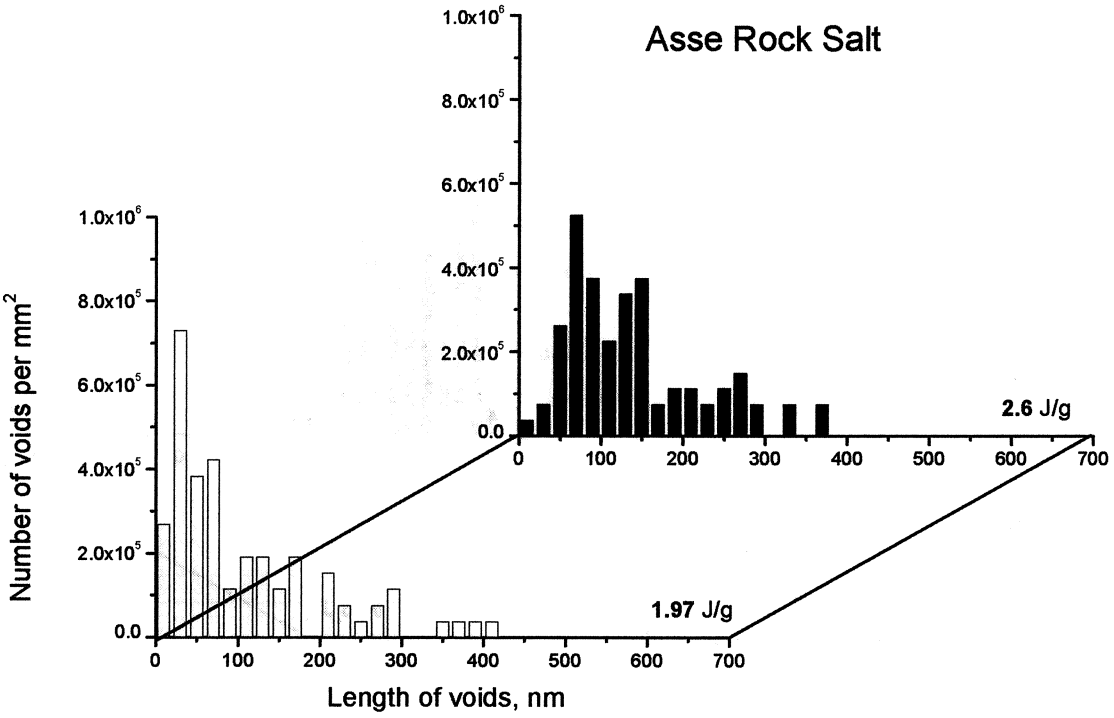

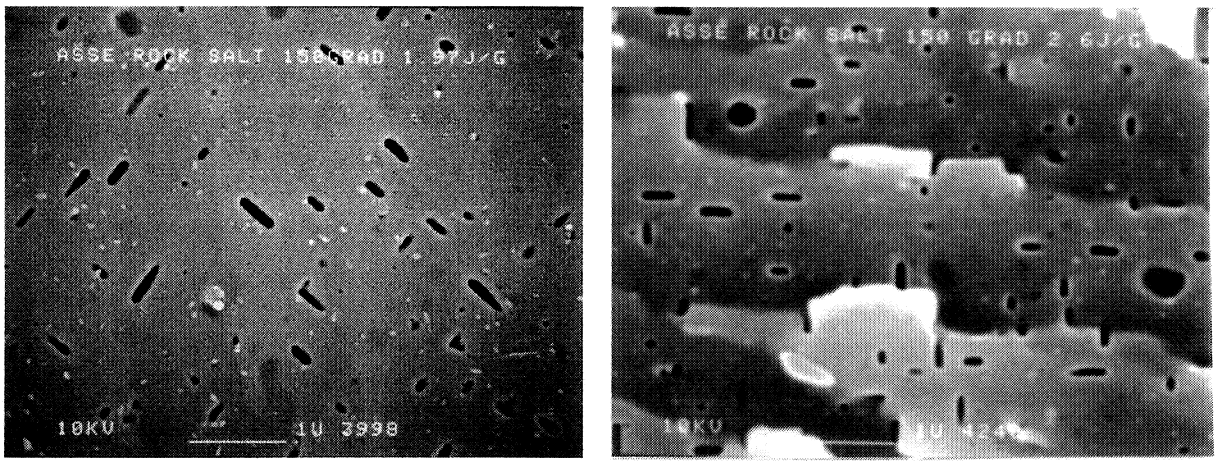

Figure 19. SEM micrograph and the void size histogram in electron irradiated Asse Rock Salt.

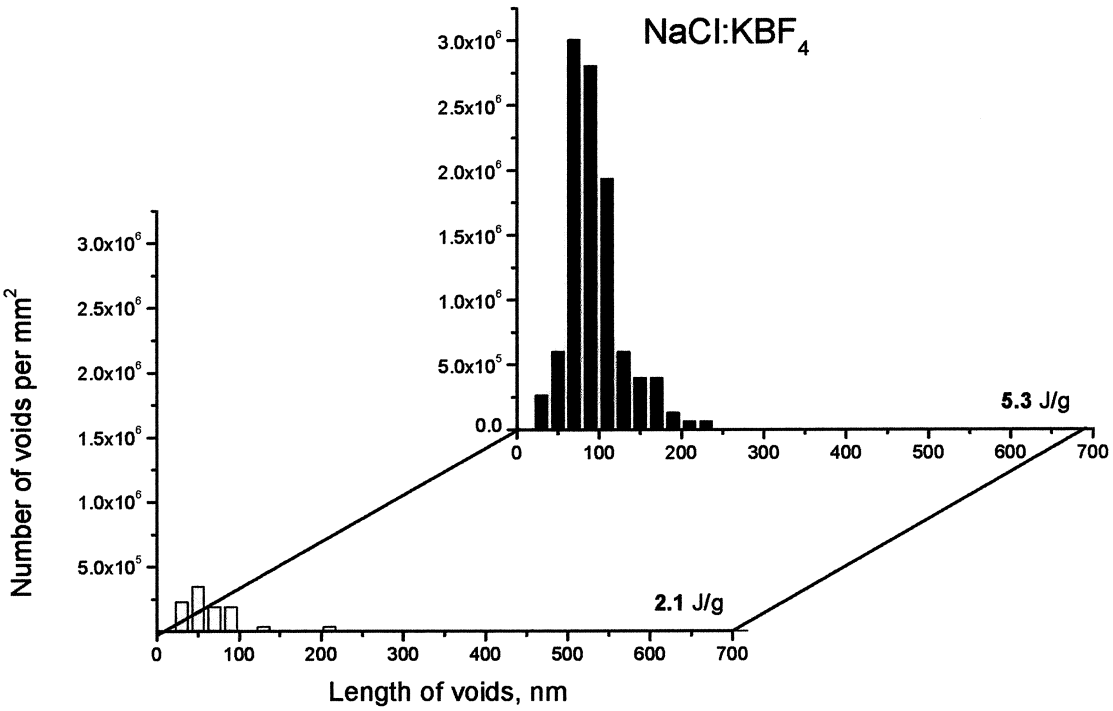

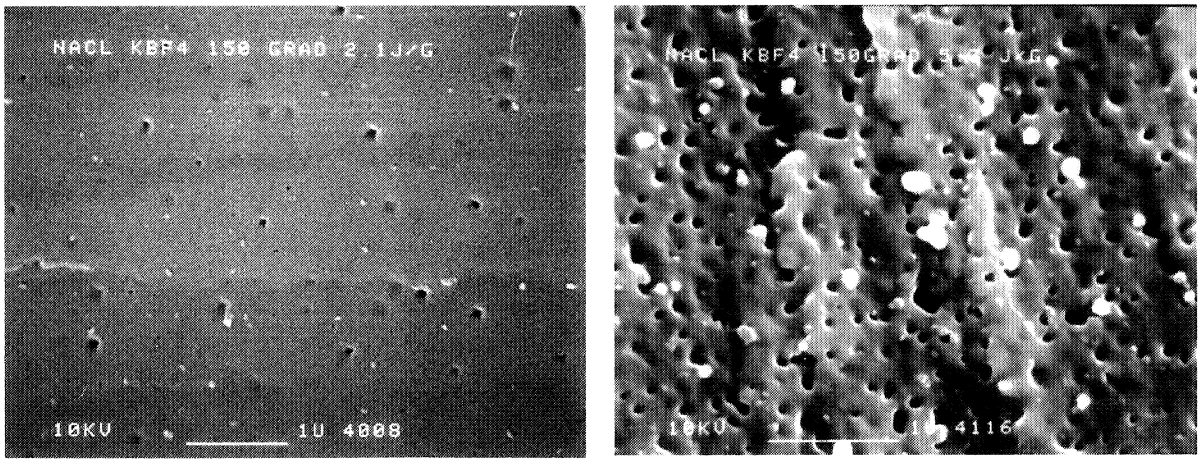

Figure 20. SEM micrograph and the void size histogram in electron irradiated NaCl doped with 0.03% KBF_4.

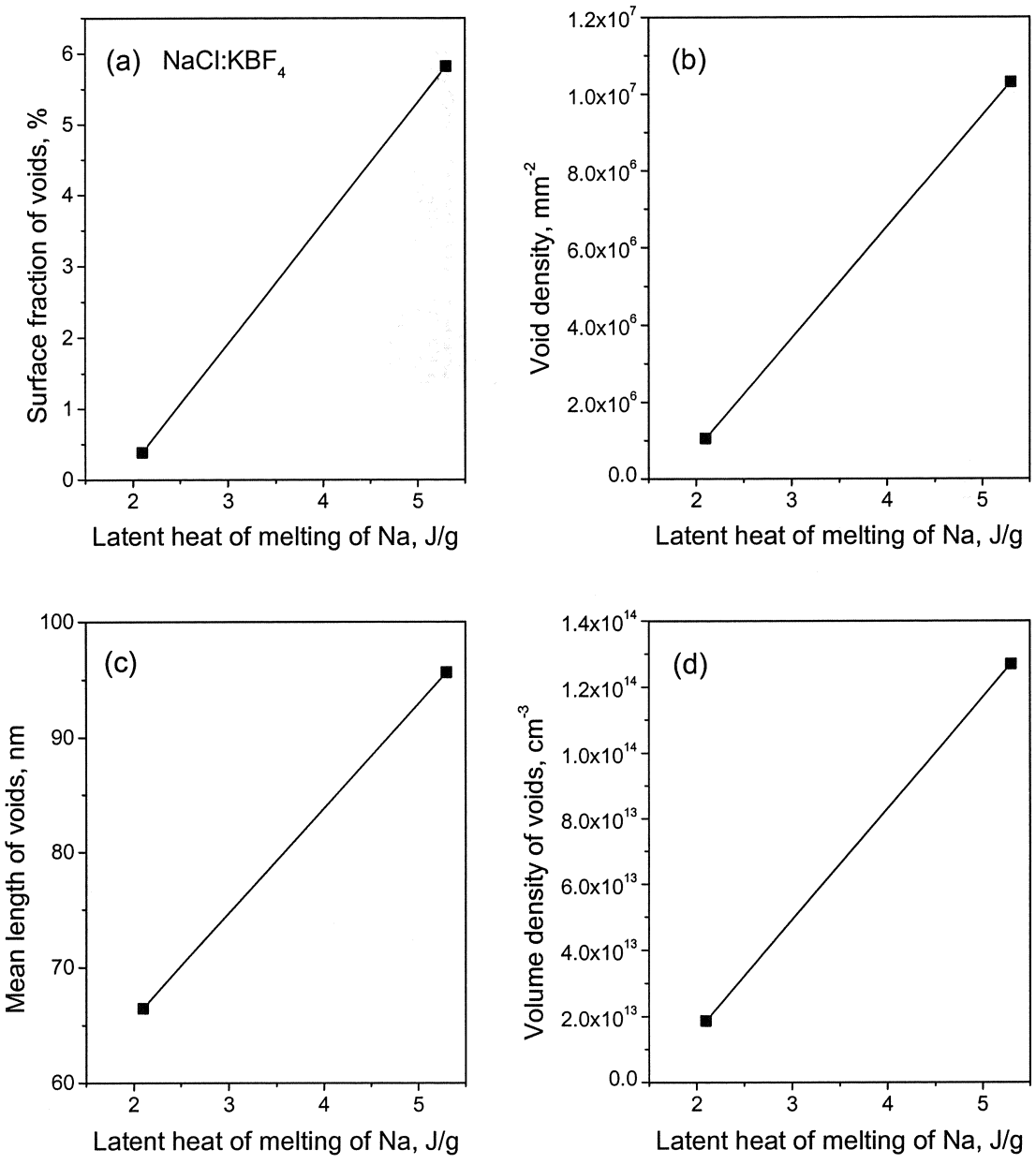

Figure 22. Void mean parameters in electron irradiated NaCl doped with 0.03% KBF_4.

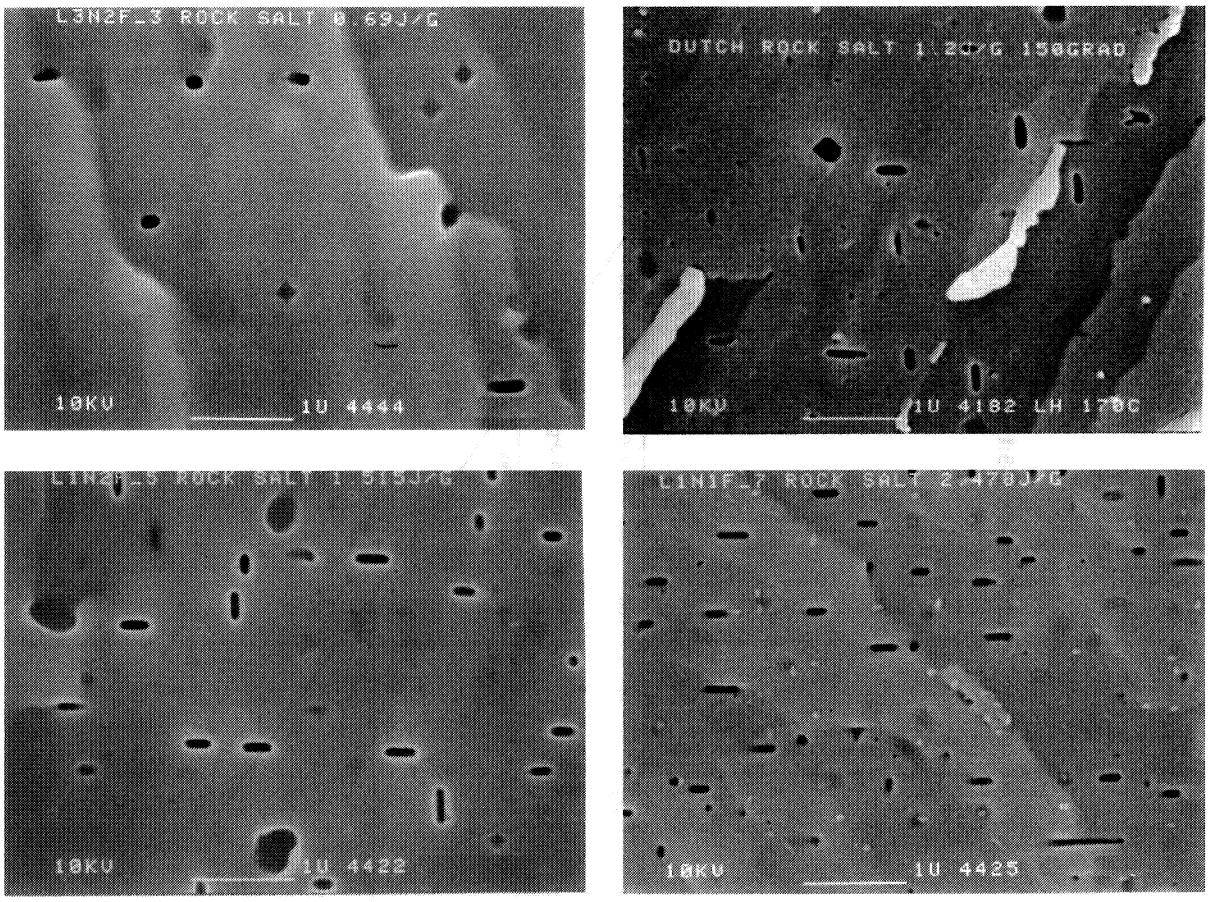

Dutch Rock Salt LHM, J/g	Mean Length,nm	Max Length, nm	Surface fraction, %	Void Density, mm-2	Volume Density, cm^{-3}
0.69	230	242	1.06	3.86E+05	1.98E+12
1.2	135	299	1.20	1.75E+06	1.52E+13
1.51	132	321	1.07	1.59E+06	1.41E+13
2.47	157	654	1.13	1.61E+06	1.21E+13

Figure 22. SEM micrograph and void mean parameters in electron irradiated Dutch Rock Salt.

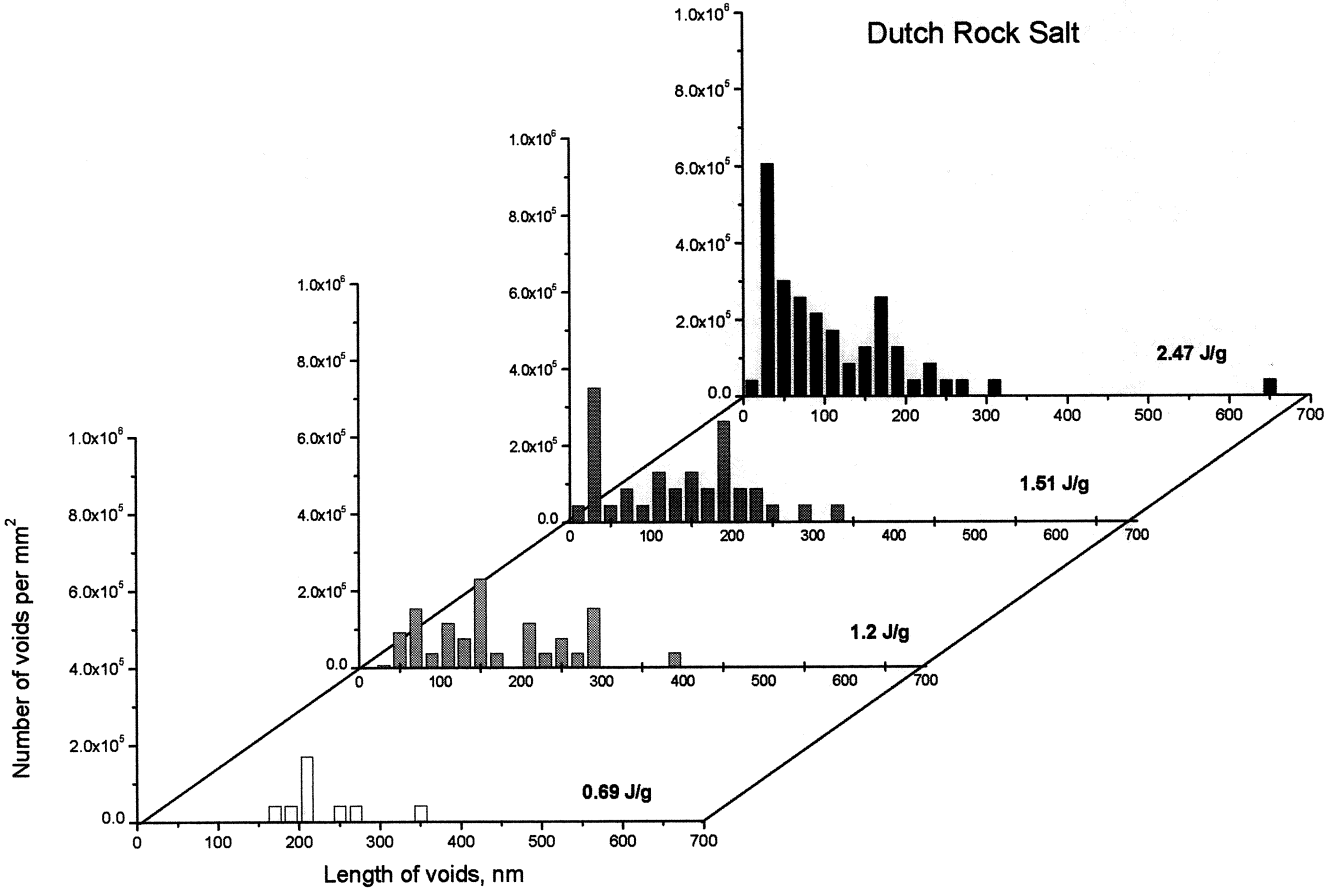

Figure 23. Void size histogram in electron irradiated Dutch Rock Salt.

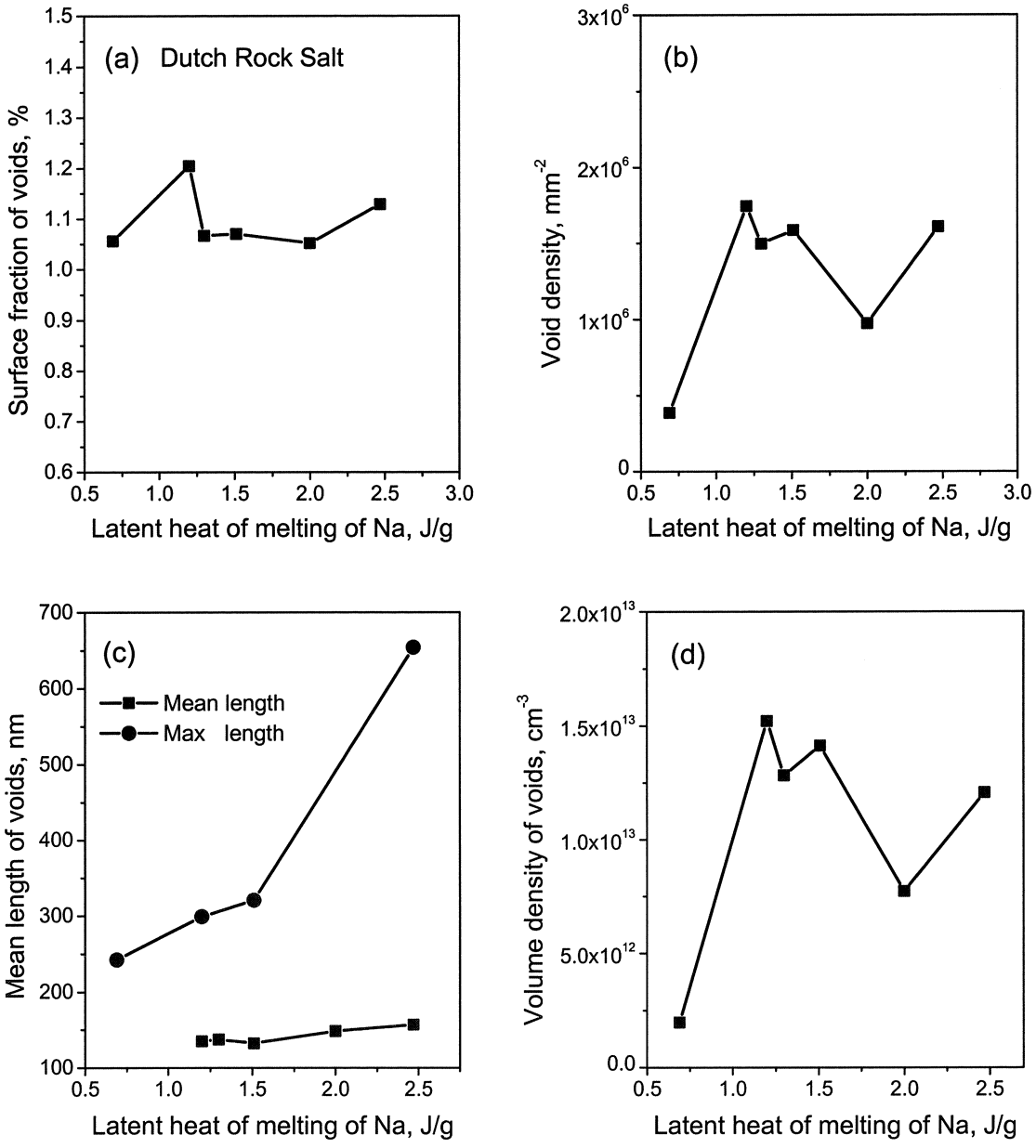

Figure 24. Void mean parameters in electron irradiated Dutch Rock Salt.

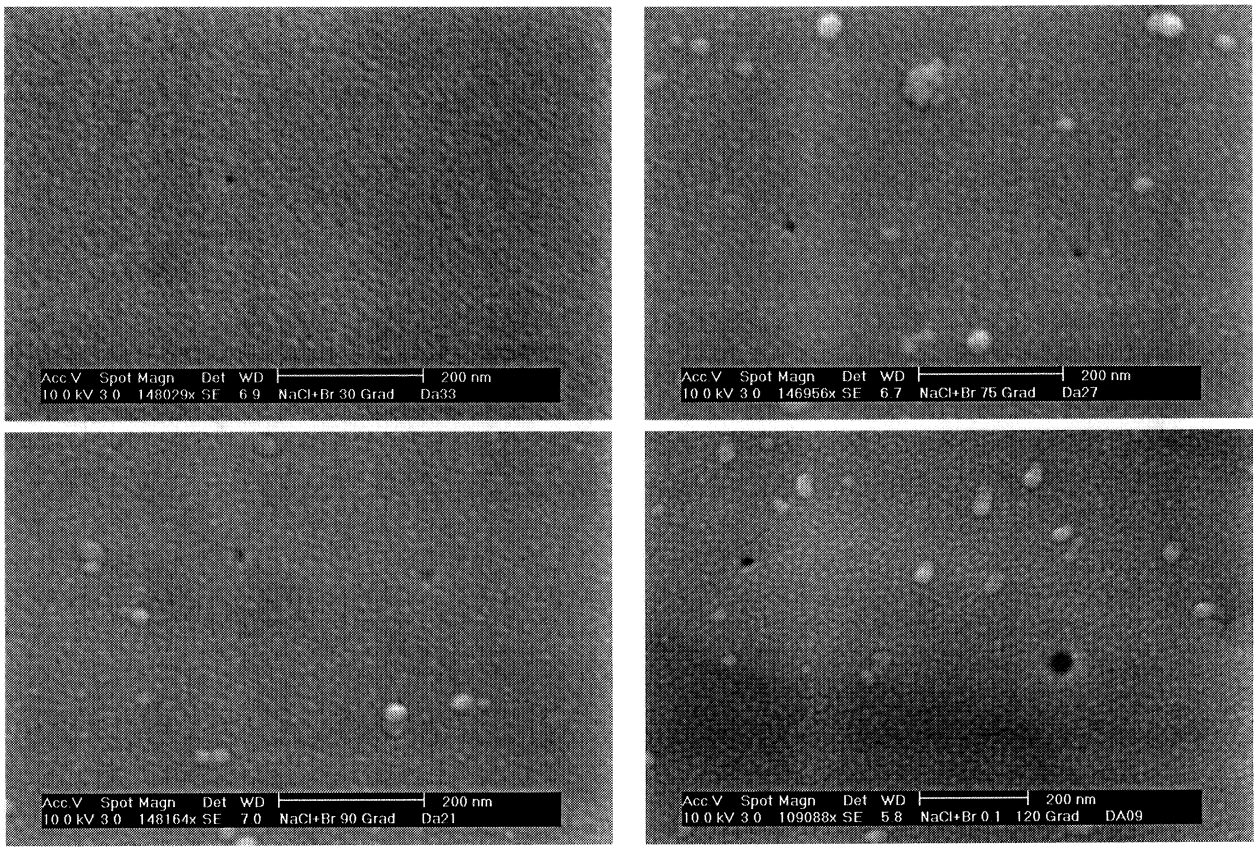

NaCl:Br					
Dose	Mean length, nm	Max length, nm	Surface fraction, %	Void density, mm-2	Volume density, cm-3
60	8.91	8.91	1.48E-04	2.08E+03	2.34E+11
150	11.18	11.31	5.91E-04	3.08E+03	2.72E+11
180	16.52	16.69	8.30E-04	4.60E+03	2.79E+11
240	32.78	37.21	1.20E-03	8.82E+03	2.92E+11

Figure 25. SEM micrograph and void mean parameters in electron irradiated NaCl doped with 0.1% Br.

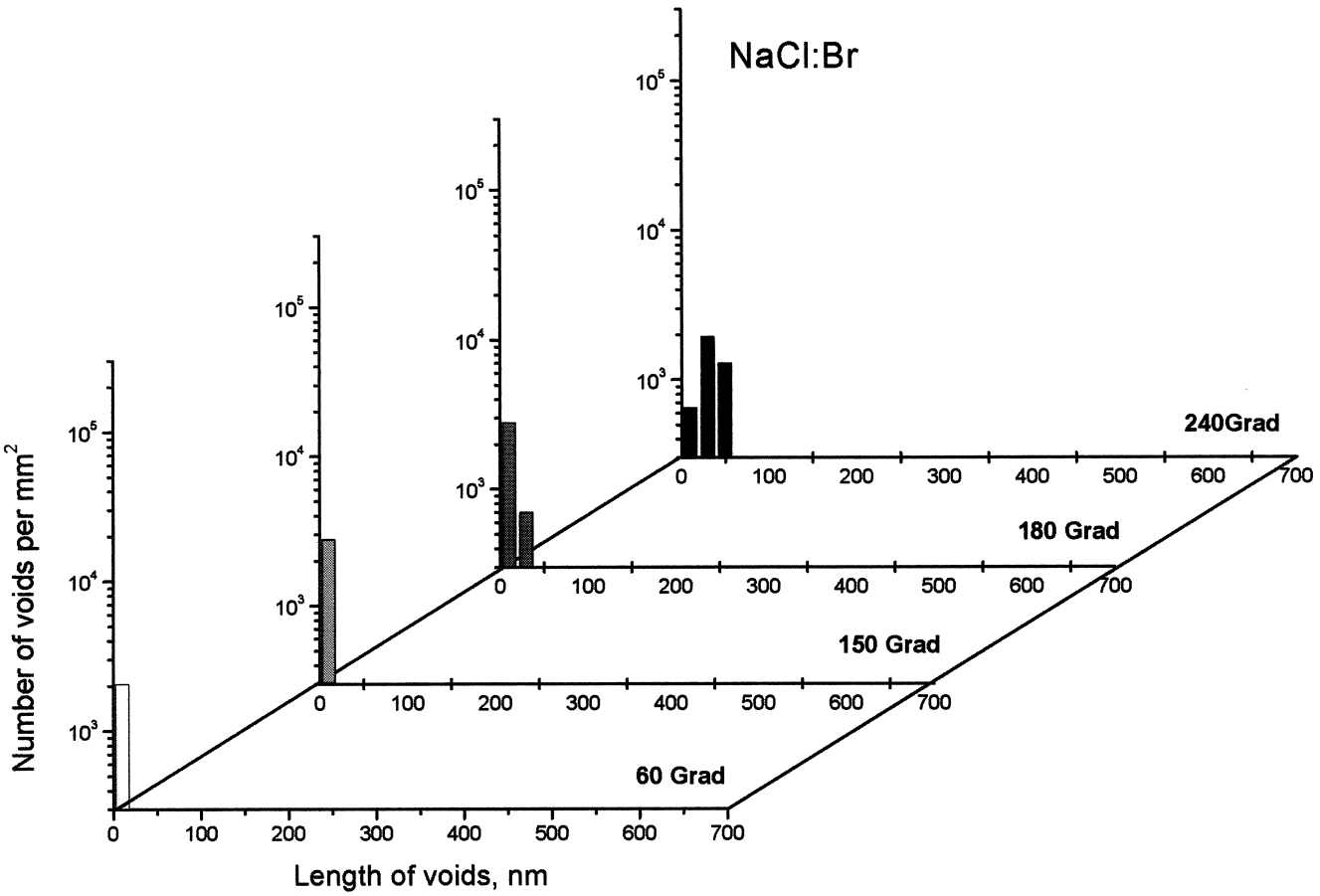

Figure 26. Void size histogram in electron irradiated NaCl doped with 0.1% Br.

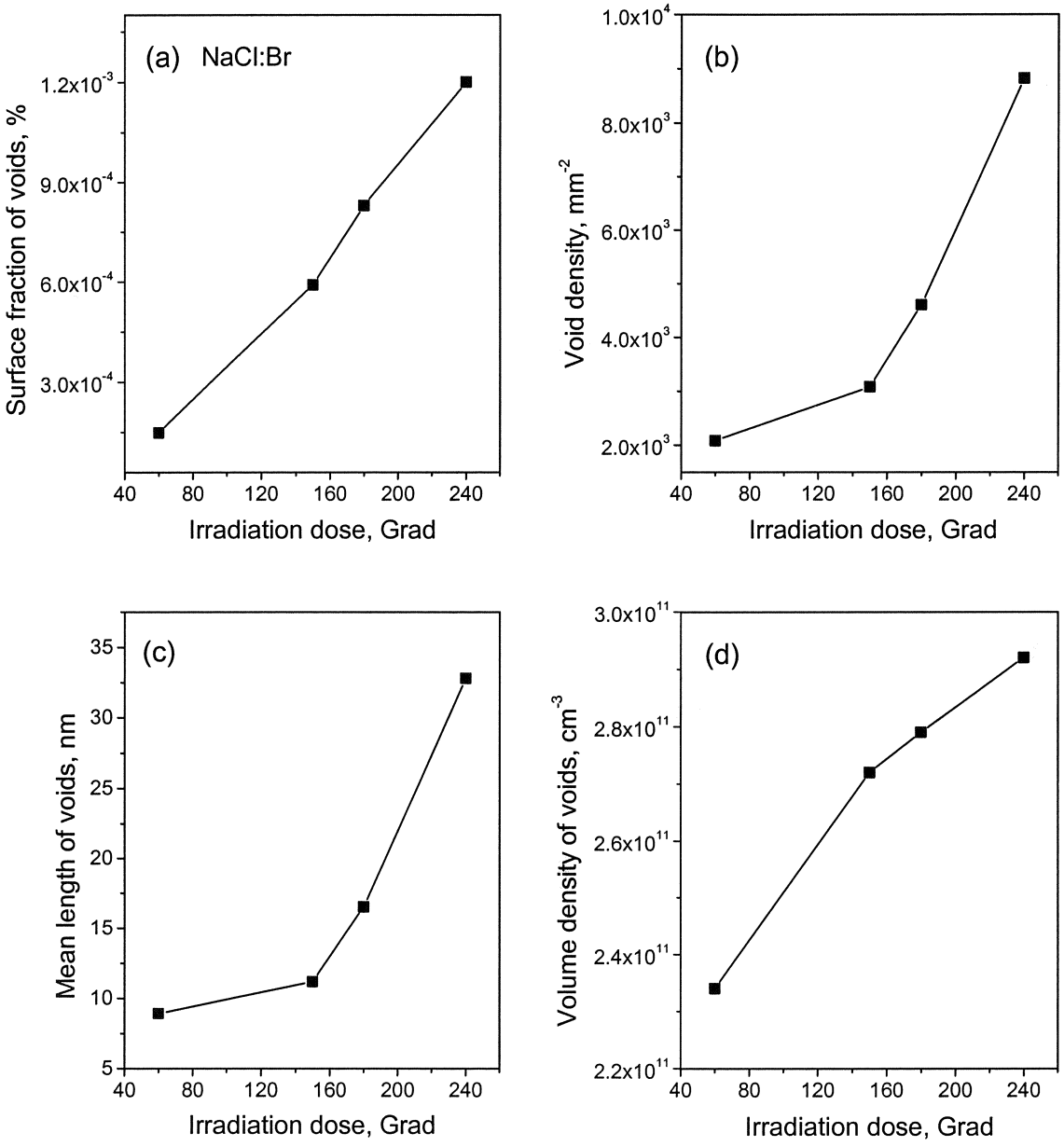

Figure 27. Void mean parameters in electron irradiated NaCl doped with 0.1% Br.

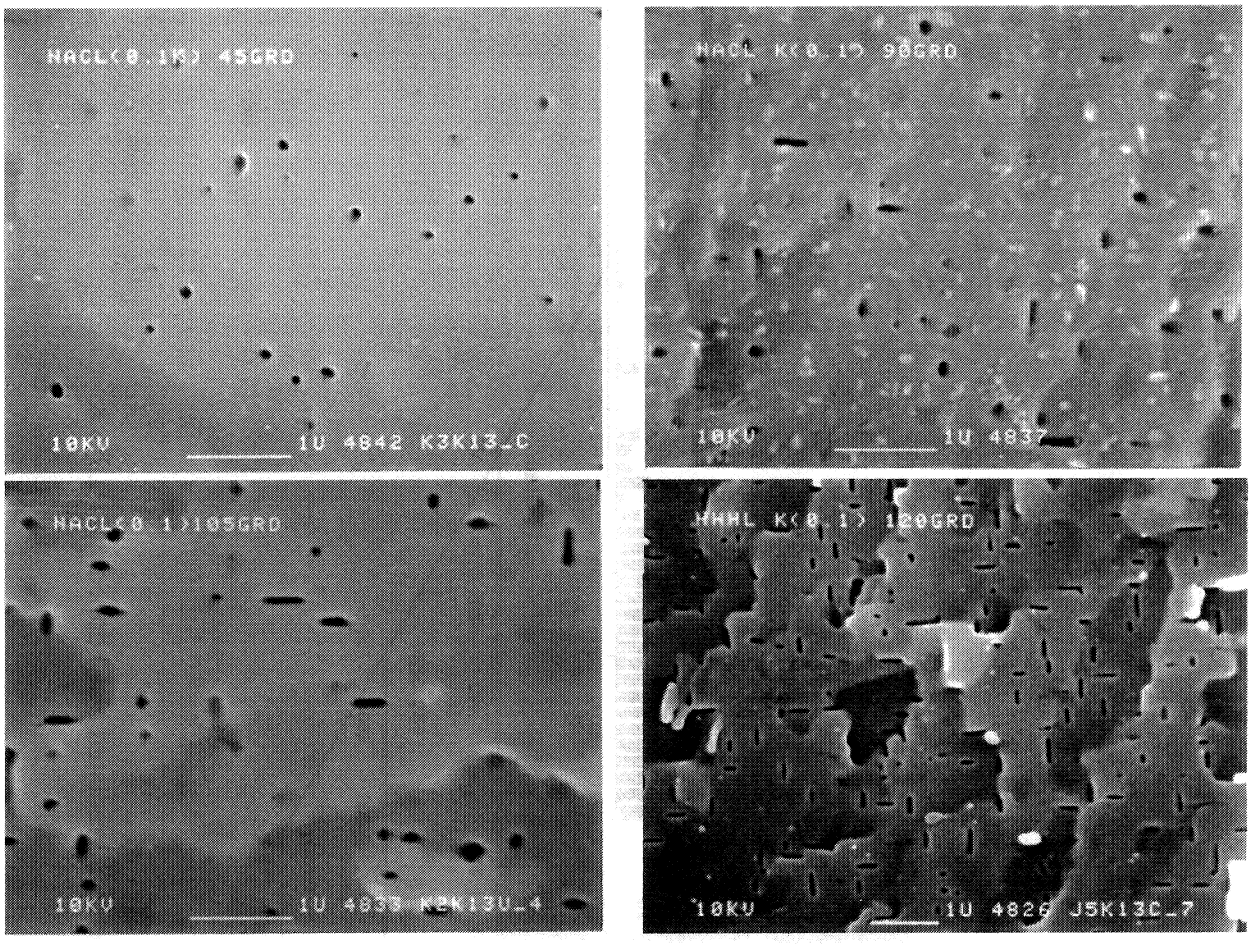

NaCl:K Dose, Grad	LHM, J/g	Mean Length,nm	Max Length, nm	Surface fraction, %	Void Density, mm^{-2}	Volume Density, cm^{-3}
60	0.84	114	138	0.15	1.51E+05	1.56E+12
90	1.05	102	287	0.49	7.10E+05	8.19E+12
180	2.10	126	334	0.93	1.15E+06	1.08E+13
210	2.31	144	551	1.16	1.14E+06	9.37E+12
240	2.81	169	669	2.26	2.85E+06	1.98E+13

Figure 28. SEM micrograph and void mean parameters in electron irradiated NaCl doped with 0.1% K.

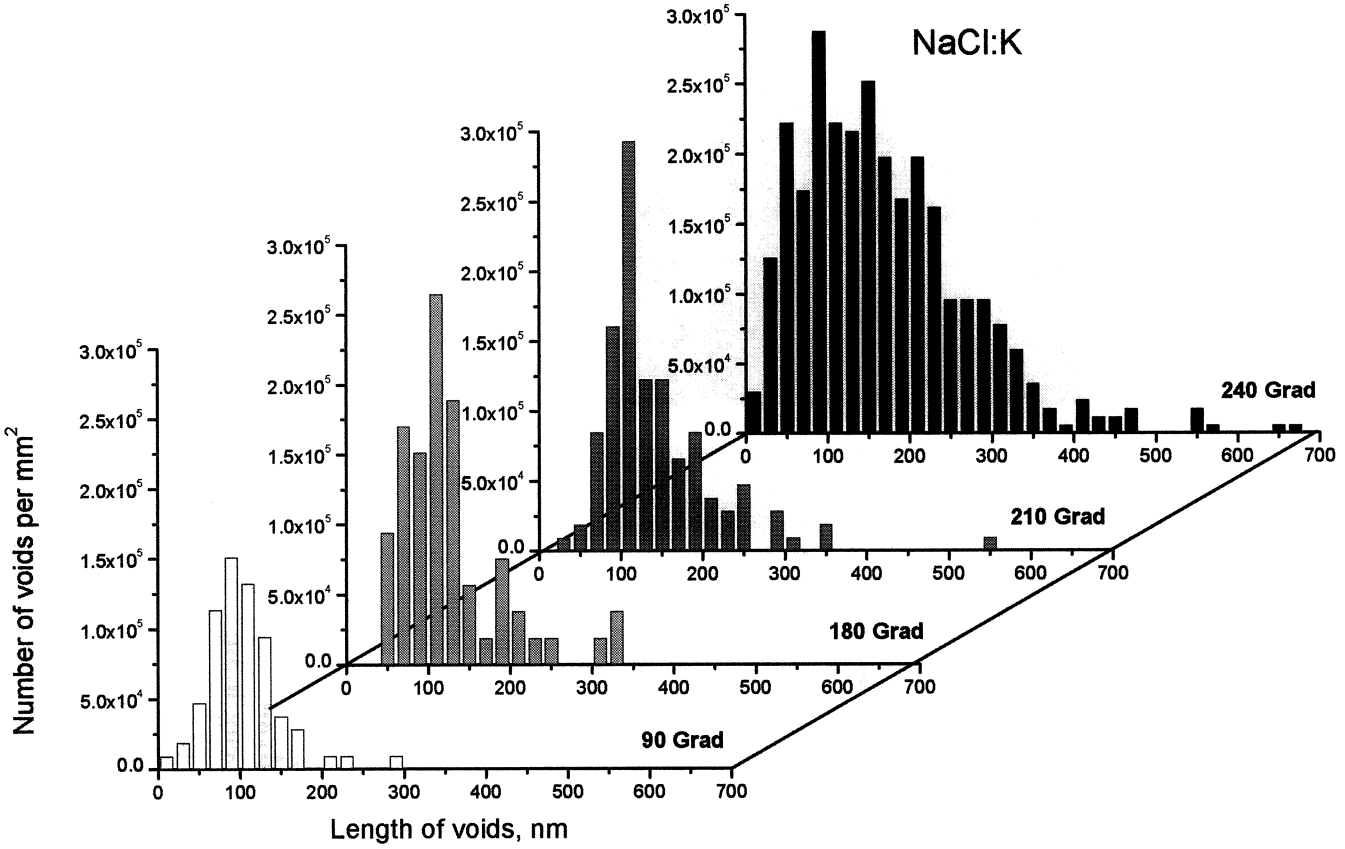

Figure 29. Void size histogram in electron irradiated NaCl doped with 0.1% K.

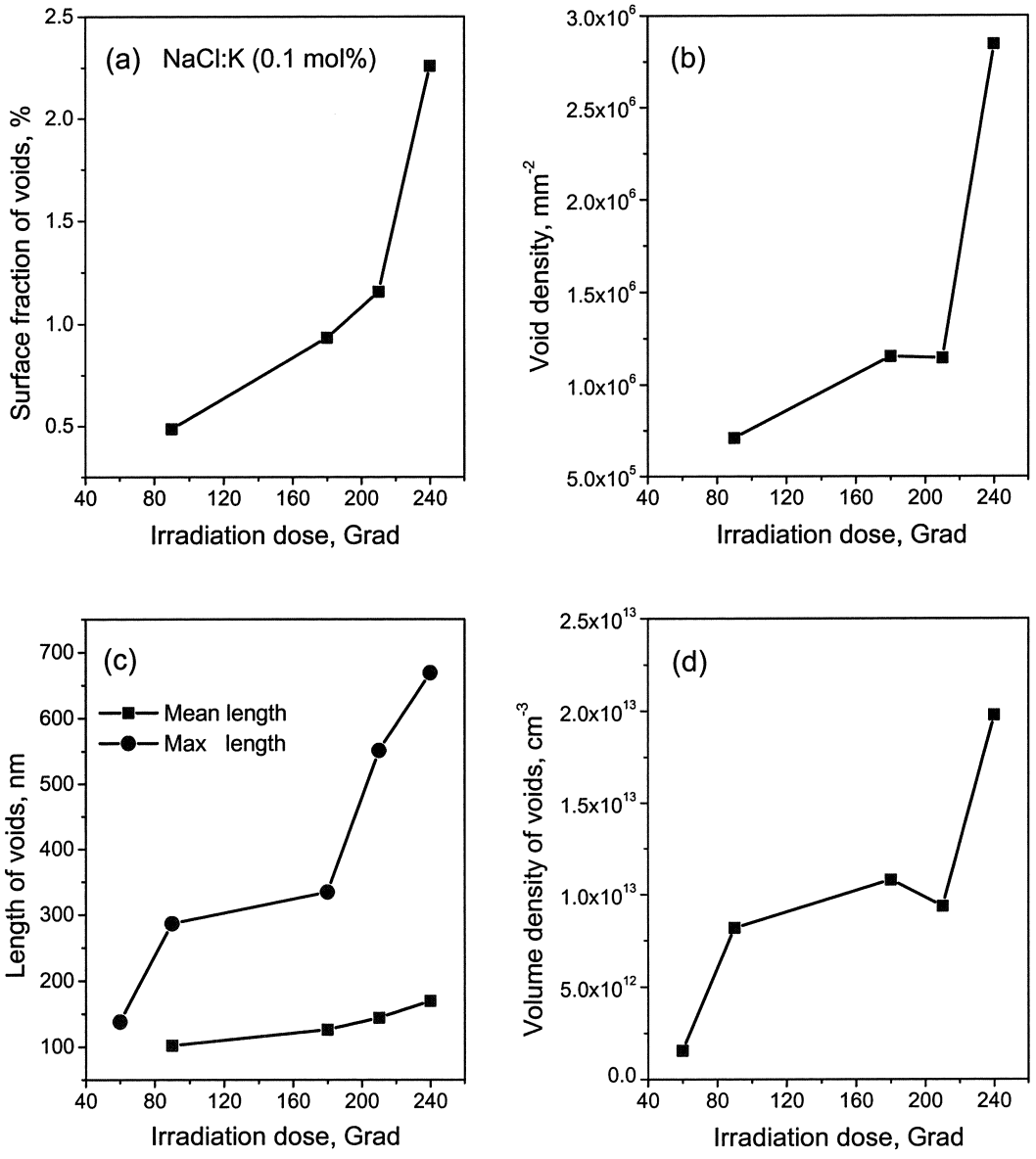

Figure 30. Void mean parameters in electron irradiated NaCl doped with 0.1% K.

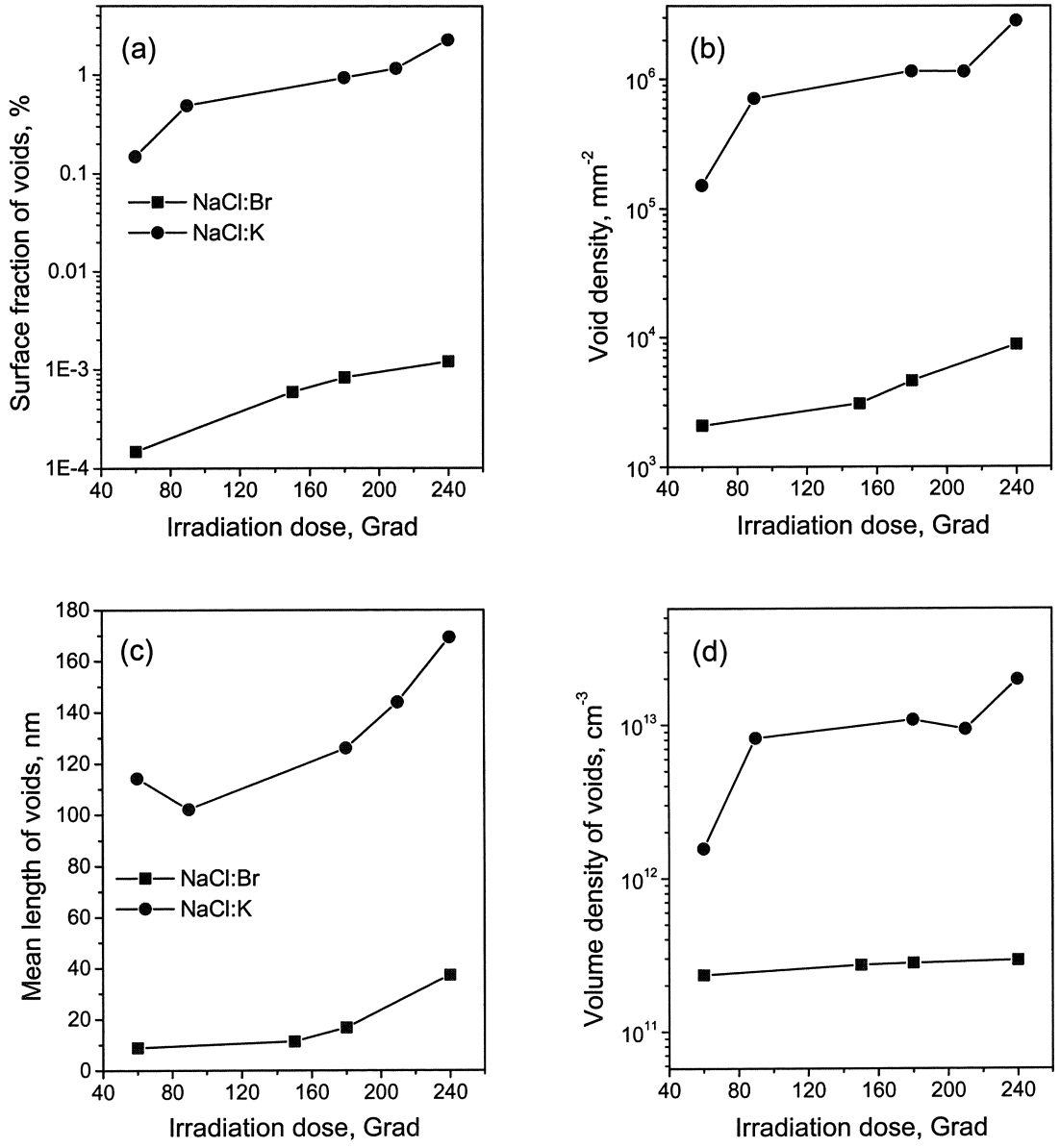

Figure 31. Comparison of void mean parameters in electron irradiated NaCl doped with 0.1% Br and with 0.1%K.

The general trend for all investigated systems is that for slightly and moderately damaged materials there are only a few, very small observable voids. In addition, we note that during this stage the shape of the voids is more or less round, sometimes the objects appeared to be slightly faceted. There are, however, major differences for different dopants. In samples, doped with KCl, elongated voids develop at lower doses as compared to several other dopants and they are significantly larger than in these crystals. It should be noted, that voids with sizes less than 20 nm are very difficult to observe with our equipment. It is possible, that although they cannot be observed, extremely small voids are present in the early stages of the irradiation.

In general, the total volume of the voids increases with increasing dose and colloid volume fraction. For irradiated samples, doped with Br the volume of the voids vs. the dose is approximately linear (fig. 27). For NaCl:0.1%K the production of voids is approximately linear at lower doses, but for the highest doses it is super-linear, and it appears that for these samples the amount of damage does not saturate as a function of the dose up to 300 Grad (fig. 30).

An important point is the nature of the voids and the formation mechanism, which can be used to explain how the voids are created. The models, which have been developed, to describe the formation of radiation damage in NaCl don't give the explanation. The original Jain-Lidiard model does not take into account the production of voids, because we know only since recently from our experimental results of heavily irradiated samples, obtained in our lab, that voids can be produced in NaCl. Our experimental results indicate, that void formation during irradiation is not a marginal effect. In fact it is an essential feature of the radiolysis process, which could not be accounted for in the existing radiolysis models. This implies that the model, describing the radiolytic reactions in NaCl, needs drastic improvements.

During the past stage of this project new ideas have been developed in collaboration with Dr. Dubinko and Dr. Turkin from the NSC-KIPT (Kharkov, Ukraine) to introduce the production of voids as a natural process in a new damage formation theory, which is described below.

3.2.1 New mechanism for radiation damage formation in NaCl

In the alkali halides, the principal radiation damage consists of *bubbles of liquid halogen* formed by agglomeration of *H* centers and of the complementary inclusions of alkali metal *("colloids")* formed by agglomeration of *F* centers [1-4]. Both *H* and *F* centers are primary radiation defects in the halide sub-lattice (fig. 32). The *H* center is a halide interstitial ion with a trapped hole, and an *F* center is the vacancy in the halide sub-lattice with a trapped electron. There is evidence [5] for the formation of numerous *perfect* interstitial dislocation loops, which evidently require both interstitial halogen and interstitial alkali metal. From our results described in the previous section, it follows that large *vacancy voids* (up to hundreds of nm's in size) are formed. The void formation requires agglomeration of both cation and anion vacancies, which cannot be explained by the conventional Jain and Lidiard model [1]. According to the latter, *the dislocation bias* for *H* centers is the driving force for the colloid growth in alkali halides exactly in the same way as for the *void growth in metals* under irradiation. However, the mechanism of dislocation climb [5] used in the Jain and Lidiard model, requires two *H* centers and leaves behind a molecular center, i. e. halogen molecule in a stoichiometric vacancy pair (a stoichiometric vacancy pair consists of two adjacent vacancies, one in the cation and one in the anion sub-lattice). Thus, only dispersed molecular centers and metal colloids can be formed according to the Jain and Lidiard model.

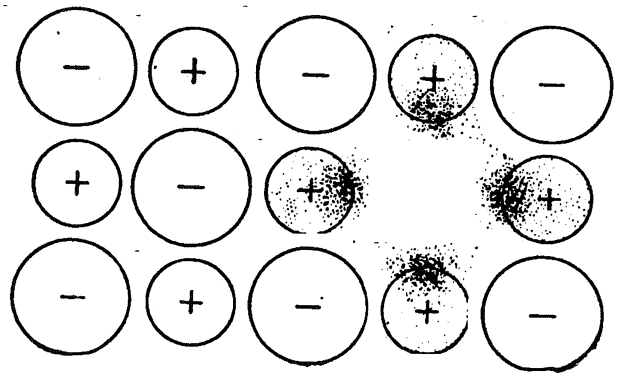

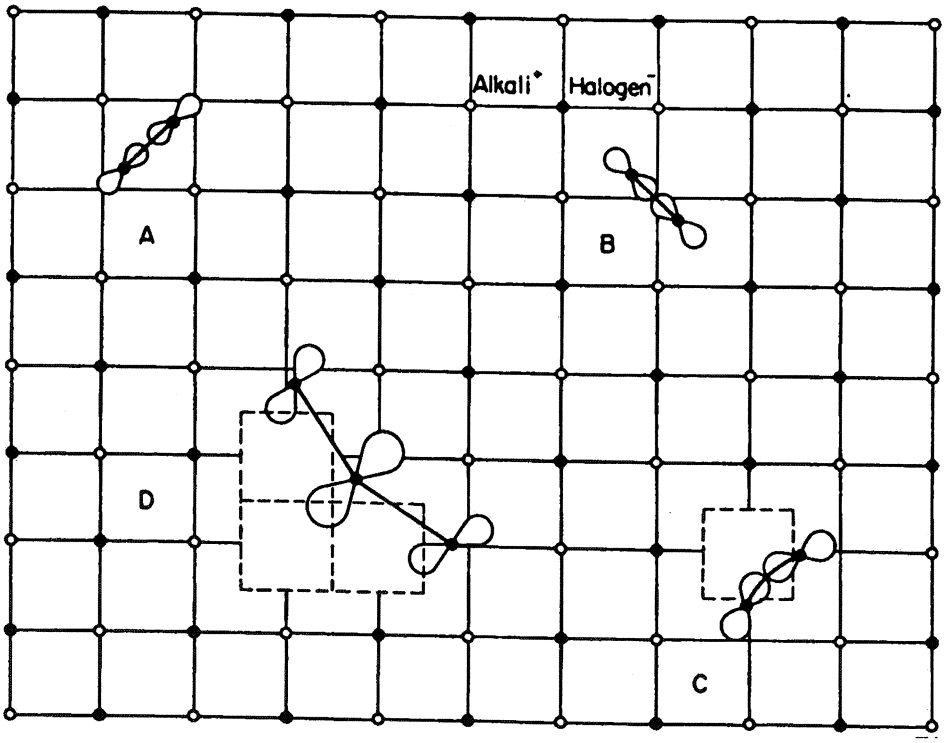

Figure 32.
Top figure: Schematic representation of the *F* center in the NaCl lattice, showing the anion vacancy and the distribution of the trapped electron.
Bottom figure: Schematic representation of a few hole-excess centers in NaCl. Center A is a self-trapped hole, which is called V_K center; it is a hole shared by two neighboring chloride lattice ions. Center B is the *H* center, which consists of a lattice chloride ion, an interstitial chloride ion and a hole shared by these two ions. Center C is the V_F center, which consists of a hole shared by two lattice chloride ions (i.e. like the V_K center) and a neighboring cation vacancy. Center D is a complex hole excess center, which does not play an important role in our considerations.

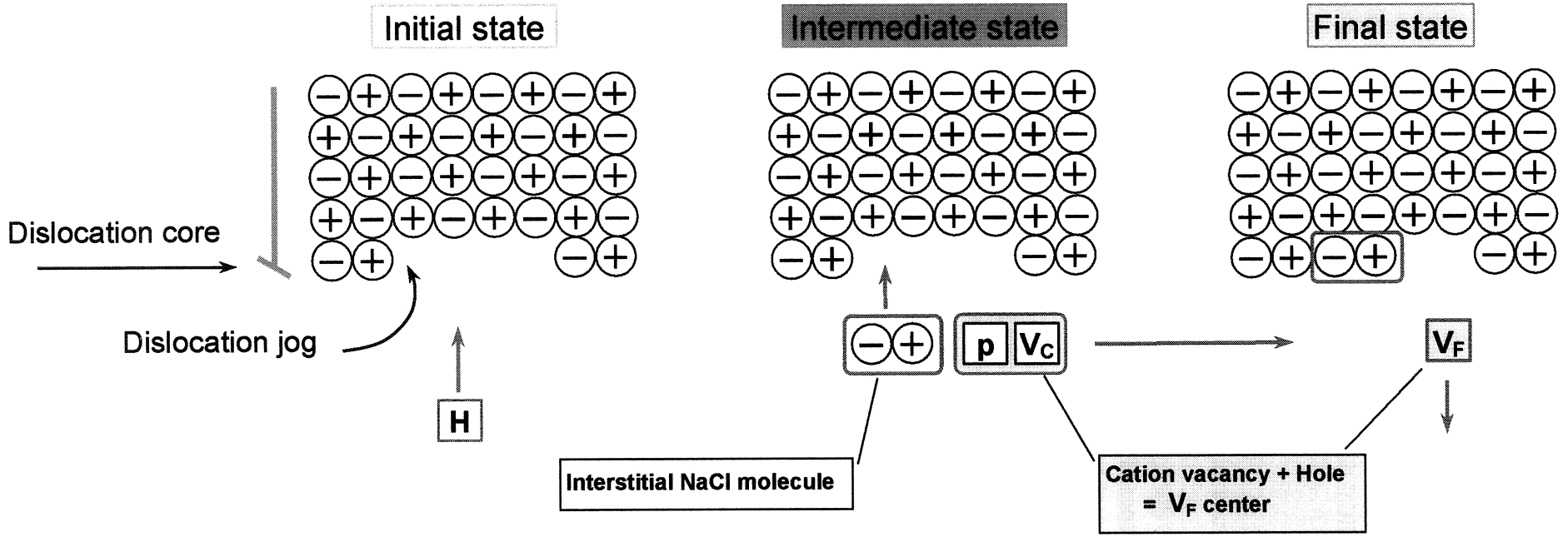

Figure 33. Production of the V_F center as a result of absorption of an H centers by an edge dislocation. When an H center approaches the dislocation, it displaces a lattice cation and forms with it a stoichiometric interstitial pair, $i_A + i_C$, where i_A and i_C are the anion and cation interstitials, respectively and an H center is $i_A + p$ (i.e. an interstitial anion plus a hole, p). A cation vacancy, V_C , and a hole, are produced in the same reaction. The interstitial pair joins a dislocation jog leaving behind the hole trapped at the cation vacancy, that is a V_F center. The recombination reaction of the V_F center with an F center produces a vacancy pair that restores the previous state of the dislocation. So, the production of V_F centers requires a bias of dislocations for H centers.

Below we present a new model of radiation damage formation in alkali halides, which would allow for the creation of halogen bubbles and voids instead of dispersed molecular centers.

3.2.1.1 Production of cation vacancies at dislocations

When an H center approaches a dislocation, it is assumed to displace a lattice cation and form with this ion a stoichiometric interstitial pair (needed for the dislocation climb) *leaving behind a hole trapped by a cation vacancy* (see Fig. 33). The latter is known as the V_F center, which is a mobile "antimorph" of the F center (electron trapped in an anion vacancy). The new reaction requires only one H center as compared to two H centers meeting at the dislocation core, according to the existing mechanism [5] originally proposed by Jain and Lidiard. This is a rather improbable event during irradiation at elevated temperatures, where F centers are mobile as well, and their fluxes to dislocations differ from H center fluxes only due to the dislocation bias. The reaction proposed here is more straightforward, and it should be energetically favorable since the formation energy of V_F center is much less than that of the H center.

As far as the dispersed halogen molecules are concerned, they can be produced in our case as well. Indeed, mobile V_F centers can subsequently recombine with each other to form a halogen molecule sitting in a double vacancy pair (i.e. in two adjacent stoichiometric di-vacancies). This can be a nucleus of a halogen bubble that is formed by the subsequent absorption of H centers as described in the fifth section.

But what is more fundamental is that the V_F center is the "antimorph" of the F center so that their mutual recombination would result in production of a stoichiometric vacancy pair (in both anion and cation sub-lattices. Such a recombination is expected to take place first of all at halogen bubble surfaces since coherent colloids are assumed to be transparent for V_F centers and do not trap them. Indeed, the V_F center is a defect in the cation sub-lattice that is not damaged by coherent colloids.

A consideration, which should be emphasized here, is that the production of V_F centers by dislocations requires excess of incoming H centers over F centers, since the latter induce a back reaction (Fig.33). Similarly, the production of vacancy pairs at the bubble surface requires an excess of incoming F centers over H centers. This means that all reactions involved in the production and absorption of V_F centers at extended defects are controlled by the biases for absorption of H centers or F centers.

An edge dislocation is biased towards absorption of H centers due to stronger elastic interaction with them as compared to F centers. So dislocations are a potential source of extra F centers and V_F centers under irradiation. But this potential can be realized only provided that there are other extended defects with lower (or negative) bias for H centers that could be the sinks for the extra F centers. The dislocation bias is determined by the ratio of relaxation volumes associated with H and F centers, Ω_H / Ω_F, and is given by [10, 11]

$$\delta_d = \ln\left(\frac{\Omega_H}{|\Omega_F|}\right) \Big/ \ln\left(\frac{2}{L_H k_H}\right), \qquad L_H = \frac{\mu b(1+\nu)}{3\pi kT(1-\nu)}\Omega_H \tag{1}$$

where b is the host lattice spacing, μ is the shear modulus of the matrix, ν is the Poisson ratio, k_H is the square root of the total sink strength of all ED for H centers, and kT has its

usual meaning. In the following section we consider the biases of other ED modeled as spherical inclusions in an elastic medium.

3.2.1.2 Bias of spherical inclusions due to elastic interaction difference (EID)

A bias of a sink for absorption of point defects (PD) of a certain type is given by the difference between the sink efficiencies to capture defects of opposite signs (*H* and *F* centers in the case under consideration). Since irradiation produces equal numbers of *H* and *F* centers, the radiation-induced growth (or shrinkage) rate of each sink is directly proportional to the difference between its bias and the mean bias of the system. The derivation of sink efficiencies, Z^S, involves the solution of the diffusion problem in the sink region of influence with consideration of its elastic interaction with PD both in equilibrium and in the saddle point configurations. As was summarized in Refs. [10, 11, 21], the former determines the image (im) [22], the modulus (μ) [23] and elastic anisotropy (ea) [24] modes of interaction between a sink and PD modeled as spherical inclusions in an elastic medium. On the other hand, the diffusion parameters of PD are those in saddle points for diffusion jumps, which are also affected by the stress field of the sink. The immediate consequence of this is the stress-induced anisotropy of PD near the sink, which influences its capture efficiency [25-27]. If each of these effects causes a small correction to Z^S, then the resulting expression for a capture efficiency of a sink of the radius *R* can be obtained approximately by summation of all corresponding corrections, which are to be evaluated separately, as has been done for metals in Refs. [10, 11, 21]

$$Z_n^S = 1 + \Delta Z_n^{im} + \Delta Z_n^{\mu} + \Delta Z_n^{ea} + \Delta Z_n^{ed}, \qquad n = H, F, \tag{2}$$

where the subscripts determine the PD type, and the superscript in Z^S determines the sink type, while the ΔZ values correspond to the above mentioned effects and are given by the following formulas

$$\Delta Z_n^{im} = \frac{\alpha_n^{im} b}{R}, \qquad \alpha_n^{im} = \left[\frac{(\mu - \mu_C)(1+\nu)^2 \Omega_n^2}{36kT(1-\nu)} \right]^{1/3}, \tag{3}$$

$$Z_n^c(r_c) \approx 1 + \frac{\alpha_n}{r_c} - \frac{3}{56} \frac{\alpha_n^{\mu}}{kT\mu^2} (\sigma_{rr} - \sigma_H)^2 . , \tag{4}$$

$$\Delta Z_n^{ea} = -1.7 \times 10^{-3} \xi^2 \left(\frac{1+\nu}{1-2\nu} \right)^2 \left(\frac{\Omega_n \sigma_{rr}}{kT} \right)^2 \tag{5}$$

$$\Delta Z_n^{ed} = \alpha_n^d \frac{\sigma_{rr}}{\mu}, \quad \alpha_n^d = -\left(5d_n^{(2)} + 2d_n^{(3)}\right)/40 \tag{6}$$

where μ_C is shear modulus of the inclusion, Ω_n is the point defect relaxation volume, α_n^{μ} is the PD polarizability, σ_{rr} is the normal stress at the inclusion boundary, $d_n^{(2)}$ and $d_n^{(3)}$ are the

independent components of the "elastodiffusion tensor" [27], and ξ is the elastic anisotropy parameter.

The inclusion bias for H centers, δ_s, is given by the difference $\left(Z_H^s / Z_F^s\right) - 1$:

$$Z_F^s \delta_s(R, \sigma_{rr}) = \alpha^{im}(b/R) + \alpha^d(\sigma_{rr}/\mu) + \alpha^{\mu,\xi}(\sigma_{rr}/\mu)^2, \tag{7}$$

$$\alpha^{im} = (\alpha_H^{im} - \alpha_F^{im})/b, \qquad \alpha^d = (\alpha_H^d - \alpha_F^d), \tag{8}$$

$$\alpha^{\mu,\xi} = \frac{3}{56kT}(\alpha_F^\mu - \alpha_H^\mu) - 1.7\times10^{-3}\left(\frac{1+\nu}{1-2\nu}\right)^2\left(\frac{\mu\xi}{kT}\right)^2\left(\Omega_H^2 - \Omega_F^2\right), \tag{9}$$

where a factor Z_F^s in most cases is close to unity, and the dimensionless bias constants, α, are defined to be positive as shown in Table 1. It can be seen that δ_s depends on the inclusion radius and stress state that is different for colloids, gas bubbles and voids. Below they are considered in detail.

3.2.1.3 Colloid bias

Below the melting temperature, metallic colloids can be in two principally different states. Since the colloids are formed by F centers they are expected to be coherent with the host matrix as long as they are small. In this, coherent, state, there exists a misfit, ε, which is equal to the difference between the lattice constants of the colloid and that of the host lattice. Positive (or negative) misfit means that colloid is under compressive (or tensile) stress given by $\sigma_{rr} = \sigma_\varepsilon$:

$$\sigma_\varepsilon = -\frac{3K_C\varepsilon}{1 + 3K_C/4\mu}, \tag{10}$$

where K_C is the colloid bulk modulus. The misfit energy increases with increasing colloid radius, which favors energetically the loss of coherency at some threshold radius, R_C^{th}, and this leads to a transition to the incoherent state. Consequently, the biases of the two colloid types are different. The first is given by

$$\delta_{coh}(R_C) = \alpha_c^{im} b/R_C + \delta_\varepsilon, \qquad \delta_\varepsilon = \alpha^d(\sigma_\varepsilon/\mu) + \alpha^{\mu,\xi}(\sigma_\varepsilon/\mu)^2, \tag{11}$$

where δ_ε is the constant misfit bias, and α_c^{im} is the constant of the image interaction, which for a colloid is given according to (3) by the difference

$$\alpha_c^{im} = \left(\frac{0.7\omega(\mu - \mu_c)(1+\nu)^2}{36kT(1-\nu)}\right)^{1/3}\left(\Omega_H^{2/3} - \Omega_F^{2/3}\right) \tag{12}$$

The incoherent colloid bias is inversely proportional to its size:

$$\delta_{in}(R_C) \approx \left(\alpha_c^{im} + \frac{\alpha^d 2\gamma_{in}}{\mu b}\right)\frac{b}{R_C} + \frac{\alpha^{\mu,\xi}}{\mu^2}\left(\frac{2\gamma_{in}}{R_C}\right)^2, \tag{13}$$

In *NaCl*, coherent sodium colloids have a negative misfit (6.8% for *fcc*- and 3.6% for *bcc*-lattices) and, hence, a positive misfit bias, which means that they can form only if the dislocation bias is larger than δ_ε.

3.2.1.4 Bias of halogen bubbles and vacancy voids

The normal stress at the bubble surface is given by the difference between its surface tension and the gas pressure, P: $\sigma_{rr} = 2\gamma/R_B - P$, where γ is the surface free energy of a bubble. Accordingly, its bias takes the form:

$$\delta_B(R_B, P) \approx \alpha^{im}\frac{b}{R_B} + \frac{\alpha^d}{\mu}\left(\frac{2\gamma}{R_B} - P\right) + \frac{\alpha^{\mu,\xi}}{\mu^2}\left(\frac{2\gamma}{R_B} - P\right)^2, \tag{14}$$

where α^{im} is given by eq. (12) at $\mu_c = 0$. From e. (14) it follows that the bubble bias has a negative constituent proportional to the gas pressure, which will be shown to play a critical role in the void formation.

For voids we have $P << 2\gamma/R$, and so their bias decreases steadily with increasing size similar to that of incoherent colloids:

$$\delta_V(R_V) \approx \left(\alpha^{im} + \frac{\alpha^d 2\gamma}{\mu b}\right)\frac{b}{R_V} + \frac{\alpha^{\mu,\xi}}{\mu^2}\left(\frac{2\gamma}{R_V}\right)^2 \tag{15}$$

Accordingly, voids can grow if their size exceeds a critical value, which is determined by the mean bias and the void bias constants. Below this size, voids would capture more H centers than F centers, which would lead to the accumulation of small amounts of gas within the vacancy voids.

3.2.1.5 Rate equations for point defects

In this paper, we will concentrate at the temperature range, where all PD are mobile but their thermal emission from ED is yet negligibly small as compared to the production by irradiation. In this range, the mean concentrations of primary PD, $\bar{c}_{F,H}$ are determined by the rate equations

$$\frac{d\bar{c}_{F,H}}{dt} = K - k_{F,H}^2 D_{F,H}\bar{c}_{F,H} - \beta_r(D_F + D_H)\bar{c}_F\bar{c}_H; \tag{16}$$

$$k_{F,H}^2 = Z_{F,H}^d \rho_d + Z_{F,H}^C 4\pi N_C \overline{R}_C + Z_{F,H}^B 4\pi N_B \overline{R}_B + Z_{F,H}^V 4\pi N_V \overline{R}_V \qquad (17)$$

where K is the generation rate of F and H centers, $k_{F,H}^2$ are the sink strengths associated with their absorption by ED, β_r is the constant of their bulk recombination, ρ_d is the dislocation density, N_S is the number density of S-type ED, and $\overline{R}_S$ is the mean radius.

The concentration of V_F centers is determined by their production at dislocations, the bulk recombination and capture by voids, bubbles and impurity traps (coherent colloids do not capture V_F centers):

$$\frac{d\overline{c}_v}{dt} = K_v - k_v^2 D_v \overline{c}_v - \beta_r (D_v + D_v)\overline{c}_v^{\,2}, \qquad (18)$$

$$K_v = (Z_H^d D_H \overline{c}_H - Z_F^d D_F \overline{c}_F)\rho_d, \quad k_v^2 = Z_v^V 4\pi N_V \overline{R}_V + Z_v^B 4\pi N_B \overline{R}_B + \beta_{iv}\overline{c}_i, \qquad (19)$$

where $\overline{c}_i$ is the concentration of impurity ions and β_{iv} is their V_F-capture efficiency.

We are interested in the steady state solutions so that $d\overline{c}_n/dt = 0$, and PD concentrations are connected by a simple relation:

$$D_F \overline{c}_F = D_H \overline{c}_H \left(k_H^2 / k_F^2\right). \qquad (20)$$

Substituting Eq. (20) into Eq. (19) and performing some algebraic operations we obtain that the V_F center source is proportional to the difference between the dislocation bias, δ_d, and the mean bias of all ED, $\overline{\delta}$:

$$K_v = D_H \overline{c}_H Z_F^d \rho_d \left(\delta_d - \overline{\delta}\right), \quad \delta_d = \frac{Z_H^d - Z_F^d}{Z_F^d}, \quad \overline{\delta} = \frac{k_H^2 - k_F^2}{k_F^2}, \qquad (21)$$

3.2.1.6 Nucleation and growth of colloids and bubbles

Colloids. The growth (or shrinkage) rate of coherent colloids is given by the difference of F and H center influxes, or equivalently, by the difference between the mean bias and the colloid bias that depends on its size and structure/aggregation state:

$$\frac{dR_C}{dt} = \frac{1}{R_C}\left[Z_F^C D_F \overline{c}_F - Z_H^C D_H \overline{c}_H\right] = \frac{1}{R_C} Z_F^C D_H \overline{c}_H \left(\overline{\delta} - \delta_C\right). \qquad (22)$$

Accordingly, the colloid growth rate is negative below some critical radius, $R_C^{crit} = \alpha^{im} b/\left(\overline{\delta} - \delta_\varepsilon\right)$, which determines the nucleation barrier and, hence, the nucleation rate of colloids.

We will consider the stage after the nucleation is over. At this stage, the final number density of colloids does not depend on the nucleation rate, but it is determined by the mechanism of the radiation induced coarsening (RIC). The RIC mechanism was proposed [22] to determine the late stage evolution of voids under irradiation of metals in the same way as the Ostwald ripening mechanism determines thermal aging of precipitates. However, the RIC mechanism has a purely kinetic origin being the result of the inversely proportional dependence of void bias for interstitial absorption on the void radius. The colloid bias has practically the same dependence, since a constant constituent from the misfit does not influence the competition between colloids of different sizes but limits an overall supply of extra F centers coming from other ED. So an asymptotic in time solution for the number density of colloids can be found to depend on the difference between the biases of other sinks and the mean bias:

$$N_C = \frac{\sum_{S=d,V,B} k_S^2(\delta_S - \bar{\delta})}{2\pi\alpha_c^{im} b}, \tag{23}$$

where k_S^2 is the sink strength of s-type. In this regime, the mean radius of colloids is completely determined by their bias constant, α_c^{im}, and by the irradiation and material parameters (via the mean concentration of H centers):

$$\frac{d\bar{R}_C}{dt} = \frac{\alpha_c^{im} b}{2\bar{R}_C^{\,2}} D_H \bar{c}_H \ . \tag{24}$$

Accordingly, the rate of growth of the colloid volume fraction is given by

$$\frac{dV_C}{dt} = \sum_{S=d,V,B} k_S^2 (\delta_S - \bar{\delta}) D_H \bar{c}_H \tag{25}$$

<u>*Bubbles.*</u> Nucleation of halogen bubbles may start as a result of recombination of V_F centers, the rate of which is proportional to the square of V_F center concentration. The steady-state concentration of point defects is inversely proportional to their mobility. The mobility of V_F centers is close to that of F centers (their migration activation energies are 0.7 and 0.8 eV, respectively), which is much lower than the mobility of H centers having migration energy of 0.1 eV. Accordingly, the recombination of V_F centers is much stronger than that of H centers and is more likely to provide immobile molecular centers in the perfect crystal. In real crystals, however, impurity ions can act as traps for H centers and provide nucleation sites. When several H centers come to such a site they combine to form a halogen bubble which "digs its own hole in the lattice by displacing a lattice cation and a neighboring lattice anion on to the edge of the dislocation loop" [1]. This process is exactly analogous to the loop punching by growing helium bubbles in metals [28, 29]. The threshold pressure for the loop punching is inversely proportional to the bubble radius [28, 30]: $\sigma_{rr}^{th} \approx -(\mu b + 2\gamma)/R_B$. Substituting it into Eq. (14) we obtain a simple dependence of the bubble bias on the radius:

$$\delta_B(R) \approx \frac{\alpha^{im} b}{R} - \alpha^d \frac{b}{R} + \alpha^{\mu,\xi} \left(\frac{b}{R}\right)^2, \tag{26}$$

from which it follows that a small halogen bubble, $R < R^{th}$, has a higher bias for H centers than the mean bias, and so it can absorb extra H centers and grow via SIA-loop punching, which can be an *additional driving force* for the separation of the H and F centers into bubbles and metal colloids.

$$R^{th} = b\left(-\frac{1}{2}\frac{\alpha^d - \alpha^{im}}{\bar{\delta}} + \sqrt{\frac{1}{4}\left(\frac{\alpha^d - \alpha^{im}}{\bar{\delta}}\right)^2 + \frac{\alpha^{\mu,\xi}}{\bar{\delta}}} \right), \tag{27}$$

At $R > R^{th}$, extra F centers start to arrive at the bubble surface and recombine with V_F centers producing stoichiometric vacancy pairs that would increase the bubble size and so decrease the pressure below the threshold level for loop punching. After that, the bubble pressure is determined both by the number of halogen molecules and the number of vacancy pairs in it via the equation of state. Accordingly, the bubble evolution takes place in the two-dimensional phase space of the number of halogen molecules, n_{Gas}, and the number of vacancy pairs in it, $n_{Vac} = 4\pi R_B^3/\omega$, where ω is the molecular volume of the host NaCl lattice. The first one increases if $\delta_B > \bar{\delta}$ while the second one increases in the opposite case of $\delta_B < \bar{\delta}$, such as follows:

$$\frac{dn_{Gas}}{dt} = 2\pi R_B Z_F^B D_H \bar{c}_H \left[\delta_B(n_{Vac}, n_{Gas}) - \bar{\delta}\right]\Theta\left(\delta_B - \bar{\delta}\right), \quad \Theta(x) \equiv \begin{cases} 1, & x > 0 \\ 0, & x \le 0 \end{cases} \tag{28}$$

$$\frac{dn_{Vac}}{dt} = 4\pi R_B Z_F^B D_H \bar{c}_H \left[\bar{\delta} - \delta_B(n_{Vac}, n_{Gas})\right]\Theta\left(\bar{\delta} - \delta_B\right), \tag{29}$$

where the dependence $\delta_B(n_{Vac}, n_{Gas})$ can be found from Eq. (14) using the appropriate equation of gas state such as the modified Van der Waals gas law:

$$P(n_{Vac}, n_{Gas}) = n_{Gas} kT / (n_{Vac}\omega - n_{Gas}\omega_{Gas}), \tag{30}$$

where ω_{Gas} is the effective volume occupied by one halogen molecule in the bubble.

Now, Eqs. (28) and (29) are the components of the vector of the bubble motion rate in the n_{Gas}, n_{Vac} phase space that are schematically shown in Fig. 34. Below some critical number of halogen molecules, a bubble is forced to occupy a stable position along the curve in the "valley" where both components of the bubble growth rate are zero. A gradual decrease of the mean bias, which is due to the colloid growth, makes the bubbles move adiabatically along the curve until they reach a critical point, beyond which n_{Vac} would increase inexorably at n_{Gas} remaining constant. Thus a conversion of bubbles to voids would take place after some threshold irradiation dose. Below that dose, bubbles are in a quasi-steady state with their bias equal to the mean bias of the system. The total number of halogen molecules in bubbles and their volume fraction increases steadily with increasing colloid volume fraction, and is given by the balance between the amounts of halogen molecules in bubbles and metal atoms in colloids:

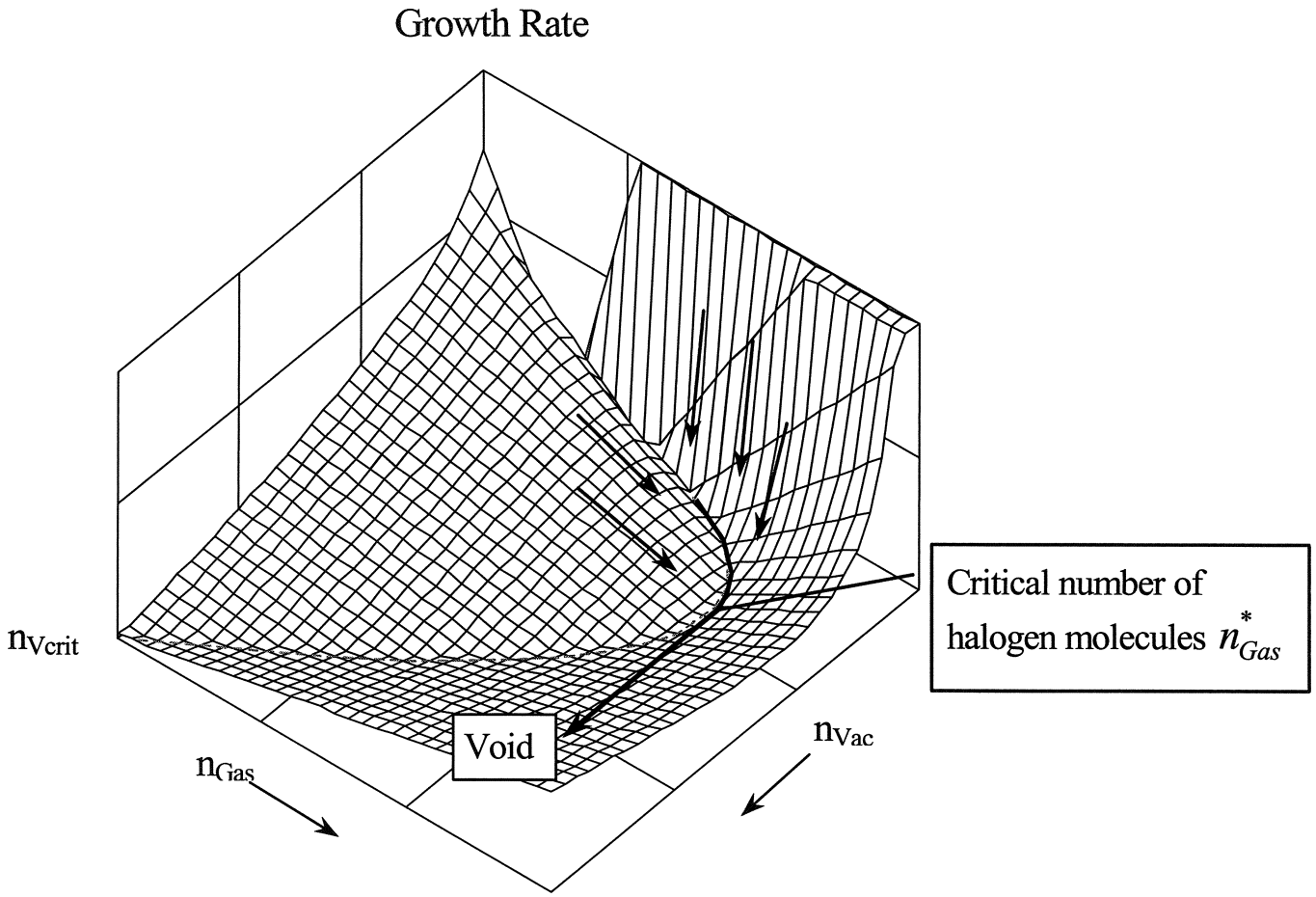

Figure 34. The evolution path of bubbles resulting in their conversion to voids. Below the critical number of halogen molecules, n^*_{Gas}, the bubbles move slowly along the valley, which provide the only stable path towards the point where the critical number of halogen molecules is reached. After the point is reached, the number of vacancies starts to increase, while the number of gas molecules stays constant. n_{Vcrit} is the critical number of vacancies required for growth of an empty void ($n_{Gas} = 0$).

$$N_{Gas}(t) = \frac{1}{2\omega} V_C(t) \quad , \qquad V_B(t) \approx \frac{\omega_{Gas}}{2\omega} V_C(t) \tag{31}$$

So to find the mean number of halogen molecules in one bubble, $\overline{n}_{Gas}$, one should know the bubble number density. A homogeneous nucleation from the recombination of V_F centers would result in the final concentration of bubbles, ωN_B^0, close to the maximum steady-state concentration of V_F centers, which can be easily estimated from Eq. (18) as follows:

$$\omega N_B^0 \approx \sqrt{K_v / D_v \beta} \tag{32}$$

Impurities can either facilitate or hamper the nucleation process, which will be shown to have a strong effect on the whole microstructural evolution.

3.2.1.7 Critical parameters controlling bubble-void transition

The critical number of halogen molecules required for the bubble-void transition, n_{Gas}^*, corresponds to the condition that Eq. (29) has no roots, i.e., $dn_{Vac}/dt > 0$ for any value of n_{Vac}. The mathematical procedure is exactly the same as that used to find a critical umber of gas atoms for the bubble-void transition in metals [31, 10]. In the case when radiation-induced PD dominate over thermal PD, one has in the linear approximation in stress ($\alpha^{\mu,\xi} = 0$) [10, 11]

$$n_{Gas}^* = \frac{8\pi\gamma_K R_{Vcrit}{}^2 (1+\varepsilon)^2}{kT(2+\varepsilon)^4}, \quad R_{Vcrit} = \frac{2\gamma_K}{\sigma_K}, \tag{33}$$

$$\varepsilon = (1+3\varphi)^{1/2}, \quad \varphi = \sigma_K \omega_{Gas} / kT, \tag{34}$$

$$\gamma_K = \gamma + \mu b \frac{\alpha^{im}}{2\alpha^d}, \quad \sigma_K = \mu \frac{\overline{\delta}}{\alpha^d}, \tag{35}$$

where R_{Vcrit} is the critical radius for the vacancy void growth (which corresponds to n_{Vcrit} at $n_{Gas} = 0$ in fig. 31), γ_K and σ_K are the effective parameters, which play the same role as the surface energy and tensile external stress that can induce void formation from thermal vacancies without irradiation [10].

3.2.1.8 Formation and growth rates of vacancy voids

The gas pressure in the growing void drops very rapidly as compared to the surface tension value, and the void growth rate is determined by the excess F center flux:

$$\frac{dR_V}{dt} = \frac{1}{R_V}\left(Z_F^V D_F \overline{c}_F - Z_H^V D_H \overline{c}_H\right) = \frac{1}{R_V} Z_F^V D_H \overline{c}_H \left(\overline{\delta} - \delta_V^{eff}\right), \tag{36}$$

where δ_V^{eff} is equal to δ_V defined by Eq. (15) provided that there are sufficient V_F centers available for the recombination with extra F centers to produce stoichiometric vacancy pairs. In the opposite case, a flux of V_F centers is a limiting factor of the void growth, which is then given by

$$\frac{dR_V}{dt} = \frac{1}{R_V} Z_v^V D_v \bar{c}_v, \tag{37}$$

It is possible to describe both these regimes by Eq. (36), by defining the following expression for the effective void bias that takes into account both V_F and F center fluxes and depends on the sink strengths and biases:

$$\delta_V^{eff}(R_V, k_S^2) = \begin{cases} \delta_V(R_V), & \text{if } \delta_V(R_V) > \delta_{VS}(k_S^2) \\ \delta_{VS}(k_S^2), & \text{if } \delta_V(R_V) < \delta_{VS}(k_S^2) \end{cases}, \tag{38}$$

$$\delta_{VS}(k_S^2) \equiv \frac{\delta_m(k_d^2 + k_V^2 + k_B^2 + k_i^2) - \delta_d k_d^2}{k_V^2 + k_B^2 + k_i^2}, \tag{39}$$

$$\delta_m \equiv \frac{\delta_C\left[k_V^2 k_C^2 + k_C^2(k_B^2 + k_i^2)\right] + \delta_d k_d^2(k_B^2 + k_i^2)}{k_V^2 k_C^2 + (k_B^2 + k_i^2)(k_d^2 + k_C^2)}, \tag{40}$$

where δ_C is the mean colloid bias.

Then the expression for the mean bias of the system of all ED can be written as

$$\bar{\delta}(k_S^2) = \frac{k_d^2 \delta_d + k_C^2 \delta_C + k_V^2 \langle \delta_V^{eff}(R_V, k_S^2) \rangle}{k_d^2 + k_C^2 + k_V^2}, \tag{41}$$

Note that the bubble bias equals the mean bias of the system (sect. 5.2), and hence it does not directly influence its value.

The nucleation rate of voids is controlled by the rate of transition through the critical point (Fig. 34) and can be estimated as follows:

$$\frac{dN_V}{dt} \approx \frac{D_v \bar{c}_v}{\omega_{Gas} n_{Gas}^*} Z_v^B 4\pi N_B R_B (\bar{\delta} - \delta_c) \Theta(n_{Gas} - n_{Gas}^*). \tag{42}$$

It is proportional to the recombination rate of V_F and F centers at bubble surfaces, which is determined by the recombination efficiency, Z_v^B, expected to be quite small due to the competition with a recombination between F centers and halogen molecules in bubbles.

3.2.1.9 Simultaneous evolution of ED at high dose irradiation

Figure 35 illustrates the radiation-induced reactions between point defects (PD) and extended defects (ED) based on the present model. Primary radiation-induced PD, namely, H and F centers, separate ultimately into bubbles, dislocations and metal colloids, which results in the production of secondary PD (V_F centers) and ED (vacancy voids).

During the late stage of radiolysis, after the nucleation of colloids and bubbles has been completed, we have simple asymptotic equations both for their number densities Eqs. (23), (32) and mean sizes Eq. (24) or volume fractions Eqs. (25) and (31) expressed through the steady-state dislocation density. The latter is known to saturate under irradiation (after approximately 10 Grad, which corresponds to about one displacement per atom, dpa) at some value (about 10^{14} m^{-2}), which we assume to be a fixed parameter controlled by the impurity content.

The void formation starts as the number of the gas molecules per bubble reaches the critical value, as shown in the fig. 36. After that the void number density depends on the rate of transition from bubbles (42), which we have calculated assuming two very different values for the recombination efficiency of V_F and F centers at bubble surfaces, Z_v^B (fig. 37) The first value for $Z_v^B = 10^{-5}$ is deduced from a comparison of the resulting void formation rate with our experimental data for KBF_4 doped samples, in which we have the maximum void formation rate. The second value is four orders of magnitude higher, which allows investigating some feedback effects due to the numerous void formation.

In the latter case, there arises a strong competition between voids and colloids that have higher bias due to misfit stress. So, if the void number density is high enough, they suppress the growth of the colloid and, consequently, bubble volume fractions (Fig. 38b). The mean colloid radius keeps growing, however (Fig. 39b), at the expense of the dissolution of smaller colloids due to the RIC mechanism [22]. As a result, the void and colloid mean sizes are comparable and difficult to observe with our equipment.

The evolution of the system in the case of the lower bubble-void transition rate is shown in Figs. 36a –39a. The void influence on the mean system bias is weak due to their low number density (Fig. 37a), but their radius growth rate is much faster (Fig. 39a). Consequently, for doses higher than 100 Grad, the void dimensions exceed the mean distance between colloids and bubbles, (R_{Vexp} in the Fig. 39a), which makes possible the capture of the latter by growing voids that would eventually bring the halogen gas and metal to a back reaction inside the voids (see section 3.3).

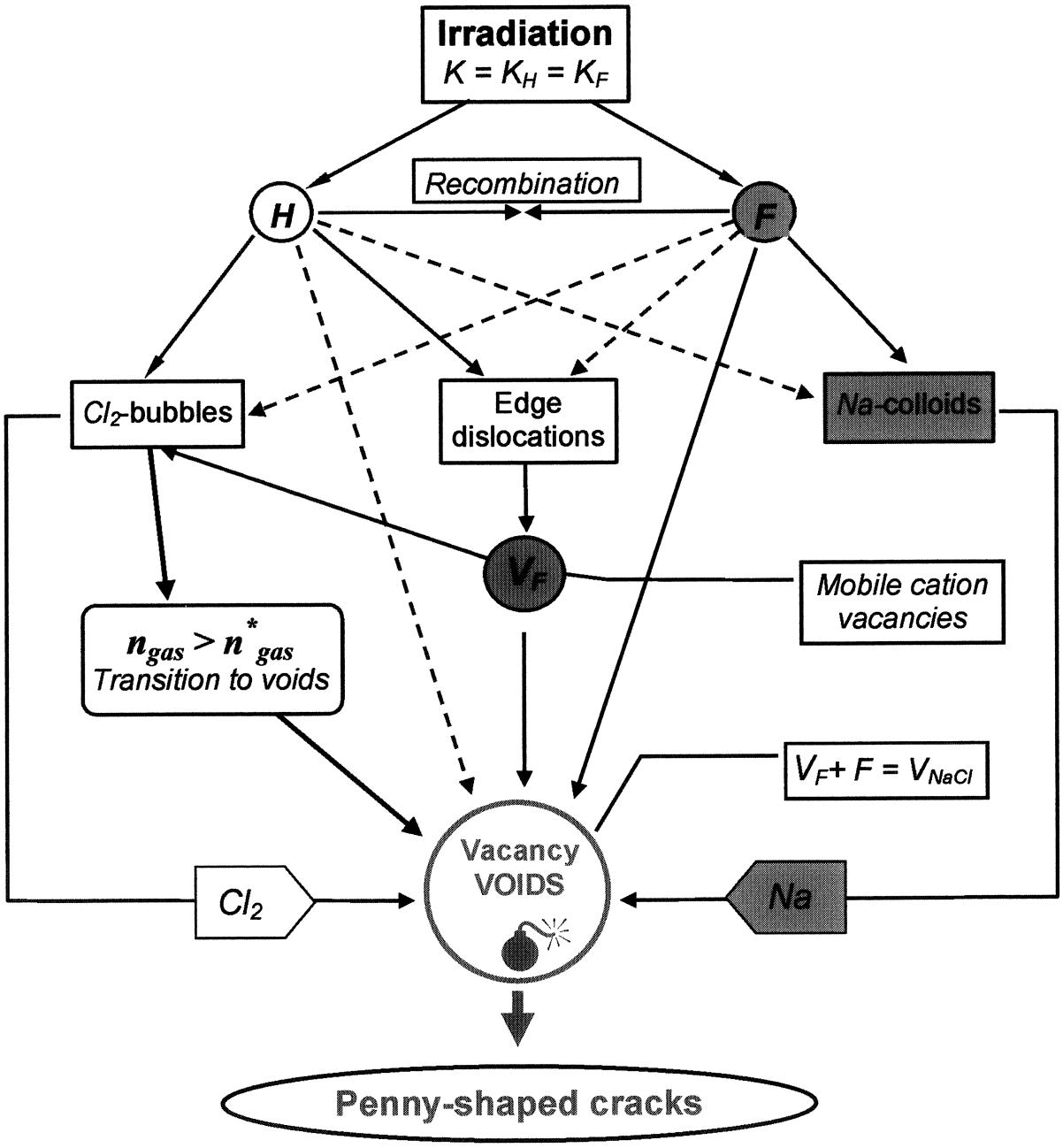

Figure 35. Diagram of radiation-induced reactions between point defects (*H*- and *F*-centers, and cation vacancies) and extended defects (bubbles, dislocations and colloids) resulting in the void formation. Release of stored energy due to absorption of chlorine bubbles and sodium colloids induces the void-crack transition and a subsequent fracture of crystal.

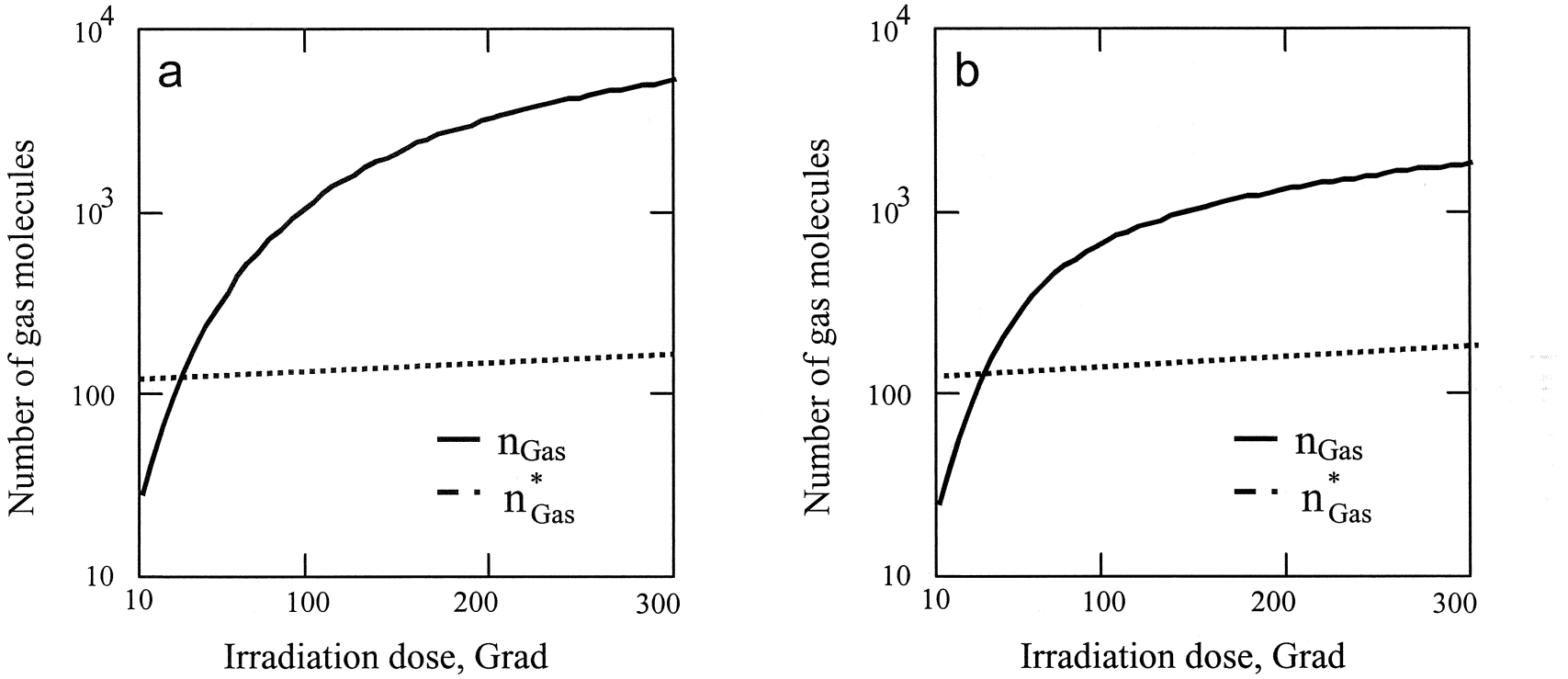

Figure 36. Dose dependence of the mean number n_{Gas} of gas molecules per a bubble at $K = K_I = 240$ Mrad/h, and $T = 100^0$C calculated for two different values for the recombination efficiency of V_F and F centers at bubble surfaces, $Z_v^B = 10^{-5}$ (a) and $Z_v^B = 10^{-1}$ (b).

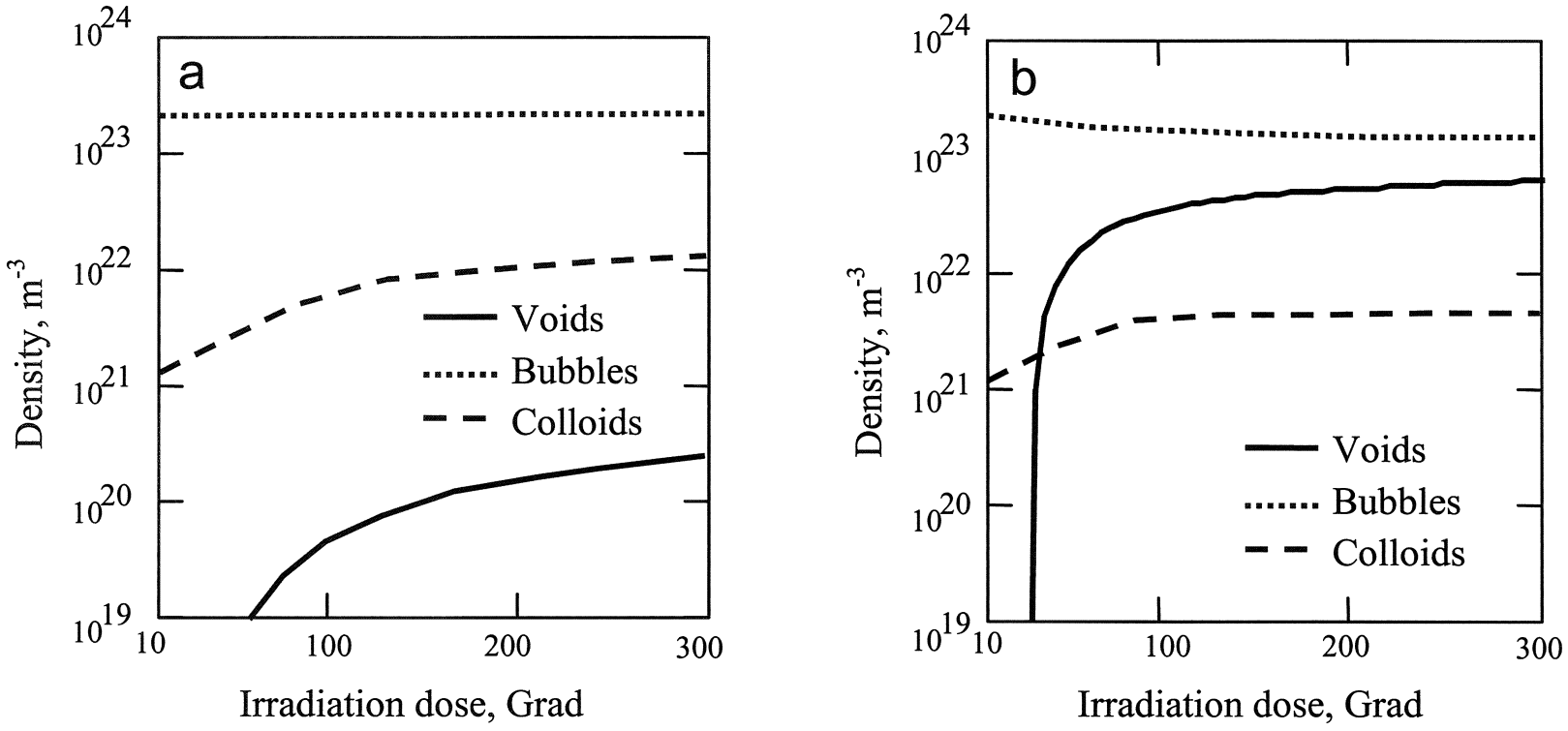

Figure 37. Dose dependence of the number densities of voids and colloids at $K = K_I = 240$ Mrad/h, and $T = 100^0$C calculated for two different values for the recombination efficiency of V_F and F centers at bubble surfaces, $Z_v^B = 10^{-5}$ (a) and $Z_v^B = 10^{-1}$(b). The dislocation and bubble densities were assumed to be 5×10^{14} m^{-2} and 2×10^{23} m^{-3}, respectively.

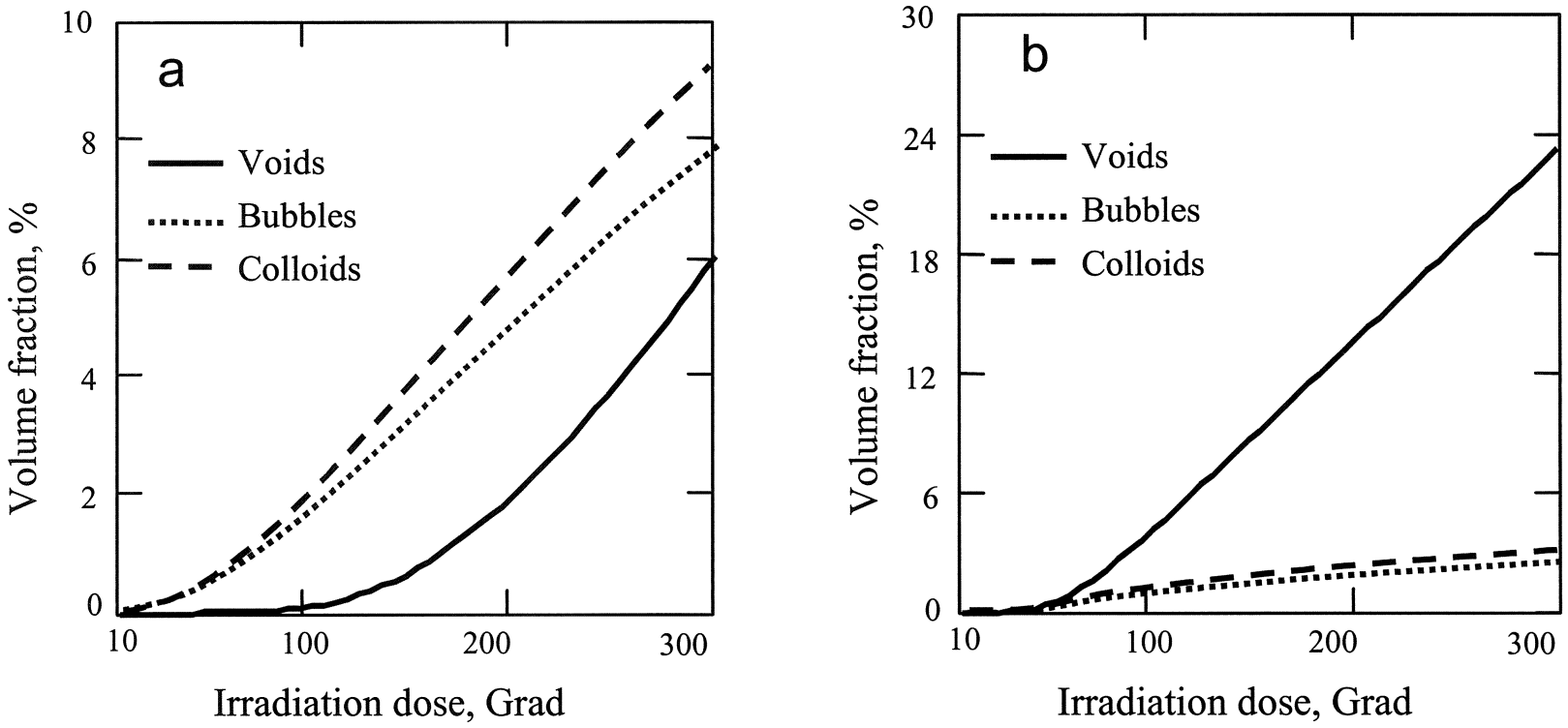

Figure 38. Dose dependence of the volume fractions of voids and colloids at $K = K_1 = 240$ Mrad/h, and $T = 100^0$C calculated for two different values for the recombination efficiency of V_F and F centers at bubble surfaces, $Z_v^B = 10^{-5}$ (a) and $Z_v^B = 10^{-1}$(b). The dislocation and bubble densities were assumed to be 5×10^{14} m^{-2} and 2×10^{23} m^{-3}, respectively.

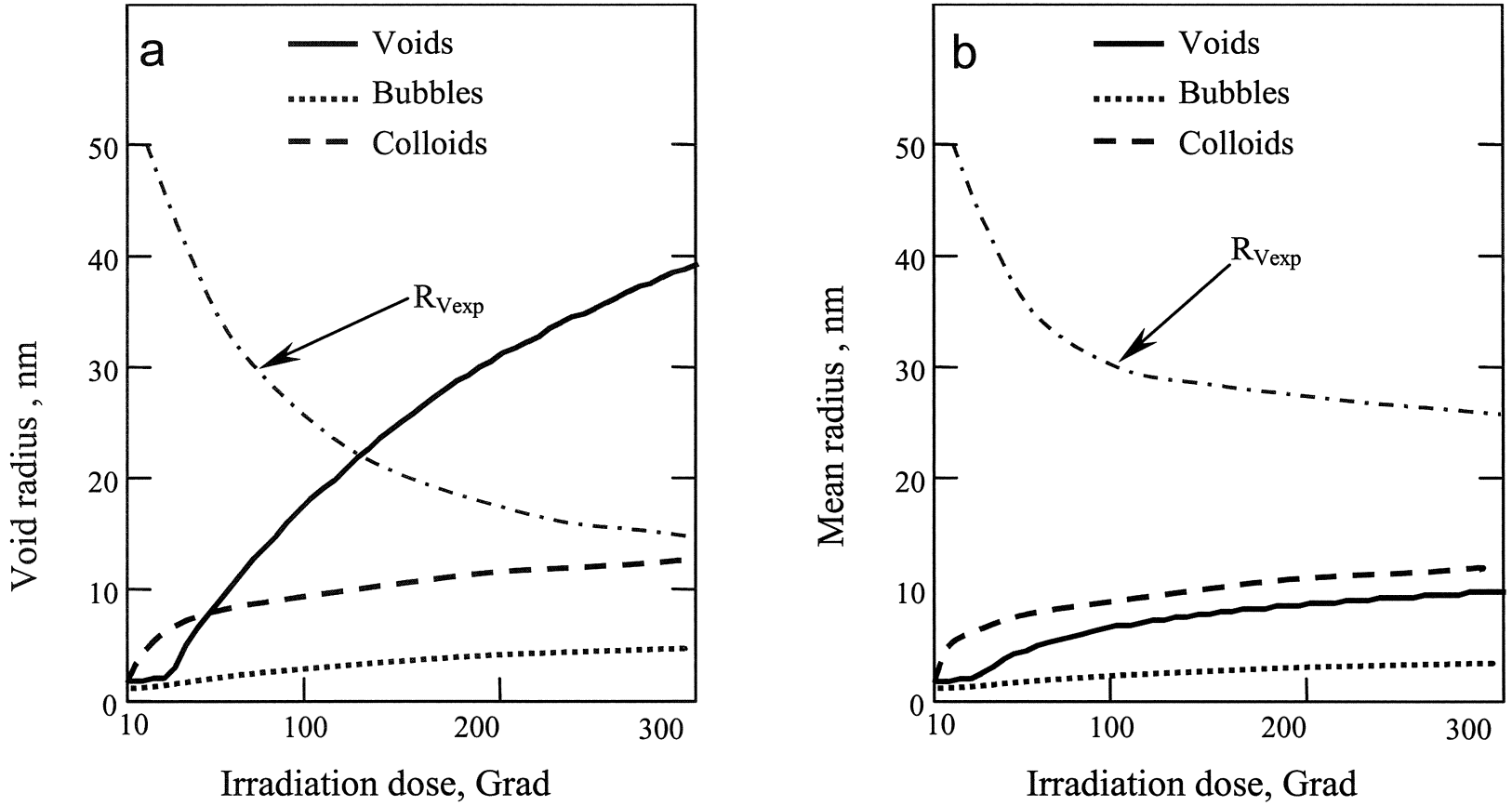

Figure 39. Dose dependence of the mean radii of voids and colloids at $K = K_1 = 240$ Mrad/h, and $T = 100^0$C calculated for two different values for the recombination efficiency of V_F and F centers at bubble surfaces, $Z_v^B = 10^{-5}$ (a) and $Z_v^B = 10^{-1}$ (b). The dislocation and bubble densities were assumed to be 5×10^{14} m^{-2} and 2×10^{23} m^{-3}, respectively. $R_{V\,exp}$ is the critical radius of collisions between gas-filled voids and colloids, which would bring the halogen gas and metal to a back reaction inside the voids.

3.2.1.10 Effects due to colloid structural state

When the radius reaches a threshold value R_C^{th}, the colloids lose their coherency. The value of R_C^{th} can be roughly estimated from the balance between the misfit energy gained in the process and the energy of the dislocation loop needed to compensate for the change of the colloid volume and the difference in surface energies of coherent and incoherent colloids, γ_{in} and γ_c:

$$R_C^{th} \approx \frac{\mu b \ln\left(8R_C^{th}/er_d\right)/2\pi(1-\nu)+2(\gamma_{in}-\gamma_c)}{\sigma_\varepsilon}, \tag{43}$$

where r_d is the dislocation core radius.

This change in structural state can strongly affect their subsequent evolution. On the one hand, the intrinsic misfit bias (that is due to the colloid/lattice parameter mismatch) disappears, which gives them a possibility to capture more V_F centers. On the other hand, incoherent colloids can trap both F and V_F centers, a subsequent recombination of which would produce a "free" space and, hence, a radiation-induced misfit instead of the intrinsic one. The maximum value of the radiation-induced misfit is determined by the ultimate misfit stress, which is controlled by the mechanism of punching of a vacancy loop that relieves the stress [32]. Accordingly, the maximum bias of incoherent colloids can be found to be as follows:

$$\delta_{in}(R_C) \approx \frac{\alpha_{in} b}{R_C}, \quad \alpha_{in} \equiv \alpha_c^{im} + \alpha^d\left(1-\frac{2\gamma_{in}}{\mu b}\right), \tag{44}$$

and their mean radius and volume fraction growth rates will change to

$$\frac{d\overline{R}_C}{dt} = \frac{\alpha_{in} b}{2\overline{R}_C^{\,2}} D_H \overline{c}_H \Theta(\delta_d - \delta_{in}). \tag{45}$$

$$\frac{dV_C}{dt} = D_H \overline{c}_H (\delta_d - \delta_C) \frac{k_C^2 k_d^2 \left(k_B^2 + k_i^2\right)}{k_C^2\left(k_d^2 + k_C^2 + k_V^2 + k_B^2 + k_i^2\right) + k_d^2\left(k_B^2 + k_i^2\right)} \tag{46}$$

Void effective bias (39) will be also changed to the following expression:

$$\delta_{VS}\left(k_S^2\right) = \delta_C + \frac{k_d^2\left(k_B^2 + k_i^2\right)(\delta_d - \delta_C)}{k_C^2\left(k_d^2 + k_C^2 + k_V^2 + k_B^2 + k_i^2\right) + k_d^2\left(k_B^2 + k_i^2\right)}. \tag{47}$$

What is more, the dislocation density will be increased due to the generation of dislocation loops by incoherent colloids [32]. The rate of dislocation density increase is proportional to the flux of V_F centers to colloids and can be expressed as follows:

$$\frac{d\rho_d}{dt} \approx \frac{8\sqrt{2\pi}}{3b} N_C D_v \bar{c}_v - \frac{\rho_d}{\tau_d}, \tag{48}$$

where τ_d is the rate of the dislocation structure recovery, which together with production rate determine a steady-state dislocation density.

This transition is expected to take place at very high irradiation doses, which have not yet been reached in a controlled experiment. So this question needs further experimental and theoretical investigations.

3.2.1.11 Temperature dependence of the damage production

The temperature dependence of the colloid evolution is governed by two parameters, namely, by the migration and formation energies of F centers. The former determines bulk recombination of F and H centers, which influences the product $D_H \bar{c}_H$ that enters all the growth rate expressions as a common factor. This factor increases with increasing temperature until the bulk recombination becomes negligible as compared to recombination at ED. The formation energy determines production of thermal F centers, which increases rapidly with increasing temperature and must be taken into account at high temperatures (or low dose rates) of irradiation. As it has been shown for irradiated metals [10], an account of thermal F centers results in an effective increase of the colloid bias factor parameter α_c^{im} by the value $\left(2\gamma\omega/kT\right)\left(D_F c_F^{(e)}/D_H \bar{c}_H\right)$, where

$$c_F^{(e)} = \exp\left(-E_F^f/kT\right) \tag{49}$$

is the thermal equilibrium concentration of F center and γ is the surface energy of particular ED. The colloid fraction growth rate can be shown to be proportional to the difference $D_H \bar{c}_H - D_F c_F^{(e)}$, which increases with temperature in the region of bulk recombination and decreases in the region of thermal PD domination. In the intermediate region, where both bulk recombination of PD and their thermal production are negligible, the growth rate per dpa reaches its maximum value, which is independent on the temperature and dose rate and is determined only by the sink strengths (the same is true for the void swelling rate in metals [10, 21, 22]). The result is shown in Fig. 40 both for our dose rate and for that assumed to model the nuclear waste repository irradiation. In both cases, we can see the usual bell shape temperature dependence shifting along the temperature axis with changing dose rate. The upper cut-off temperature is determined by the sum of the F center migration and formation energies, E_S.

The expressions for the critical parameters (33) and (34) remain unchanged but the form of the effective parameters γ_K and σ_K will be different due to the account of thermal PD [10, 11, 33]:

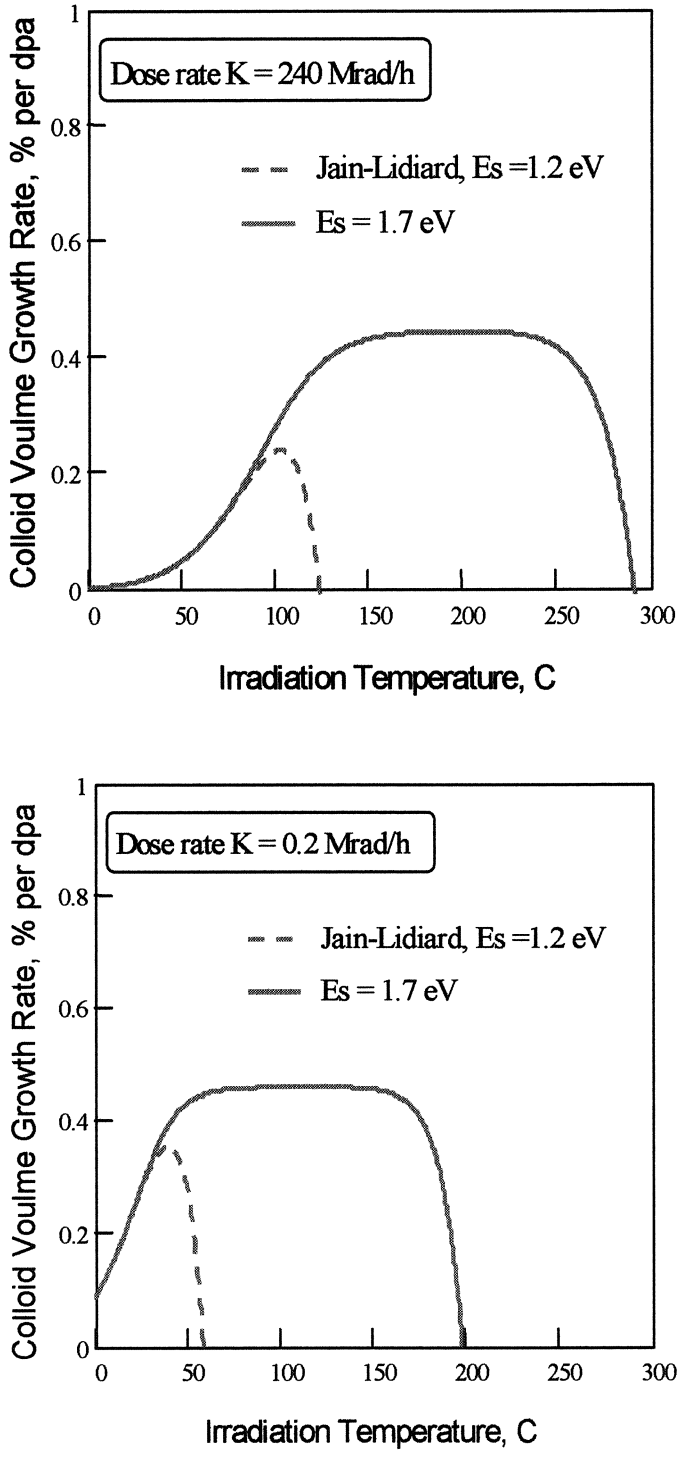

Figure 40. Temperature dependence of the colloid volume growth rate. Two dose rates are shown, corresponding to the laboratory irradiation (left) and irradiation in repository (right). In both cases, we can see the usual bell shape temperature dependence shifting along the temperature axis with changing dose rate. The upper temperature cut-off is determined by the sum of the F center formation and migration energies, E_s. We have used the parameters available from the literature, we may suggest that the rate of accumulation of stored energy per dpa in repository conditions is expected to be as high as in laboratory experiments.

$$\gamma_K = \gamma + \mu b \frac{\alpha^{im}}{2\alpha_K^d}, \qquad \sigma_K = \mu \frac{\bar{\delta}}{\alpha_K^d}, \qquad \alpha_K^d \equiv \alpha^d + \frac{D_F c_F^{(e)}}{D_H \bar{c}_H} \frac{\omega\mu}{kT} \tag{50}$$

The voids are thermally more stable as compared to colloids since their dissolution is determined by the sum of the F and V_F center migration and formation energies. Accordingly, the annealing behavior of irradiated *NaCl* after irradiation can be understood as the dissolution of colloids at moderate temperatures (between 250 ^{O}C and 400 ^{O}C [34]). This results in a back reaction of liberated F centers ("evaporated" excess Na from the colloids) with halogen molecules in bubbles, which leaves behind vacancy voids and dislocations that could be annealed only at higher temperatures (above 400 ^{O}C to 450 ^{O}C [34]). So a moderately annealed crystal still persists in showing a lower density (i.e. a volume expansion) than an unirradiated crystal up to 400^{O}C. We predict with this model that a subsequent irradiation of this not fully recovered crystal at lower temperatures may result in further void development instead of colloid formation that would be suppressed by voids. Such a result can be expected, however, after sufficiently long irradiation to produce halogen bubbles with sizes exceeding the critical void size, which corresponds to the critical number of vacancy pairs, n_{Vcrit}, in fig. 34. Below this size, empty voids formed as a result of annealing would have a larger bias for H enters than that of dislocations. Such voids would be filled with halogen under the subsequent irradiation and provide an additional driving force for the colloid growth instead of suppressing it.

The critical void size is determined by the ratio of its bias constant to the dislocation bias to be about 1.7 nm. The mean bubble size can reach this value after irradiation dose of about 40 Grad (which is even higher than the dose 30 Grad required for the bubble-void transition onset). So the annealing up to 400 ^{O}C should enhance (or suppress) the colloid production under a subsequent irradiation if the initial dose were lower (or higher) than 40 Grad. The former conclusion agrees with experimental data by Hodgson et al. [34] who observed that such a treatment enhanced the colloid production after initial irradiation up to 5 Grad and suggested that vacancy pairs and/or their clusters were responsible for colloid nucleation. Experimental data on the effect of annealing after higher irradiation doses do not exist to our knowledge.

3.2.1.12 Discussion of the results and comparison with experimental data

The present theory is based on a new mechanism of dislocation climb, which involves the production of V_F centers (self-trapped hole neighboring a cation vacancy) as a result of the absorption of H centers. There exist a lot of experimental data on cation vacancy production in alkali halides under irradiation (see, e.g. [34, 35]) and on the formation of vacancy pairs and their small aggregates [36]. The salient points of the present model are compared with those of the Jain-Lidiard model in fig. 41.

Based on the present model, a complete set of the rate equations for PD and growth rates for ED was derived. An asymptotic (in time of irradiation) solution to these equations was obtained in the temperature range, in which both anion and cation PD are mobile. In this region, the growth or shrinkage rates of different kinds of ED and their sizes are determined

by the difference between the incoming fluxes of radiation-induced PD, which is determined by several material constants presented in Table 1. We have used a typical value for the mean dislocation density, $\rho_d = 10^{14}$ m^{-2}, as the only input microstructural parameter, and two values for the recombination efficiency of V_F and F centers at bubble surfaces, Z_v^B, 10^{-5} and 10^{-1}. The first value has been deduced from a comparison with the observed void number density in KBF_4 doped samples.

To make a quantitative comparison of the other calculated ED parameters with experimental data we have to take into account that they have been obtained at different temperatures ranging from 60 to 130 ^{0}C. In this range, as can be seen from fig. 40, the temperature dependence of ED evolution is due to F center increasing mobility since their thermal production is negligibly small as compared to that by irradiation.

Figure 42a shows the calculated and measured dose dependencies of the sodium latent heat of melting (LHM) at 100 ^{O}C. LHM is proportional to the colloid volume fraction, which can be seen to correlate with void parameters in Fig. 42b-d measured at temperatures ranging from 60 to 130 ^{0}C. The experimental data for voids in *NaCl* doped with KBF_4 (illustrated also in Fig. 20) seem to be in agreement with the calculations.

There appears to be no saturation of colloid growth with increasing irradiation dose, and besides, the void dimensions grow to exceed the mean distance, first, between bubbles and then between colloids (R_{expl} in Fig. 39a) resulting in their collisions with voids. Collisions with bubbles fill the voids with gas, and subsequent collisions with colloids bring the halogen gas and metal to a back reaction inside the voids. Such a sudden release of stored energy can be shown to result in a drastic rise of temperature (above 10^4 K) and gas pressure (up to several GPa) within voids, which may transform equiaxial voids into penny shaped cracks along the cleavage planes in the matrix, as it will be demonstrated in section 3.3. Figs. 22 and 28 show penny shaped voids/cracks in natural rock salt samples and in *NaCl* doped with *K* as compared to equiaxial voids formed in heavily irradiated *NaCl* doped with KBF_4 (Fig. 20). Obviously, the dimensions of penny shaped voids should be larger than those calculated in the framework of diffusion void growth mechanism. This explains the discrepancy between theoretical curves and experimental data presented for other dopants in fig. 42. To describe these data we have developed a new (explosion driven) mechanism of void/crack growth in irradiated *NaCl* resulting in a subsequent material destruction, which is presented below in section 3.3.

In the following section we consider the possible ways to model the impurity effects on void formation

3.2.2 Impurity effects on void formation

Most of the impurities studied in the present project enhance the void production as compared to that in pure material, as shown in figs. 43 and 44. The only exception from this rule seems to be bromine, which results also in suppression of colloid production (see section 3.3.2 below).

Jain-Lidiard	***Dubinko-Turkin-Vainshtein-den Hartog***
Clustering of H-centers to form self-interstitial (sia)-loops and *molecular centers*	Clustering of *H*-centers to form ***Halogen bubbles*** and a SIA-loops
Bias-driven growth of SIA-loops followed by generation of immobile ***molecular centers***, H_2V: $H+H+SIAloop\{n\}\rightarrow SIAloop\{n+1\}+H_2V$	Bias-driven growth of SIA-loops followed by generation of *mobile* V_F***-centers*** (*cation vacancy with a trapped hole):* $H+SIAloop\{n\}\rightarrow SIAloop\{n+1\}+V_F$
Dislocations are biased toward absorption of H-centers. Metallic colloids are assumed to be neutral sinks	All extended defects are biased toward absorption of *H*-centers. Competition between bias factors controls the evolution of microstructure
Growth of colloids due to absorption of excess *F*-centers: $F+Colloid\{n\}\rightarrow Colloid\{n+1\}$	Growth of colloids due to absorption of excess *F*-centers. No absorption of V_F***-centers*** by coherent colloids
Accumulation of dispersed ***molecular centers***	Accumulation of molecules in bubbles up to a critical value
	Transition of overcritical bubbles to voids: $Bubble\{n^*_{Gas},n_{Vac}\}+V_F+F\rightarrow Bubble\{n^*_{Gas},n_{Vac}+1\}\rightarrow .....Void$
Recombination of *molecular centers* with *F*-centers, which **suppresses** colloid growth.	Void growth due to absorption of V_F-centers and excess *F*-centers
	Collision of growing voids with *Hal*-bubbles and colloids resulting in **explosive *Me+Hal* reaction**, which increases the gas pressure in voids beyond the strength limit of material

Figure 41. Comparison of the models of radiation damage in alkali halides

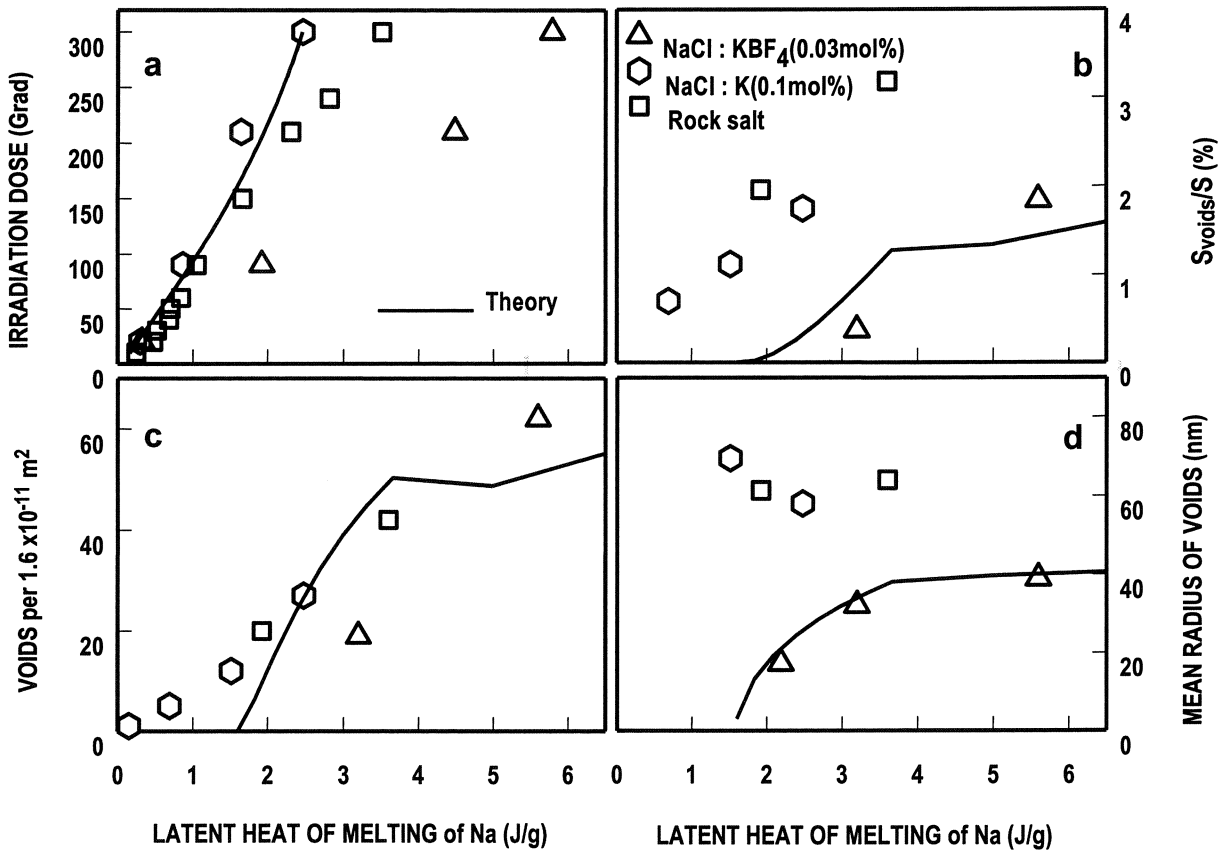

Figure 42. Comparison between experiment and the present theory.

a) Measured and calculated dependence of LHM of metallic *Na* , which is proportional to the colloid fraction, on irradiation dose ($K = K_I$) at 100 ^{0}C.

(b-d) Void mean parameters (volume fraction (b), number density (c) and mean radius (d)) against LHM measured after irradiation up to 300 Grad (symbols) for different dopants and temperatures (from 60 ^{0}C to 130 ^{0}C) and calculated (curves) assuming $K = K_I$, dislocation density $\rho_d = 10^{14}$ m^{-2}, and the void formation rate $dN_V/dKt = 2\text{x}10^{17}$ Grad^{-1}m^{-3} [11].

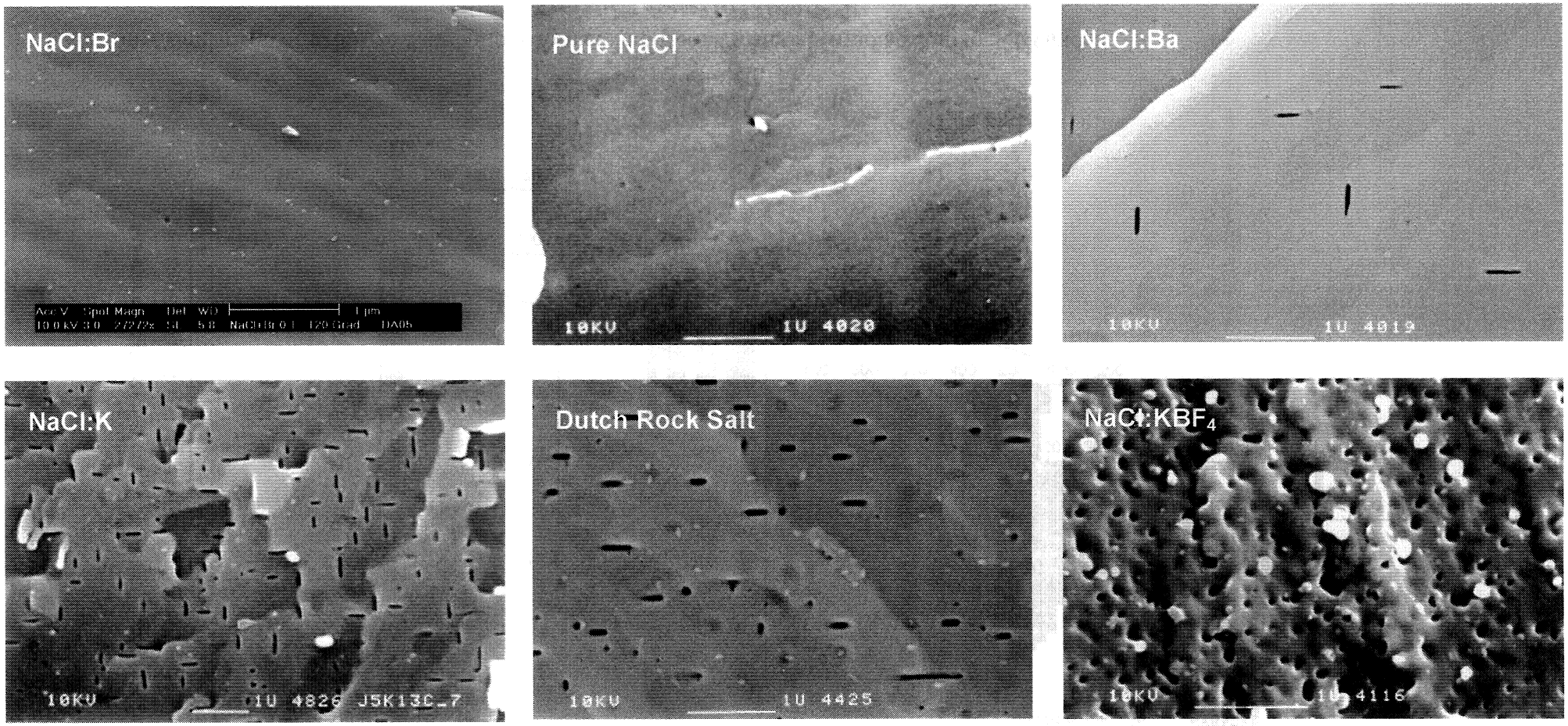

Figure 43. Comparison of void structures formed in different materials irradiated up to 300 Grad.

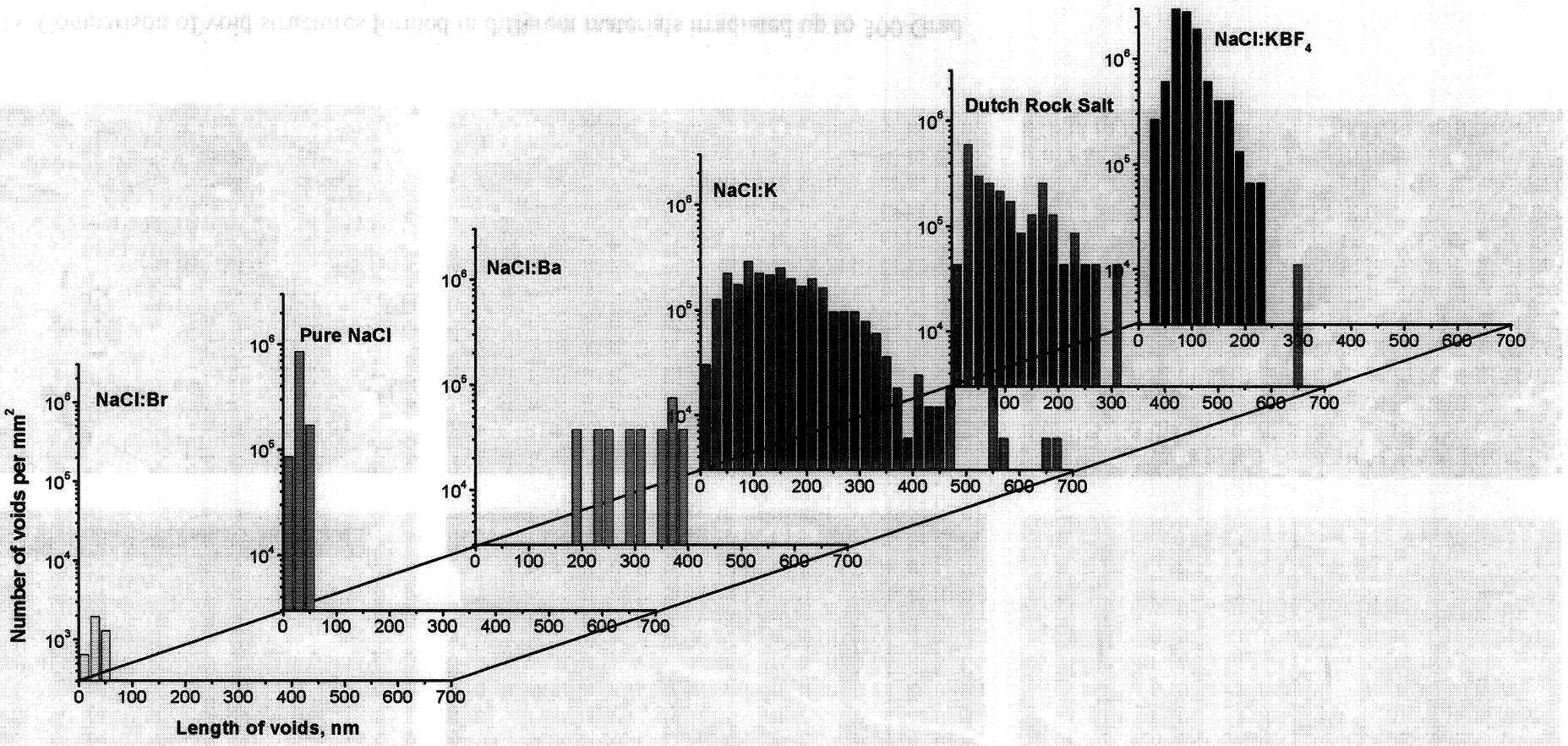

Figure 44. Comparison of void size distributions formed in different materials irradiated up to 300 Grad.

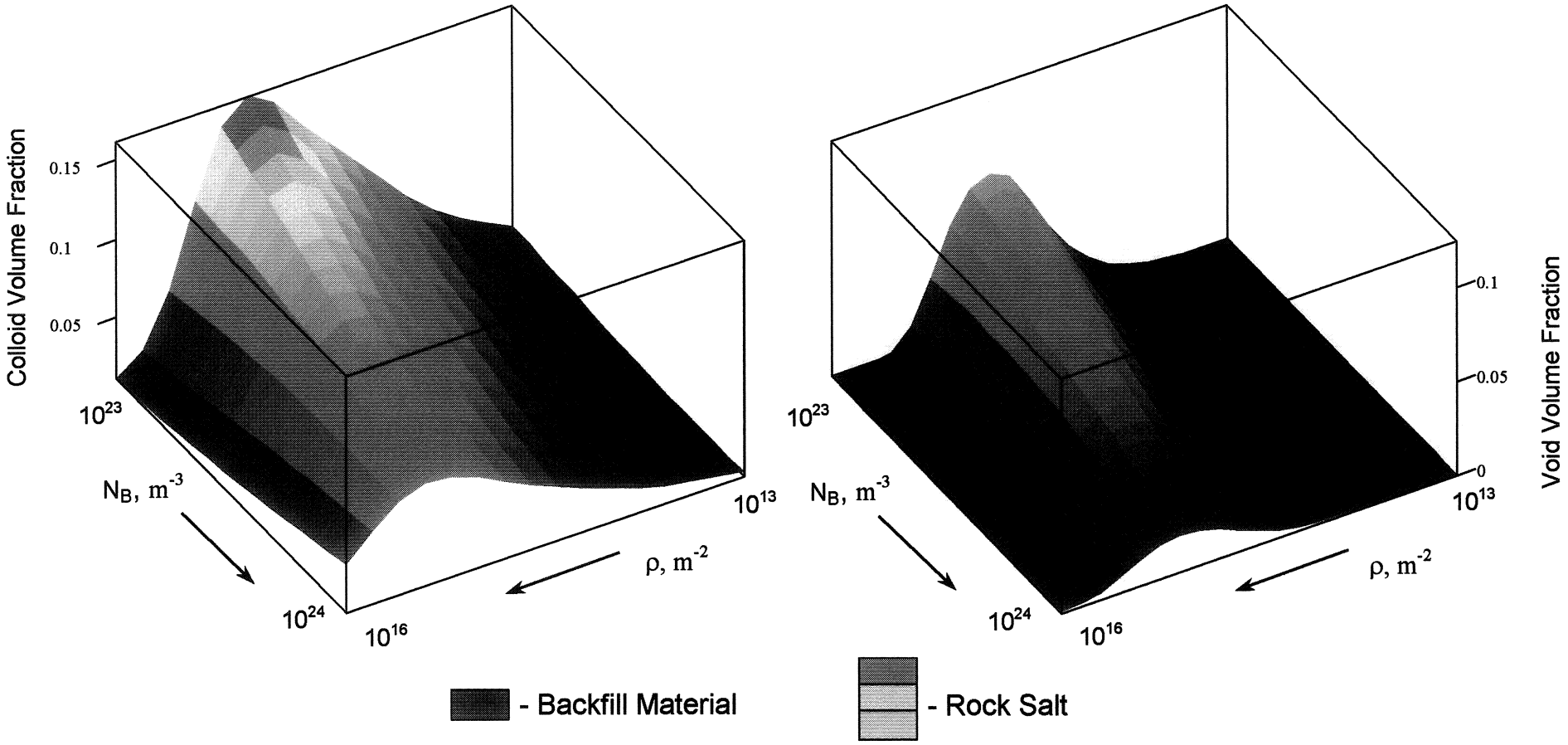

Figure 45. Volume fractions of colloids and voids after irradiation to 300 Grad calculated for different dislocation and bubble densities at $Z_v^B = 10^{-5}$. It is seen that low dislocation density and high bubble density suppress both the void and colloid formation, which makes the material more radiation resistant.

There are many ways in which impurities can affect the formation of radiation damage. One of the most obvious ways is that impurity atoms can be nucleation centers for extended defects under irradiation, if they trap certain types of mobile point defects. If, for example, they can trap H centers, that would probably increase the dislocation density, ρ, and the bubble number density, N_B, which enter our model as free parameters (colloid and void number densities are calculated). The impurity-induced difference in dislocation and bubble densities can be one of the reasons for the different responses of doped materials to irradiation. This is demonstrated in Fig. 45, which shows the void volume fraction calculated at different dislocation and bubble densities.

3.3 Goal 2: Smart backfill materials

We have demonstrated above that formation of voids strongly depends on impurity content, which may be explained either by a direct impurity effect on the bubble-void transition or via the impurity influence on the number densities of other extended defects such as dislocations and bubbles. In this section we will show how voids can affect the structural stability of rock salt under irradiation, which is necessary in order to select the particular dopants that ensure the optimal radiation resistance of backfill materials.

3.3.1 Structural stability of rock salt under irradiation

According to the present model, chlorine bubbles (several nm in size) are the most finely dispersed ED in the system (the inter-bubble spacing is typically well below 10 nm) so that they start to collide with growing voids first, filling them with chlorine gas (fig. 46) The chlorine molecules within the "bubbles" are in a solid or liquid state due to a super high pressure (in the GPa range), but after collision with a void it becomes a gas. One can estimate the number of chlorine atoms, n_{Cl}, captured by a void of radius R_V as a product of the void volume and the bubble volume fraction, V_B, divided by the chlorine atomic volume, ω_{Cl} :

$$n_{Cl} = \frac{4\pi}{3} R_V^3 \frac{V_B}{\omega_{Cl}} \tag{51}$$

The bubble volume fraction grows with irradiation dose at the same rate as the colloid volume fraction, $V_C = \frac{\omega}{\omega_{Cl}} V_B$, due to the balance between sodium and chlorine atoms stored in the unit volume of the matrix, where ω is the atomic volume of *NaCl*. Accordingly, the gas pressure in the voids (where it is in molecular form) is also determined by the colloid volume fraction:

$$P = \frac{(n_{Cl}/2)kT}{(4\pi/3)R_V^3} = \frac{kT}{2\omega_{Cl}} V_B = \frac{kT}{2\omega} V_C, \tag{52}$$

where we have used the equation of state of an ideal gas, which is valid in this pressure region. An estimate done for 100 ^{0}C shows that even at maximum values of $V_C \approx 10\%$, the pressure is 5x10^{-3} Gpa (50 *atm*), which is still lower than the surface tension of a void as large as 200 nm. So this pressure does not affect the void bias, which controls the void diffusion growth. However, the chlorine accumulation in voids provides a very important possibility for the explosive back reaction with metallic sodium when a growing void hits the first colloid.

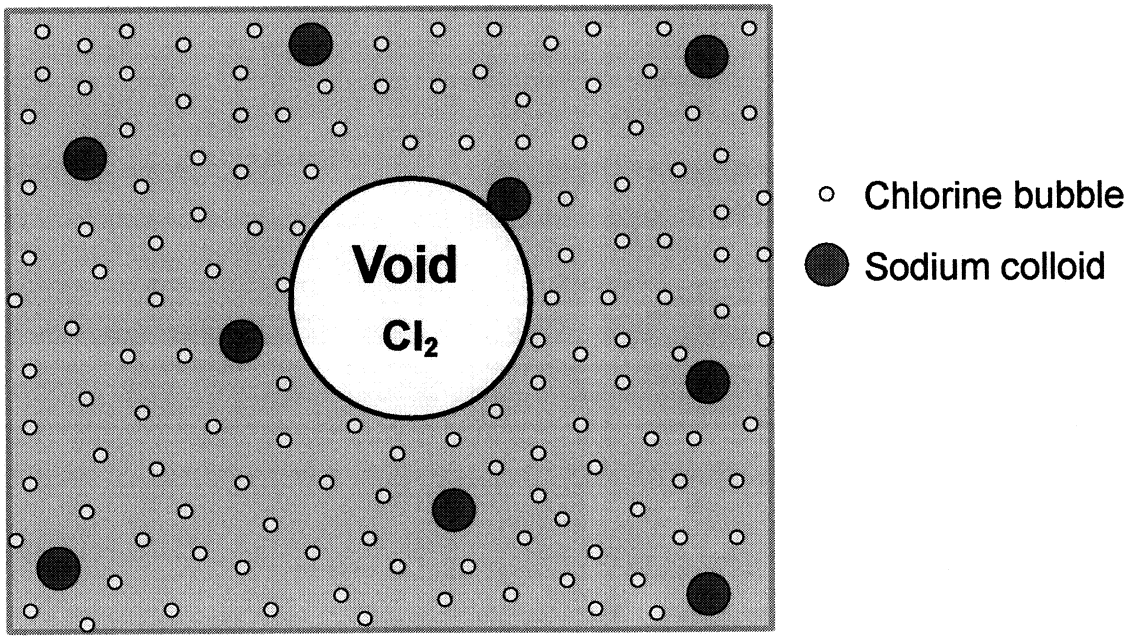

Figure 46. Illustration of the distribution of chlorine bubbles, sodium colloids and voids in irradiated NaCl crystals. The void size is about the mean inter-colloid size, R_{Vexp}, when the first collision with a colloid is expected.

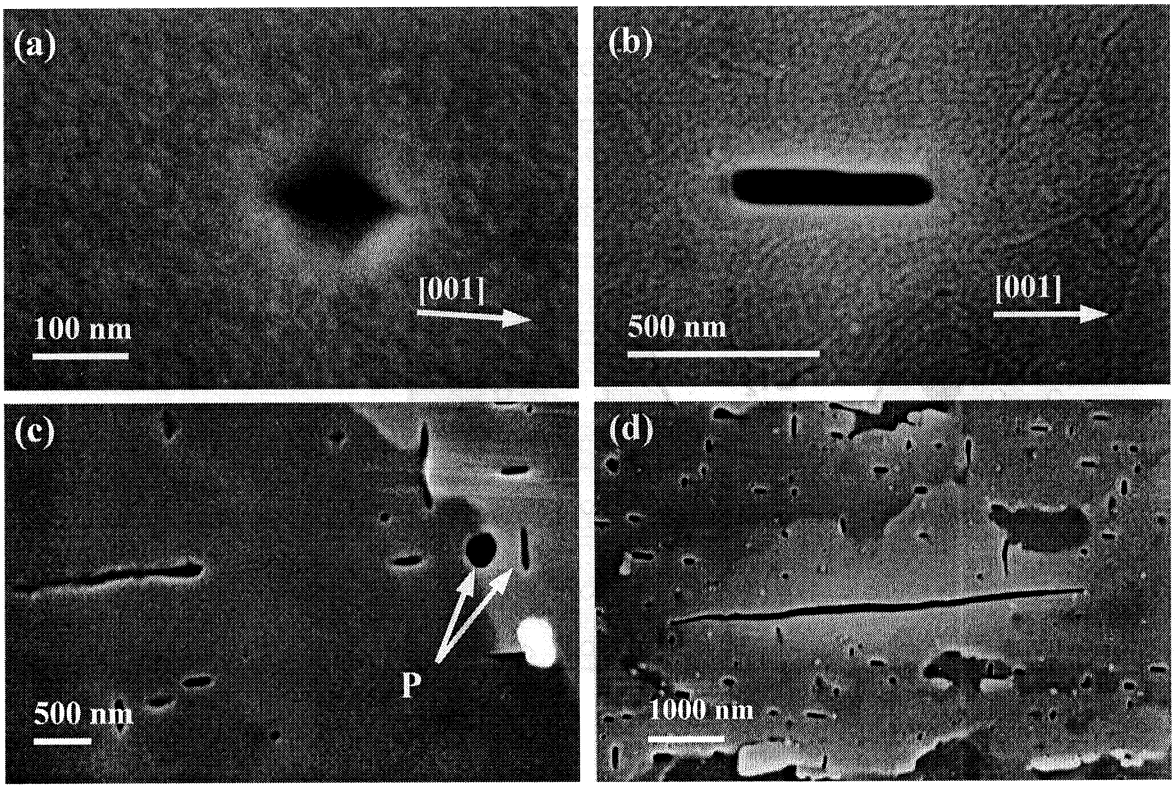

Figure. 47. SEM micrographs showing vacancy voids and cracks in natural rock salt crystals irradiated with 0.5 MeV electrons. (**a**) Equiaxial void at high resolution after irradiation to 60 Grad; latent heat of melting (LHM) of metallic *Na* is 0.45 J/g. (**b**) "Penny-shaped" crack formed after irradiation to 300 Grad, LHM of metallic *Na* is 0.8 J/g (**c**) "Penny-shaped" voids/cracks in natural rock salt irradiated up to 300 Grad; LHM of metallic *Na* is 1.2 J/g. Two adjacent voids with different orientations are shown by the letter "P" with the arrows. (**d**) Long crack formed after irradiation to 300 Grad, LHM of metallic *Na* is 2.5 J/g.

The amount of released energy in this reaction is proportional to the energy released due to formation of one *NaCl* molecule, q_{NaCl}, and to the number of molecules formed as a result of collision, n_{NaCl}. The latter is equal to the mean number of sodium atoms in a colloid, which is close to the number of chlorine atoms accumulated in the void at the time of the collision (Fig. 46). The released energy heats up the reaction products inside the void resulting in an instantaneous temperature and pressure increase, which can be estimated as

$$\Delta T = \frac{q_{NaCl} n_{NaCl}}{C_P n_{NaCl}} = \left| C_P = \frac{3}{2}k \right| = \frac{2}{3}\frac{q_{NaCl}}{k} \geq 2\times 10^4 K \tag{53}$$

$$\Delta P = \frac{n_{NaCl} k \Delta T}{\frac{4\pi}{3} R_V^3} = \left| n_{NaCl} = \frac{4\pi}{3} R_V^3 \frac{V_C}{\omega} \right| \geq \frac{2}{3}\frac{q_{NaCl}}{\omega} V_C \approx \mu V_C \tag{54}$$

where C_P is the specific heat capacity of *NaCl* per molecule estimated as that for ideal gas. We note that the calculated temperature increase in eq. (53) has been obtained under the assumption that there is no exchange of heat between the hot gas within the void and the surrounding crystal lattice, which has a relatively high heat capacitance as compared to the hot gas. This conclusion has been drawn after a detailed discussion about this subject with H.J. de Haan (CORA committee). The actual temperature increase will therefore be smaller than the one presented in eq. (53). Our preliminary conclusion is still, that the temperature of the hot gas will be very high and the proposed mechanism is the most likely explanation for the observation of elongated cracks in heavily irradiated rock salt. In order to obtain an accurate value for the temperature increase complex calculations should be carried out. One should take into account realistic reaction rates between Na and Cl within the voids, the shape of the initial voids (approximately spherical) and furthermore realistic relaxation times for the heat exchange with the surrounding lattice have to be obtained. These relaxation rates cannot be derived from the standard thermodynamic relationships, because we are dealing with extremely short time scales, which are in the vicinity of the characteristic times of phonons in the surrounding NaCl lattice. As a result the exchange of heat between the gas within the voids and the NaCl lattice needs more time than expected on the basis of thermodynamics.

The pressure increase due to the back reaction is proportional to the colloid volume fraction or, equivalently, to the amount of stored energy per unit volume. The proportionality coefficient is close to the matrix shear modulus μ, which is about 12 Gpa in *NaCl*, which gives one the pressure in the GPa range for the observed values of stored energy. Such an increase of pressure may initiate a crack propagation from the void along the matrix cleavage plane (100) if it is bigger than some threshold value [37]: $P_f = \sigma_f / 2$, where σ_f is the fracture stress corresponding to the Griffith crack of the length, L:

$$\sigma_f = \sqrt{\frac{EG_c}{\pi(1-\nu^2)L}} \tag{55}$$

where E is the Youngs modulus and G_c is the total work of fracture. The initial crack length in eq. (55) is about the void size, $2R_V$, which allows us to express the threshold colloid volume fraction, V_{th}, required to initiate the explosive crack propagation through the void size:

$$V_{th} = \frac{5\omega}{4q_{NaCl}}\sigma_f \propto R_V^{-1/2}. \qquad (56)$$

The pressure in the growing crack decreases due to its expansion, which restricts the crack propagation distance and results in the transition of an equiaxial void into a penny-shaped crack. This is illustrated in Figs. 47, 43, 28 and 22 showing the void-crack evolution with increasing irradiation dose and the amount of stored energy in crystals with different dopants. It is seen that the crack length increases gradually, which can be explained by a combined mechanism of diffusion accumulation and explosive release of energy in voids and cracks (see section 3.4.1 below).

Thus, the structural stability of NaCl under irradiation is determined both by the amount of stored energy (measured via colloid volume fraction) and the void size distribution. In the next section we will show how the stored energy accumulation depends on the irradiation parameters and impurity content.

3.3.1 Effects of the temperature, dose rate and impurities on the stored energy accumulation

The intensity of our laboratory irradiation is several orders of magnitude higher than that expected under repository conditions, which poses a very important problem of the dose rate effects. From a theoretical point of view we know that irradiation conditions are controlled by two parameters, namely, dose rate, K, and temperature, T, which means that equivalent irradiation conditions can be achieved at different dose rates by adjusting irradiation temperature.

The temperature dependence of the colloid evolution is governed by two parameters, namely, by the migration and formation energies of F centers. The former determines the bulk recombination of F and H centers, which decreases with increasing temperature until it becomes negligible as compared to the recombination at extended defects. The formation energy determines the concentration of thermal F centers, which increases rapidly with increasing temperature and must be taken into account at high irradiation temperatures (or low dose rates). The steady-state colloid volume growth rate is roughly proportional to the difference between the radiation-induced and the thermal concentration of F centers, which increases with the temperature in the region of bulk recombination and decreases in the region of thermal point defect domination. In the intermediate region, where both bulk recombination of point defects and their thermal production are negligible, the growth rate per dpa reaches its maximum value, which does not depend on the temperature and dose rate and is determined only by the sink strengths. The result is shown in Fig. 40 both for the laboratory dose rate and for that assumed to model the radwaste repository irradiation. In both cases, we can see the usual bell shape temperature dependence shifting along the temperature axis with changing dose rate. The upper temperature cut-off is determined by the sum of the F center formation and migration energies. We need reliable information on these parameters. Adopting the parameters available from the literature (Table 1), the model indicates that the rate of accumulation of stored energy per dpa in repository conditions is expected to be as

high as in the laboratory experiments. We should be very careful with this (preliminary) conclusion, because we know that the detailed behavior of the radiation damage formation depends sensitively on the specific choices of the relevant parameters.

As far as the impurity effects are concerned, the impurity-induced difference in dislocation density can be one of the reasons for the different responses of doped materials to irradiation. This is demonstrated in Fig. 48 by comparing theoretical results obtained for dose dependence of the colloid volume fraction for different dislocation densities with experimental data obtained in crystals doped with different impurities.

It can be seen that in most cases the volume fraction of the Na colloids increases almost linearly with the irradiation dose and does not show any sign of saturation even at very high irradiation doses. Only samples doped with Ba or Br do show some indication of saturation, but this type of behavior appears to be limited to only a few special cases. Saturation is definitely not observed as a general trend, as was concluded by previous investigators [2, 3]. But even if the volume of the colloid fraction saturates, this does not guarantee that the material is resistant against structural and mechanical instability, as will be demonstrated in the following section.

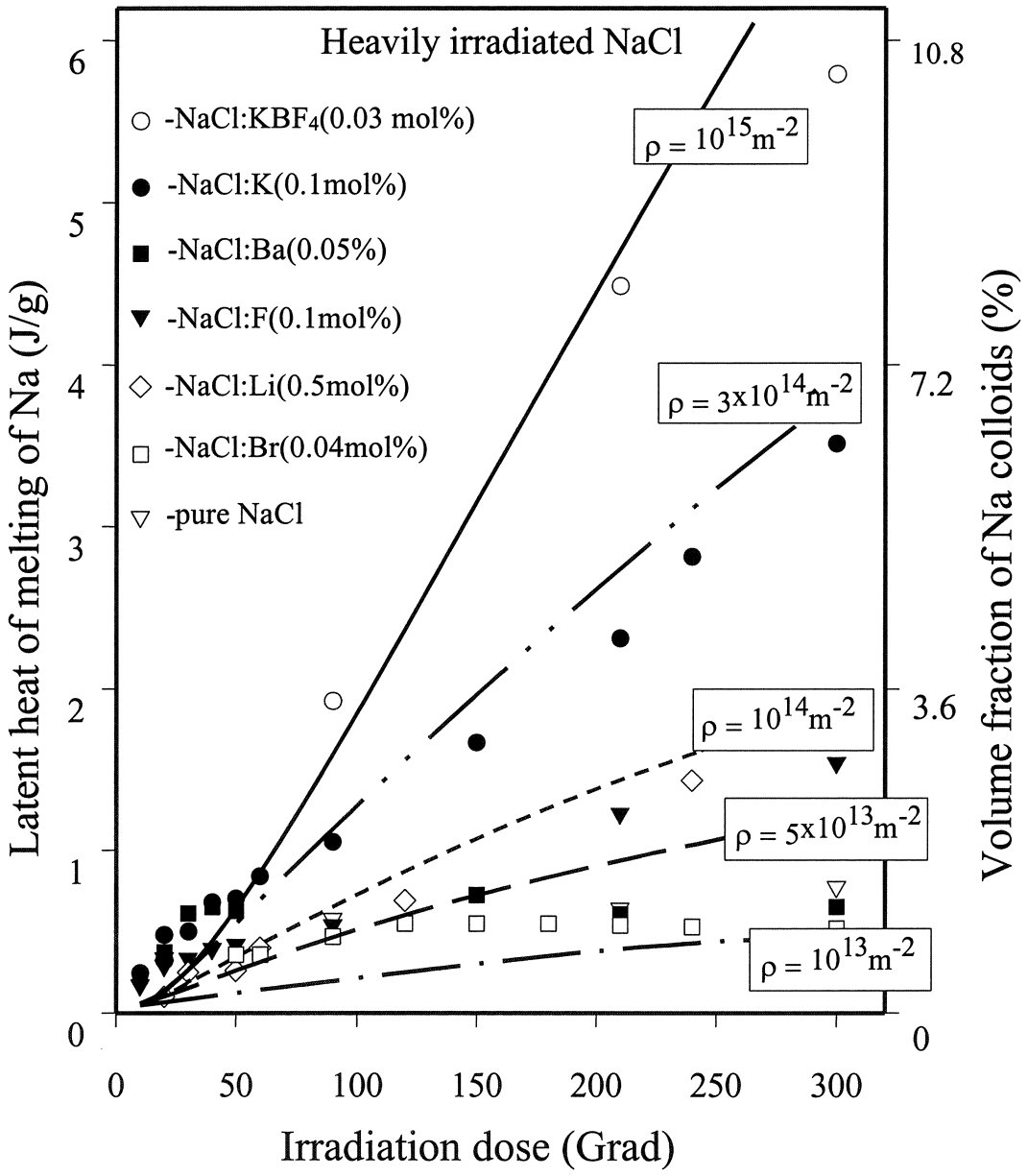

Fig. 48. Comparison of experimental data on dose dependence of colloid volume fraction (proportional to the LHM of Na) in crystals doped with different impurities and irradiated at 100 ^{O}C, 240 Mrad/h with theoretical results obtained for different dislocation densities.

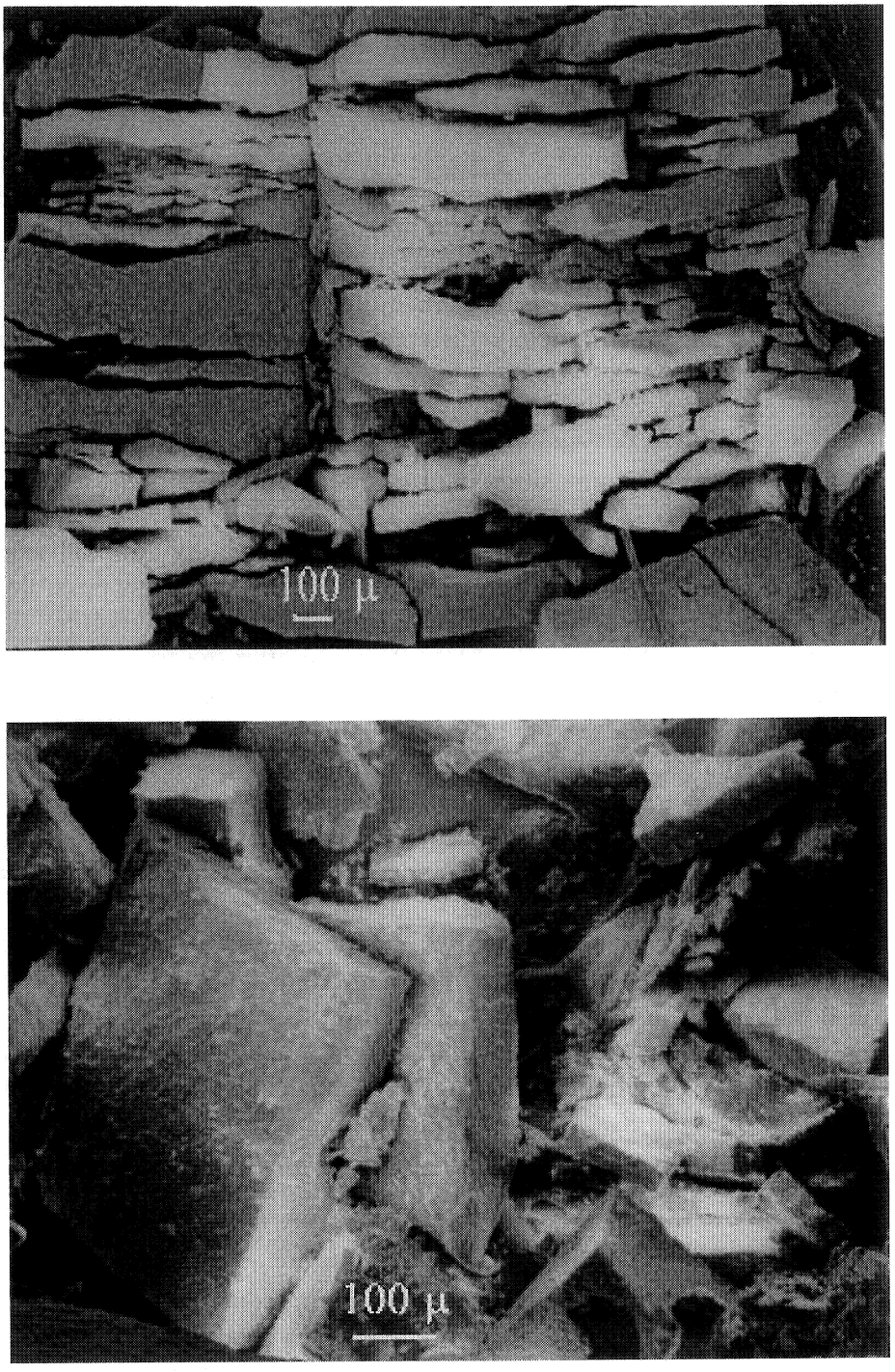

Figure 49. Explosive fracture of NaCl+K (0.1mol%) samples irradiated with 0.5 MeV electrons to 300 Grad. SEM micrograph of the exploded sample reveals large fragments and dust-like particles.

3.3.2 Impurity effects on mechanical stability of NaCl

SEM examinations have revealed that the response of the samples doped with Ba or Br is quite different (Fig. 43). The latter samples show very few small voids, and we have found that these materials remain mechanically stable up to the highest dose reached so far. In contrast with this, in Ba doped samples large penny-shaped cracks are formed, and many of the samples showed extensive fractures during the late stages of the irradiation experiments. Doping with K has a very strong effect on the development of radiation induced cracks (Figs. 43 and 28). In fact heavily irradiated NaCl:K is quite unstable and many samples exploded during the irradiation run. A completely different behavior has been observed for NaCl samples doped with small concentrations (a few 100 ppm) KBF_4 (Figs. 43 and 20). In these samples it was difficult to produce penny-shaped cracks, and it appeared that the stability of KBF_4-doped NaCl samples was quite high, i.e. even at the highest damage levels it was difficult to initiate explosive decomposition during irradiation.

The explosive fracture of irradiated samples can be also induced by their subsequent heating to temperatures of about 200^0C as shown in the Fig. 49. In this case, it is possible to carefully control the amount of stored energy by measuring the latent heat of melting (LHM) of *Na* before and after the fracture (Fig.50). The LHM decrease after the fracture confirms that the latter was indeed due to the release of radiation-induced stored energy.

Comparison of Figs. 20 and 28 shows that the critical amount of stored energy initiating the formation of penny-shaped cracks is substantially higher in crystals doped with KBF_4 than in those dopes with potassium. According to eq. (56), the critical amount of stored energy decreases with increasing void size as shown in Fig. 48, which is in agreement with experimental data shown in the same figure. Voids in crystals doped with KBF_4 are smaller and more numerous than in those doped with *K*, which delays their transition to cracks to a higher level of stored energy. Note that the maximum void size, R_{expl} does not increase with the irradiation dose since it is determined roughly by the inter-colloid spacing. Indeed, the explosions that do not result in the void-crack transition (below the curve in Fig. 51) result in the void shrinkage due to the condensation of *NaCl* molecules at the void surface after the cooling down of the spike. So R_{expl} is a point of accumulation of voids in the size space until the critical amount of stored energy is reached, which depends on the kinetics of colloid formation affected by the dopants.

In this section, we will conclude that among all the dopants investigated so far Br appears to the most promising for backfill materials since it results in reduction of both colloid and void production even as compared to pure NaCl. The mechanical stability of NaCl:Br is also high since it was not possible to initiate explosive decomposition during either irradiation or heating. But since the irradiation dose was limited to 300Grad, one cannot be sure of radiation stability of any investigated material in the higher dose range.

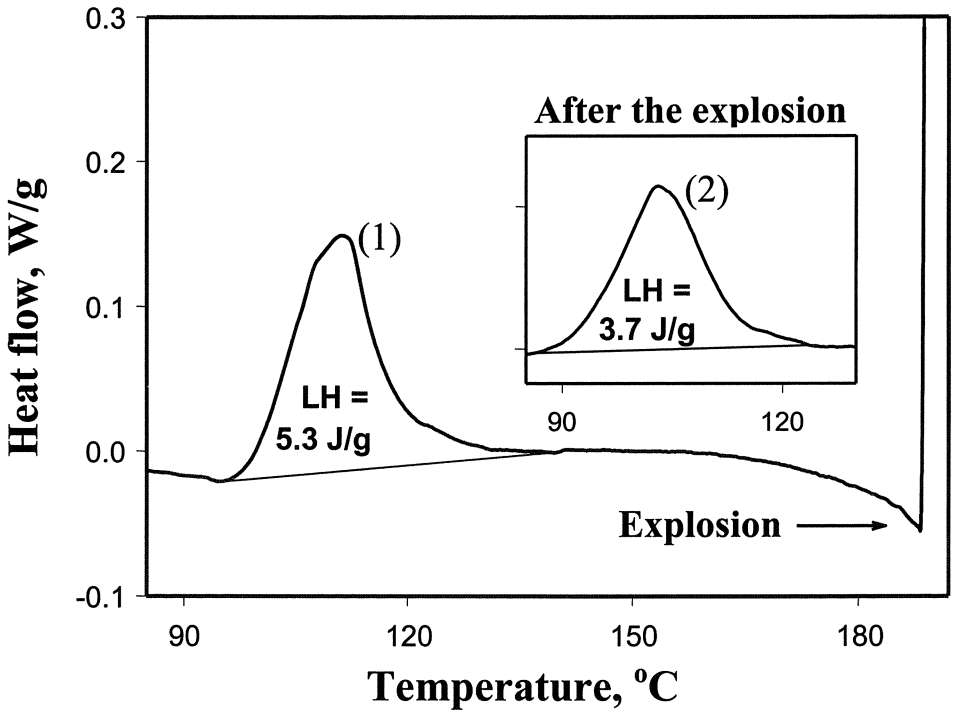

Figure 50. Differential scanning calorimetry (DSC) measurements of the LHM of metallic *Na* in NaCl:K before (1) and after (2) the explosion at 189 ^{0}C. The LHM has decreased by 30% due to the back reaction.

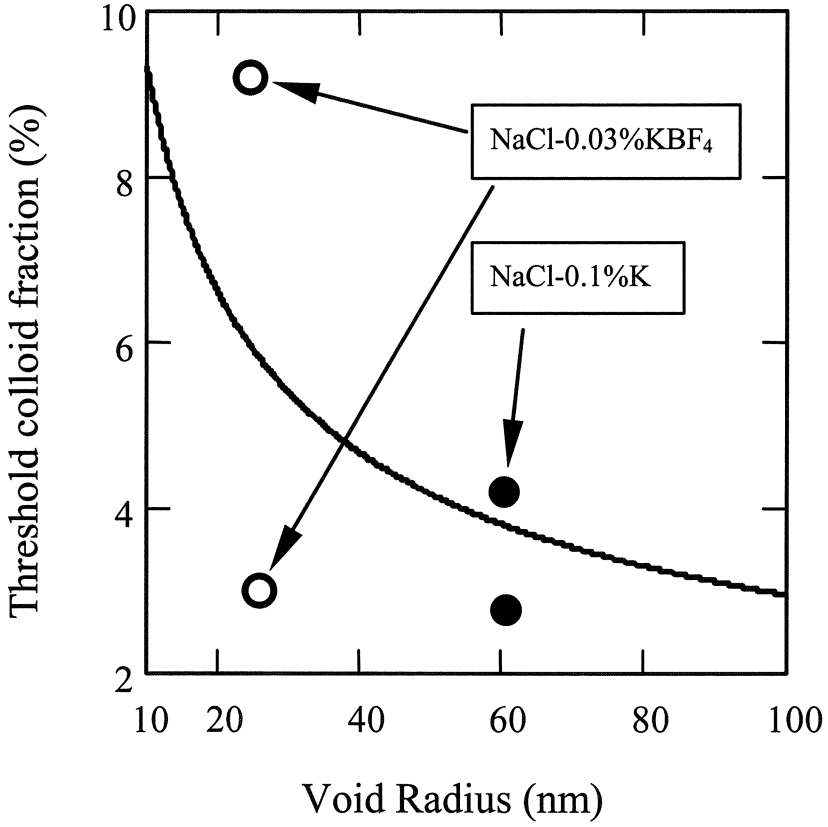

Figure 51. Threshold colloid volume fraction, V_{th} (56), required to initiate the explosive crack propagation versus the void radius. Experimental points below the theoretical curve correspond to the equiaxial voids before the void-crack transition while those above the curve correspond to the equiaxial voids after the void-crack transition.

3.4 Goal 3:Relation with future monitoring of storage sites

In the following section we will describe diffusion plus the explosion mechanism of the void-crack transition in more details and demonstrate the potential threats, which should be monitored under storage conditions.

3.4.1 Diffusion plus explosion mechanism of void-crack transition

As was demonstrated above, the instantaneous pressure increase in a chlorine-filled void due to its collision with a sodium colloid is proportional to the colloid volume fraction and is given by eq. (54). If the pressure exceeds the threshold value, $P_f = \sigma_f/2$, given by eq. (55), it will initiate a penny shape crack propagation along a cleavage plane, the length of which, L_{cr}, is determined by two competing processes.

The first one is the crack expansion in thickness due to gas pressure, which is a plastic process resulting in the pressure decrease by a factor proportional to the surface covered by the propagating crack and its thickness, T_{cr}. As a result, the crack propagation would stop if the gas pressure falls down to the threshold value. However, the pressure may not fall due to collisions with new bubbles and colloids lying along the cleavage plane in the layer of thickness T_{tip} determined by the collision efficiency of the crack tip. This process provides the crack with more "fuel", which stimulates its propagation increasing the pressure by a factor proportional to the surface covered by the propagating crack tip and its collision efficiency, $S_{cr} \times T_{cr}$, where S_{cr} is the crack surface.

A penny shaped crack can be described by a cylindrical layer with thickness T_{cr} and outer radius L_{cr}+R_{expl} , where R_{expl} is the void explosion radius determined by the colloid number density, N_C and mean radius, R_C, as

$$R_{expl} = \left(\frac{3}{4\pi N_C}\right)^{1/3} - R_C \tag{57}$$

Accordingly, the final pressure in the crack has the following dependence on its length and colloid parameters:

$$P\left(V_C, R_{expl}, L_{cr}\right) = \frac{2}{3}\frac{q_{NaCl}}{\omega}V_C \frac{\frac{4\pi}{3}R_{expl}^3 + \pi\left[\left(R_{expl}+L_{cr}\right)^2 - R_{expl}^2\right]T_{tip}}{\frac{4\pi}{3}R_{expl}^3 + \pi\left[\left(R_{expl}+L_{cr}\right)^2 - R_{expl}^2\right]T_{cr}} \tag{58}$$

The final crack length can be found by equating $P\left(V_C, R_{expl}, L_{cr}\right)$ to the threshold value, $P_f\left(R_{expl}, L_{cr}\right)$ given by

$$P_f\left(R_{expl}, L_{cr}\right) = \sqrt{\frac{EG_c}{2\pi\left(1-\nu^2\right)\left(R_{expl}+L_{cr}\right)}}. \tag{59}$$

T_{tip} is determined mainly by the crack tip geometry (in our calculations it is assumed to be equal to 6 nm), while the final crack thickness, T_{cr}, depends on the mechanism of its plastic expansion, such as the dislocation loop punching. The latter process has its own threshold pressure, P_{th} that can be estimated using results obtained for a spherical void [38]:

$$P_{th}\left(R_{expl}, L_{cr}\right) \approx \frac{\mu b}{\left(R_{expl} + L_{cr}\right)}, \tag{60}$$

Since P_{th} is inversely proportional to the void size, it is expected to be higher than the initial pressure in a relatively small void (at L_{cr} = 0), but it decreases rapidly with the crack propagation resulting in the crack expansion by loop punching up to the thickness determined by the final pressure, P_f, and the back stresses from the punched out loops [38]:

$$T_{cr}\left(R_{expl}, L_{cr}\right) \approx \frac{P_f\left[P_f\left(R_{expl} + L_{cr}\right) - \mu b\right]}{5\sigma_P \mu}, \tag{61}$$

where σ_P is the stress required for dislocation glide.

Thus a combined fracture-plastic process determines both the crack final length and thickness through the colloid number density and volume fraction. The result is shown in Fig. 52 in the form of crack length dependence on the colloid volume fraction at different colloid number densities, expected for different dopants, according to fig. 53.

It can be seen that the colloid number density, which determines the void explosion radius, has a drastic effect on the ultimate mechanical stability of material. If it is low as in NaCl:Br (below $10^{21}m^{-3}$) then the void-crack transition size is large and difficult to reach. If it is high as in NaCl:KBF_4 (above $10^{22}m^{-3}$) it takes a high colloid volume fraction to initiate the void-crack transition, which progresses gradually until the explosive fracture occurs. The materials doped with Ba or K, and natural rock salt show the transient behavior, which is the most susceptible to explosive fracture due to the unrestricted propagation of cracks. The latter starts at the point where the crack length derivative with respect to the colloid volume fraction becomes infinite. Above these points, there are no stable crack parameters, which implies that the positive feed back due to consumption of new "fuel" becomes stronger than the negative one due to the plastic relaxation of pressure. This process is analogous to the classic explosion process, which explains our term "explosive fracture".

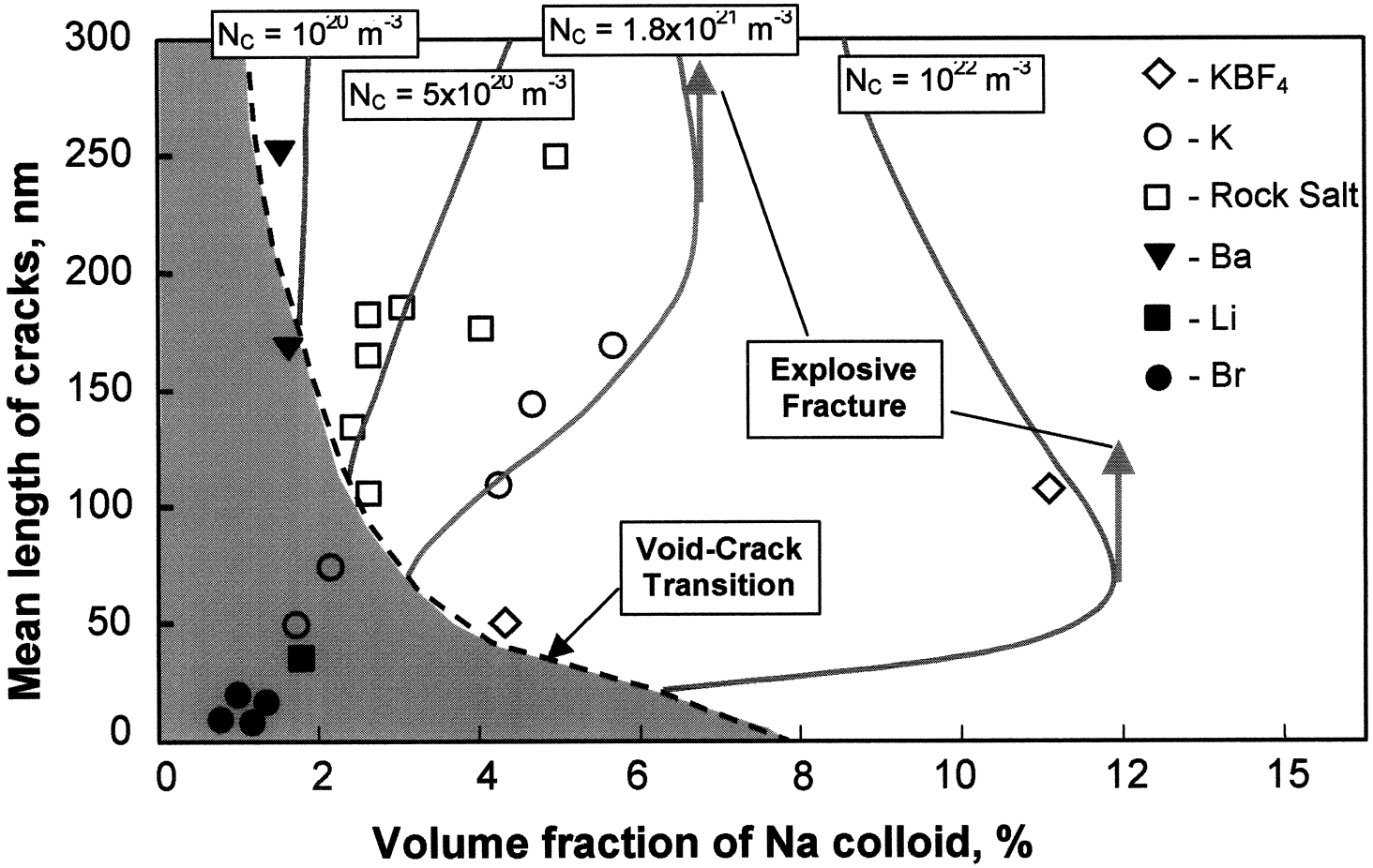

Figure 52. Diagram showing dependence of the maximum void size and a subsequent crack length on the colloid volume fraction, calculated for different colloid number densities, N_C indicated in the figure. The explosive fracture of the material starts at the point where the crack length derivative with respect to the colloid volume fraction becomes infinite. Above these points, no stable crack exists, which implies that the positive feed back due to consumption of new "fuel" becomes stronger than the negative one due to the plastic relaxation of pressure. Experimental points correspond to different dopants, for which experimental data on N_C are given in fig. 50.

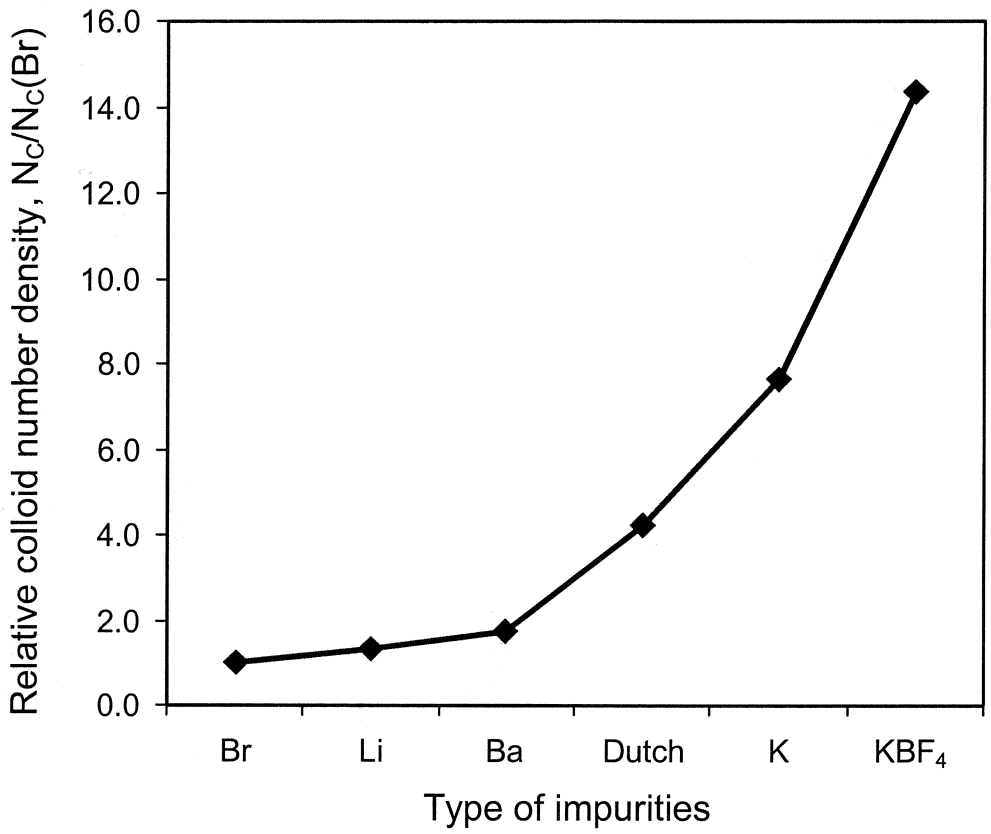

Figure 53. Colloid number densities in different materials after 300 Grad irradiation obtained by measuring the ESR signals from sodium colloids. A signal from Br doped samples was selected as a reference point.

3.4.2 *Critical parameters controlling mechanical stability of heavily irradiated NaCl*

In the present project, the formation of large vacancy voids under electron irradiation of NaCl crystals observed in our experiments has been explained within a framework of a theoretical model, which is based on a new mechanism of dislocation climb. The mechanism involves the production of V_F centers as a result of the absorption of excess H centers at dislocation lines. Voids are shown to arise due to formation of vacancy pairs (two adjacent vacancies, one in the cation and one in the anion sub-lattice) in the reaction between F centers and V_F centers at the surface of halogen bubbles. The model predicts that voids can grow to a size exceeding the mean distance between colloids and bubbles, eventually absorbing them, and, hence, bringing the halogen gas and metal to a back reaction. This leads to an explosive release of the radiation-induced stored energy. We attribute to that effect the destruction of salt samples after high dose irradiation. Thus, the evolution of voids strongly affects mechanical stability of salt materials. However, other types of extended defects formed by irradiation are also important and should be taken into consideration.

In this section, we summarize the critical microstructure, irradiation and material parameters that control mechanical stability of salt materials under irradiation.

Dislocations. The dislocation bias for absorption of H centers is the major driving force of the microstructural evolution under irradiation. The bias value will depend on the impurity content that may affect the dislocation interaction with H and F centers. Another important parameter is the dislocation density, which determines their sink strength. It is known to saturate with increasing irradiation dose at some value, which can be influenced by the impurity content and by the plastic deformation. Fig. 45 shows the void and colloid volume fractions calculated at different dislocation and bubble densities. It can be seen that too low as well as too high dislocation densities suppress both colloid and void formation, while the intermediate values favor the accumulation of radiation damage.

Chlorine bubbles. The volume fraction of chlorine "bubbles" (or rather solid or liquid chlorine precipitates, since the pressure in them is too high for the liquid-gas transition) is closely related to that of sodium colloids (fig. 54), which is a measure of the energy stored by irradiation. The higher it grows, the more potentially unstable becomes the material. But the actual mechanical stability is determined by a scenario of the stored energy release rather than by its value. If the back reaction quantum is small enough (as it is assumed in the Jain-Lidiard model, which considers only the recombination between chlorine molecules and F centers) then it may just limit the stored energy accumulation. But the voids can collect a large number of chlorine molecules before the collision with colloids starts, which changes the scale of the back reaction from the atomic to the macroscopic one, resulting in material fracture.

The bubble number density, which controls the critical irradiation dose of their transition to voids, is an important parameter. It is expected to depend on the content of impurity ions that can act as the bubble nuclei. So the bubble number density is another "free" parameter (along with dislocation density), which has a strong influence on microstructural evolution (Fig. 45). It can be seen that if the bubble number density is higher than some threshold value, the void formation can be suppressed, in which case the release of stored energy is possible only by direct collisions between growing sodium and chlorine precipitates. The latter process may be more gradual due to a finer scale of the mechanism involved, which may be less dangerous for the mechanical stability of material. So it may be an attractive type of further research to find the dopants acting as efficient traps for H centers, which could disperse chlorine among finer bubbles.

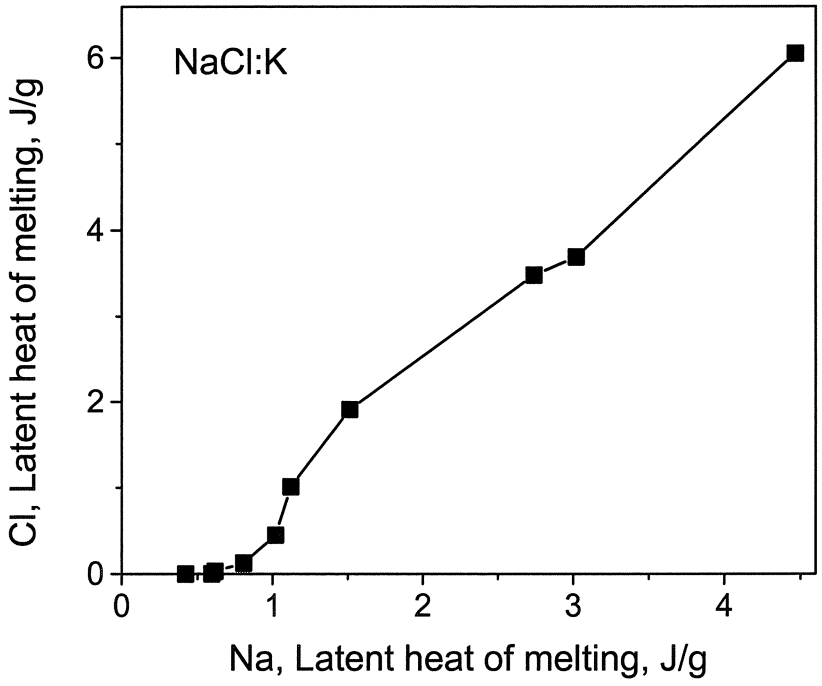

Figure 54. Latent heat of melting of chlorine (which is proportional to the chlorine bubble volume fraction) versus the latent heat of melting of sodium (which is proportional to the sodium colloid volume fraction). The linear dependence starts when a critical volume fraction of chlorine is reached resulting in its aggregation in bubbles.

Sodium colloids. As was mentioned above, the volume fraction of sodium colloids is a measure of the energy stored by irradiation. Another critical parameter is the colloid number density, which is illustrated in the void-crack transition diagram (fig. 52). If it is below $10^{21}m^{-3}$, then the void-crack transition size is large and difficult to reach. If it is above $10^{22}m^{-3}$, then a high colloid volume fraction is required to initiate the void-crack transition, which progresses gradually and may not result in explosive fracture. The materials doped with a majority of investigated dopants (such as Ba or K) and natural rock salt samples show the transient behavior, which is the most susceptible to explosive fracture.

Structural state of sodium colloids can also have a strong influence on the accumulation of radiation damage. Small colloids are expected to be coherent with the matrix, which means that they are under tensile stresses due to the misfit between Na and NaCl lattices. During later stages of irradiation, colloids lose coherency, which changes their stress state. Thus, coherent colloids have a misfit bias for the absorption of H centers, which slows their growth as compared to that of voids. On the other hand, after the loss of coherency, the colloid interfaces may start to capture V_F centers and produce electroneutral vacancy pairs, which may suppress the colloid growth but lead colloids to punch out vacancy dislocation loops. All these changes could be monitored, since they are reflected in the position of Na melting peak, which has been shown to move along the temperature axis non-monotonously during irradiation [39].

Voids have been shown to arise from halogen bubbles and grow to a size exceeding the mean distance between colloids and bubbles, eventually absorbing them, and, hence, bringing the halogen gas and metal to a back reaction. Thus, the void size is a parameter of primary importance that should be monitored during irradiation, as is evident from comparison of the mean void/crack sizes in stable NaCl:Br and unstable NaCl:K (fig. 55). According to a comparative analysis among different materials (Fig. 56, Tables 2 and 3), the most unstable materials produce the largest voids.

Another important factor is a shape of the voids, which shows at which stage of radiolysis the material is. If the voids are equiaxial then the explosive back reaction has not started yet or it is too weak to cause the void-crack transition. The appearance of elongated (or penny-shaped) voids indicates the beginning of the explosive fracture process. For a quantitative description it is convenient to define a *shape factor*, which is the ratio of the major and minor void axes. A sharp increase of the maximum shape factor after some irradiation dose (as shown in fig. 57) may be the last warning before the material failure.

Although voids can be the origin of the material fracture, their role in the structural evolution is quite ambiguous and complex. They can even cause an increased material stability against radiation damage if the number density of the voids is high and if the sizes are small. It turns out that voids may suppress the growth of colloids since they compete with them absorbing F centers. This competition is very strong if the rate of the bubble-to-void transition is sufficiently high to allow the formation of a high number density of relatively small voids (figs. 36b-39b). This situation has two advantages: first, the growth of voids is not very fast because of the competition between themselves, and second, the growth of colloids is suppressed since voids are the more powerful sinks for F centers. Consequently, the collisions between voids and colloids (i) will be postponed until higher doses and (ii) it may result in void shrinkage (due to the condensation of NaCl molecules, which are formed by the back reaction) rather than in the void-crack transition.

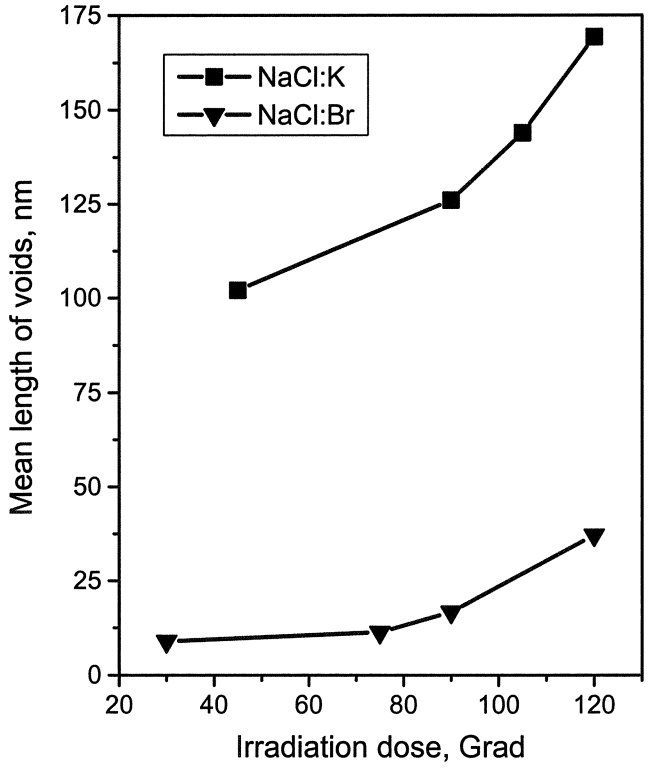

Figure 55. Comparison between void lengths in samples doped with K and Br.

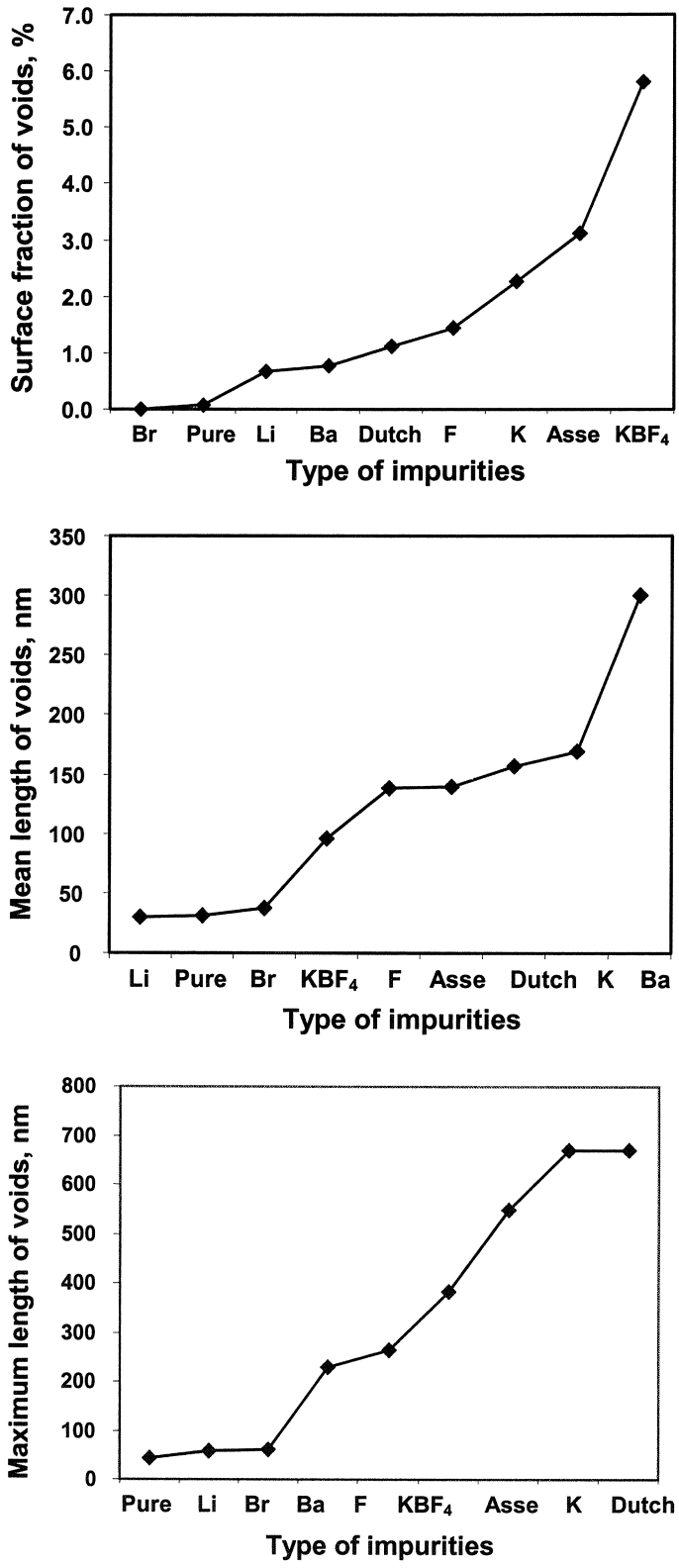

Figure 56. Void/crack parameters in different materials after irradiation to 300 Grad. The most unstable materials produce the largest voids.

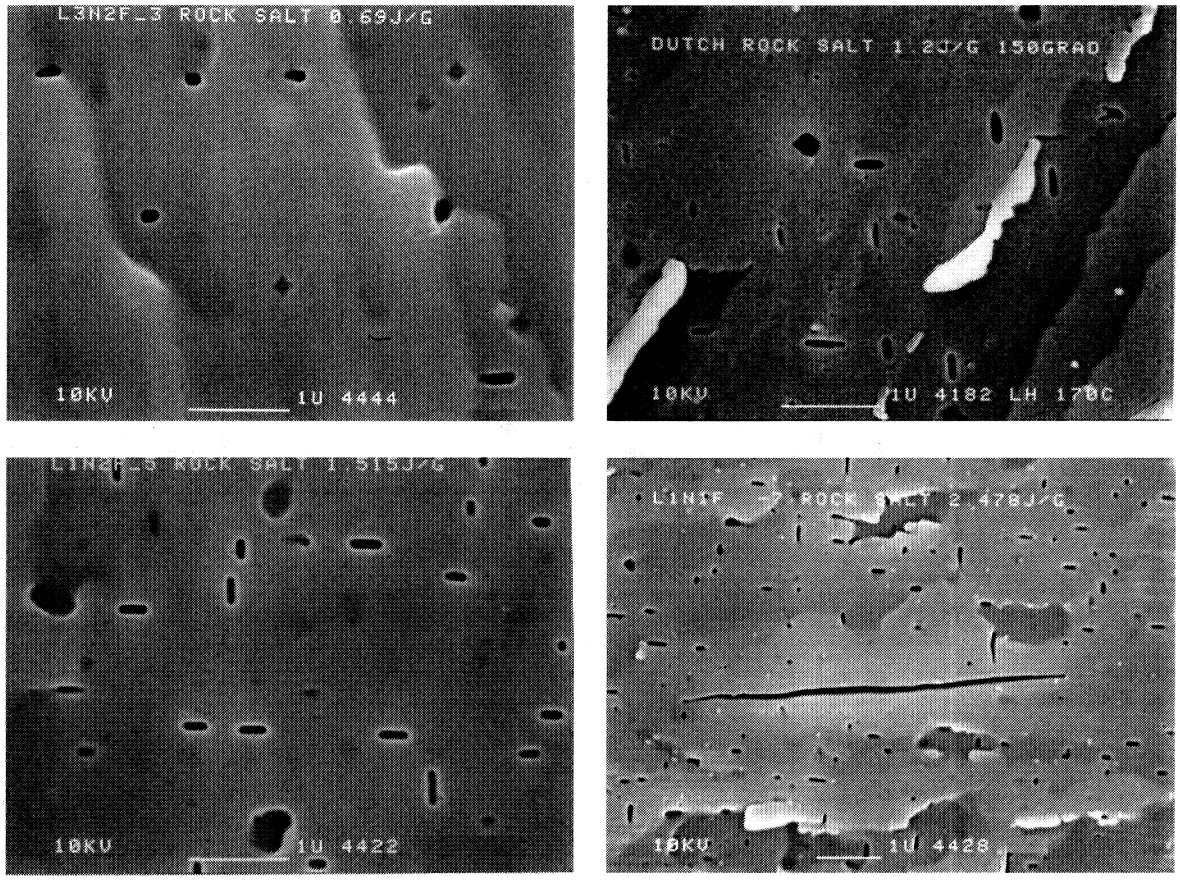

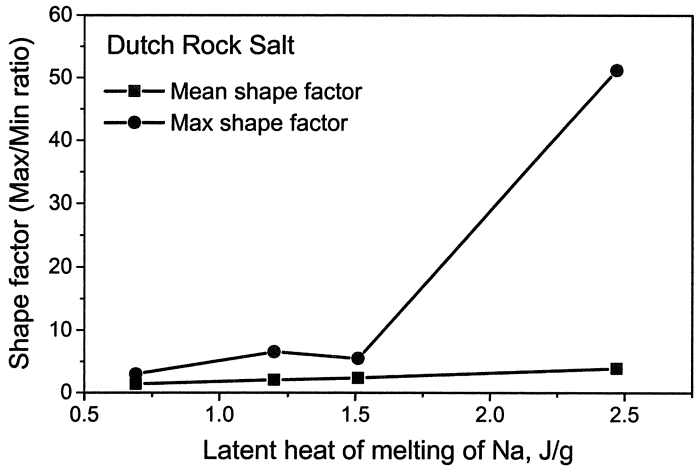

Dutch Rock Salt		
LHM, J/g	Mean shape factor	Max shape factor
0.69	1.41596	2.987
1.2	2.0573	6.530
1.51	2.3779	5.487
2.47	3.9182	51.190

Figure 57. SEM micrograph showing the correlation between void-crack formation and the volume fraction of sodium colloids, demonstrated also in the plot and the table.

Dose rate versus temperature effects. The intensity of our laboratory irradiation is several orders of magnitude higher than that expected under repository conditions, which poses a very important problem of the dose rate effects. From a theoretical point of view we know that irradiation conditions are controlled by two parameters, namely, dose rate, K, and temperature, T, which means that equivalent irradiation conditions can be achieved at different dose rates by adjusting irradiation temperature. This is illustrated in Fig. 40, which compares colloid production under the laboratory dose rate and under that assumed to model the radwaste repository irradiation. The parameters of primary importance are the F center formation and migration energies, which determine the upper temperature cut-off of colloid formation. We need reliable information on these parameters.

Irradiation dose versus material parameters effects. We have shown in the present project that the microstructural evolution in irradiated rock salt is characterized by several stages such as the formation of sodium precipitates and chlorine "bubbles" followed by the bubble-void transition and a subsequent void-crack transition leading to explosive fracture of the material. Each stage begins after some critical irradiation dose, which can be very different for different material and irradiation conditions. This is illustrated in Fig. 58, which shows the dependence of the dose required to initiate explosive back reaction in voids on the dislocation and bubble densities.

The critical doses predicted by the present theory are in a general agreement with our experimental data obtained in laboratory conditions. So they should be regarded as a demonstration of possible scenarios of the rock salt behavior under irradiation rather than as quantitative predictions of the backfill material behavior in the real conditions of repository. The latter requires further and more detailed investigations.

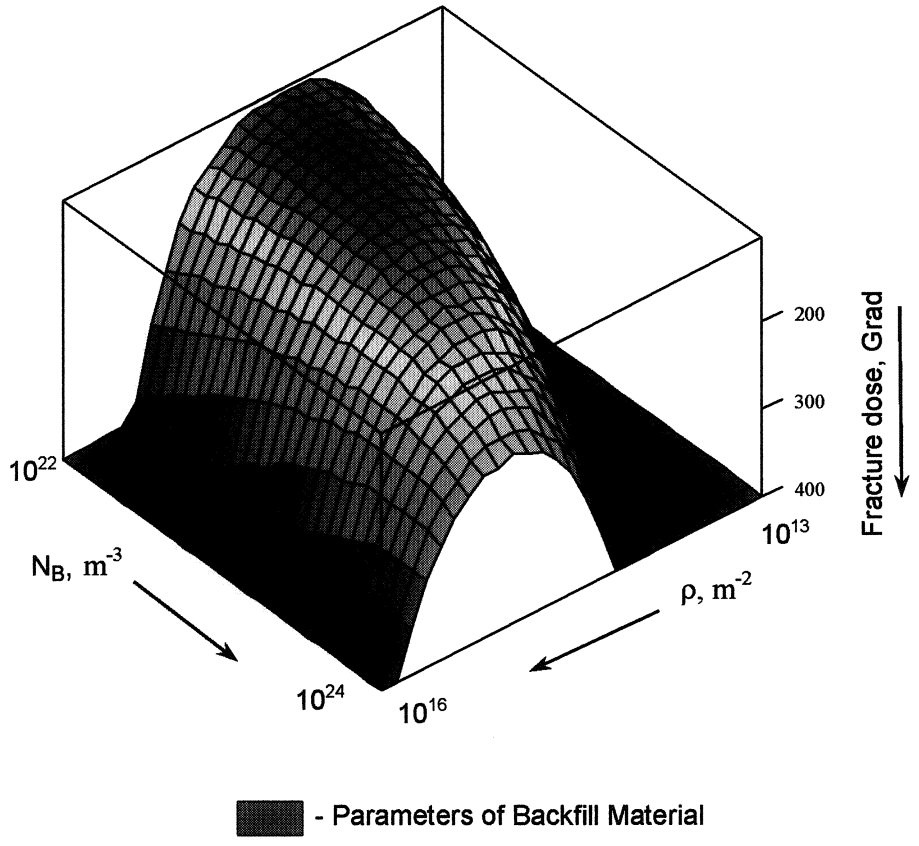

Figure 58. Irradiation dose required to initiate explosive back reaction of radiolytic products inside the voids, calculated by the equation $R_{Vexp} = R_{Void}$.

4 CONCLUSIONS AND OUTLOOK

Goal 1: Investigation of voids

- Systematic experiments on many (pure, doped and natural rock salt) irradiated samples have shown that with increasing irradiation dose formation of large voids is observed, which strongly depends on the impurity content.
- The void formation cannot be explained within the framework of models of the Jain-Lidiard type.
- We have presented a new concept of the microstructure evolution, which is verified by the phenomena observed in rock salt.
- Voids can grow to a size exceeding the mean distance between colloids and bubbles, eventually absorbing them, and, hence, bringing the halogen gas and metal to a back reaction. This leads to an explosive release of the radiation-induced stored energy. We attribute to that effect the fracture of salt samples after high dose irradiation.

Goal 2: Backfill materials

- Structural stability of rock salt under irradiation strongly depends on the dopants.
- The radiation stability of NaCl:Br is the highest among all the materials investigated in this project. Bromine doped materials show reduction of both colloid and void production even as compared to pure NaCl, and they appear to be the most promising as backfill materials.

Goal 3: Monitoring

- Evolution of voids controls the mechanical stability of salt materials, since voids reaching certain size trigger the explosive instability resulting in the fracture of the material.
- The void size and shape are the parameters of primary importance that should be monitored during irradiation since the most unstable materials produce the largest voids, which result in the void-crack transition.

Outlook

- More experimental studies of the *NaCl* radiolysis are required in order to check and tune the theoretical model and then to apply them to the rock salt monitoring in the real conditions of depository.
- The new concept can be a prototype of an adequate description of the long-term behavior of the important insulating materials in intense radiation fields, which can be employed for an evaluation of the critical effects expected under storage conditions and creation of radiation resistant materials.

5 PRESENTATIONS AND PUBLICATIONS

The results of this project have been presented at the 8th Europhysical Conference on Defects in Insulating Materials (EURODIM'98), Keel, UK, 1998; 4th International Conference on Computer Simulation of Radiation Effects in Solids (COSIRES'98), Okayama, Japan, 1998; 10th International Conference on Radiation Effects in Insulators (REI-10), Jena, Germany, 1999; 16th International Workshop on Charged Particle Linear Accelerators, Alushta, Ukraine, 1999; the European Commission Conference on Radioactive Waste Management Strategies and Issues (EURADWASTE'99), Luxembourg, Nov. 1999.

Publications of the present results include the following (see also the supplement):

1. V. I. Dubinko, A. A. Turkin, D. I. Vainshtein, H. W. den Hartog, New formulation of the modeling of radiation-induced microstructure evolution in alkali halides, Radiation Effects and Defects in Solids, vol. 150 (1999) 145-149.
2. H.W. den Hartog, Stored energy in heavily irradiated NaCl, Radiation Effects and Defects in Solids, vol. 150 (1999) 167-172.
3. D. I. Vainshtein, V. I. Dubinko, A. A. Turkin, and H. W. den Hartog, Void formation in heavily irradiated NaCl, Radiation Effects and Defects in Solids, vol. 150 (1999) 173-177.
4. V. I. Dubinko, A. A. Turkin, D. I. Vainshtein, H. W. den Hartog, Modeling of the radiation-induced microstructural evolution in ionic crystals, Nucl. Instr. and Meth. in Phys. Research, B153 (1999) 163-166.
5. V. I. Dubinko, A. A. Turkin, D. I. Vainshtein, H. W. den Hartog, A New Mechanism for Radiation Damage Processes in Alkali Halides, J. Appl.Phys, 86 (1999) 5957 –5960.
6. V. I. Dubinko, A. A. Turkin, D. I. Vainshtein, H. W. den Hartog, Theory of the late stage of radiolysis of alkali halides, J. Nucl Mater. 277 (2000) 184-198.
7. D.I. Vainshtein, H.W. den Hartog, Explosive decomposition of heavily irradiated NaCl, Radiation Effects and Defects in Solids, 1999, accepted for publication, in press.
8. V. I. Dubinko, A. A. Turkin, D. I. Vainshtein, H. W. den Hartog, Effect of Dose Rate, Temperature and Impurity Content on the Radiation Damage in the Electron Irradiated NaCl Crystals, presented at the 10th International Conference on Radiation Effects in Insulators, Jena, Germany, 1999; accepted for publication in Nucl. Instr. and Meth. in Phys. Research.
9. D. I. Vainshtein, V. I. Dubinko, A. A. Turkin and H. W. den Hartog, Effect of the void formation on the explosive decomposition of electron irradiated NaCl crystals, presented at the 10th International Conference on Radiation Effects in Insulators, Jena, Germany, 1999; accepted for publication in Nucl. Instr. and Meth. in Phys. Research.

6 REFERENCES

1. Uma Jain and A. B. Lidiard, Phil. Mag. 35, 245 (1977).
2. H. Gies, W. Hild, T. Kuhle and J. Monig, Radiation effects in rock salts, GSF-Report 9/93, GSF Munchen, 1994.
3. W. J. Soppe, H. Donker, A. Garcia Celma, J. Prij, J. Nucl. Mater. 217 (1994) 1-31
4. A. B. Lidiard, Comments Solid State Phys. 8, 73 (1978).
5. L. W. Hobbs A. E. Huges and Pooley, Proc Roy. Soc. (Lond.), A332, 167 (1973).
6. D. I. Vainshtein, C. Altena and H.W. Den Hartog, Mater. Sci. Forum. 239-241 (1997) 607
7. H.W. Den Hartog and D. I. Vainshtein, Mater. Sci. Forum. 239-241, 611 (1997).
8. D. I. Vainshtein, V. I. Dubinko, A. A. Turkin, and H. W. den Hartog, Radiation Effects and Defects in Solids, vol. 150 (1999) 173-177.
9. W. J. Weber, L. K. Mansur, F. W. Clinard, Jr., D. M. Parkin, J. Nucl. Mater. 184 (1991) 1-21.
10. V. I. Dubinko, J. Nucl. Mater. 206,1 (1993).
11. V. I. Dubinko, A. A. Turkin, D. I. Vainshtein, H. W. den Hartog, J. Nucl Mater. 277 (2000) 184-198.
12. V. I. Dubinko, Nucl. Instr. and Meth. in Phys. Res. B102 (1995) 125-131.
13. E. Johnson, L. T. Chadderton, Radiat. Eff. 79 (1983) 183-233.
14. L. W. Hobbs, F. W. Clinard, Jr., S. J. Zinkle, R. C. Ewing, Radiation effects in ceramics, J. Nucl. Mater. 216 (1994) 291-321.
15. H. A. Bethe, Handbuch fur Physik, Springer Verlag, Berlin, (1933), vol. 24/2.
16. M. J. Berger and S. M. Seltzer, Stopping power for electrons and positrons (ICRU-37), Washington D.C., (1984).
17. L. V. Spenser, Natl. Bur. Std. (U.S.) Monograph 1 (1959).
18. B.N. Shubba Rao, Nucl. Instr. Methods 44, (1966), p. 155.
19. E. J. Kobetich and R. Katz, Phys. Rev. 170, (1968), p. 391.
20. M. J. Berger, in Methods in Computational Physics, edited by B. Adler, S. Fernbach and M. Rotenberg.
21. V. I. Dubinko, J. Nucl. Mater. 225 (1995) 26.
22. V. I. Dubinko, P. N. Ostapchuk and V. V. Slezov, J. Nucl. Mater. 161 (1989) 239.
23. W. G. Wolfer and M. Ashkin, J. Appl. Phys. 46 (1975) 547.
24. P. N. Ostapchuk and N. I. Ischenko, On the void bias factor in elastically anisotropic cubic crystals, Preprint KIPT 93-19, Kharkov 1993, 14 p.
25. E. J. Savino, Philos. Mag. 36 (1977)323.
26. P. H. Dederich, K. Schroeder , Phys. Rev. B 17 (1978) 2524.

27. V. A. Borodin, A.I. Ryazanov, C. Abromeit, J. Nucl. Mater. 207 (1993) 242.
28. G. W. Greenwood, A. J. E. Foreman and D. E. Rimmer, J. Nucl. Mater. 4 (1959) 305.
29. J.H. Evans, A.Van Veen and L.M. Caspers: Radiat. Eff. 78 (1983) 611.
30. V. I. Dubinko, V.V. Slezov, A.V. Tur and V.V. Yanovskij, Radiat. Eff. 100 (1986) 85.
31. L. K. Mansur, E. H. Lee, P. J. Maziasz and A. P. Rowcliffe, J. Nucl. Mater. 141-143 (1986) 633.
32. V. I. Dubinko, V. V. Slezov, A.V. Tur and V.V. Yanovskij, Radiation-induced generation of dislocation loops by precipitates, Doklady Akademii Nauk SSSR (in Russian), 291(1986) 87.
33. V. I. Dubinko, J. Nucl. Mater. 233-237 (1996) 832.
34. E. R. Hodgson, A. Delgado and F. Agullo-Lopez, F.J. Lopez, Radiat. Eff. 74 (1983) 193.
35. Lushchik, Ch. Lushchik, N. Lushchik, A. Frorip and O. Nikiforova, Phys. Stat. Sol. (b) 168 (1991) 413.
36. A. V. Gektin, V. Ya. Serebryany and N. V. Shiran, Radiat. Eff. and Def. in Sol. 134 (1995) 411.
37. R. E. Voskoboinikov, J. Nucl. Mater. 270 (1999) 309.
38. V. I. Dubinko, A. N. Efremenko, A.V. Tur and V.V. Yanovskij, Dislocation mechanism of void interaction, Fiz. Met. i. Metalloved. (in Russian) №4 (1990) 39-47.
39. J. Seinen, D.I. Vainshtein, H.C. Datema, H.W. den Hartog, J. Phys. C: Condens. Matter. 7 (1995) 705-716.

7 TABLES

Table 1. Material parameters of NaCl and Na colloids used in calculations

Parameter	*Value*
Irradiation parameters	
Irradiation temperature, T, ^{0}C	60 – 130
Dose rate, K, Mrad/hour (dpa/s)	240 (6.7×10^{-6})
Maximum dose, Grad (displacements per atom, dpa)	300 (30)
Material constants	
Diffusion coefficient of H-centers, m^2s^{-1}	$10^{-6}\exp(-0.1eV/kT)$
Diffusion coefficient of F-centers, m^2s^{-1}	$10^{-6}\exp(-0.7eV/kT)$
Diffusion coefficient of V_F centers, m^2s^{-1}	$10^{-6}\exp(-0.69eV/kT)$
Formation energy of F centers, E_F^f, eV	1.0
F-H recombination rate constant, m^{-2}	1.13×10^{20}
NaCl shear modulus, μ, GPa	12.61
Pierls stress, σ_P	$10^{-4}\,\mu$
NaCl Young's modulus	40
NaCl bulk modulus	6.3
Poisson ratio, ν	0.333
Na shear modulus, μ_C, GPa	3.3
Interface energy of coherent colloid, γ_c, J/m^2	0.01
Surface energy of *NaCl*, γ, J/m^2	0.228
Total work of fracture, G_c	$4\,\gamma$
Atomic volume of the host lattice, ω, m^{-3}	4.4×10^{-29}
Chlorine molecule volume, ω_{Gas}	1.7 ω
Relaxation volume of H centers, Ω_H	1.2 ω
Relaxation volumes F centers, Ω_F	-0.4 ω
Colloid misfit, ε	0.068
Heat of formation of *NaCl* molecule, q_{NaCl}, eV	4.25
Bias constants	
Dislocation bias, δ_d (see eq. 1)	0.47
Misfit bias of coherent colloids, δ_ε (see eq. 11)	0.37
Elastic-diffusion anisotropy interaction constant, α^d (see eq. 8)	5
"Image" interaction constant for colloids, α_c^{im} (see eq. 12)	0.941
"Image" interaction constant for voids, α^{im} (see eq. 8)	1.041
Modulus minus elastic anisotropy interaction constant, $\alpha^{\mu,\zeta}$ (see eq. 9)	0

Table 2. Mean length of voids/cracks vs. colloid volume fraction observed in different materials after irradiation up to 300 Grad

Ba		Br		F		KBF		Li		Rock Salt	
Na volume fraction, %	Length, nm	Na volume fraction, %	Length, nm	Na volume fraction, %	Length, nm	Na volume fraction, %	Length, nm	Na volume fraction, %	Length, nm	Na volume fraction, %	Length, nm
1.2	251.8	0.72	8.9	1.08	60	4.2	50.0	1.74	35.5065	1.68	50.0
1.6	166.9	0.87	20.0	1.66	90	10.6	150.0			2.1	75.0
		1.10	11.3	4.4	110	11.2	112.6			4.2	110.0
		1.30	16.7							4.6	143.9
										5.6	169.3

Table 3. Parameters of voids/cracks vs. colloid volume fraction observed in different materials after irradiation up to 300 Grad

Irradiated NaCl	Colloids		Voids/Cracks			
	LHM, J/g	Volume fraction of Na, %	Mean Length, nm	Max Length, nm	Surface Fraction,%	Volume Density, cm^{-3}
Br	0.50	1	37.2	57.1	0.002	1.00E+10
Pure	0.60	1.2	31.2	44.1	0.1	4.20E+13
Li	0.87	1.74	29.6	59.52	0.7	3.81E+14
Ba	0.60	1.2	300.0	382.0	0.8	7.67E+12
Dutch	2.47	4.94	156.8	654.2	1.1	1.21E+13
F	2.20	4.4	138.1	264.5	1.4	1.05E+13
K	2.47	4.94	169.3	668.80	2.3	1.98E+13
Asse	2.60	5.2	139.3	547.18	3.1	2.60E+13
KBF4	5.30	10.6	95.6	227.6	5.8	1.27E+14

8 ABBREVIATIONS

AC	Alternating Current
DC	Direct Current
DSC	Differential Scanning Calorimetry
EPR	Electron Paramagnetic Resonance
ESR	Electron Spin Resonance
HLW	High Level Waste
kV	Kilo Volt (1000 Volts)
LINAC	Linear Electron Accelerator
μA	Micro-Ampere
mA	Milli-Ampere
PID	Proportional Integration Differentiation
PLC	Programming Logical Controller
SEM	Scanning Electron Microscopy